TU Delft

Delft University of Technology

Development of inorganic nanoparticles for radionuclide therapy in cancer treatment

Wang, R.

DOI
10.4233/uuid:42efb000-bcae-4560-8a31-c984d2400ca0

Publication date
2024

Document Version
Final published version

Citation (APA)
Wang, R. (2024). *Development of inorganic nanoparticles for radionuclide therapy in cancer treatment*. [Dissertation (TU Delft), Delft University of Technology]. https://doi.org/10.4233/uuid:42efb000-bcae-4560-8a31-c984d2400ca0

Important note
To cite this publication, please use the final published version (if applicable).
Please check the document version above.

Copyright
Other than for strictly personal use, it is not permitted to download, forward or distribute the text or part of it, without the consent of the author(s) and/or copyright holder(s), unless the work is under an open content license such as Creative Commons.

Takedown policy
Please contact us and provide details if you believe this document breaches copyrights.
We will remove access to the work immediately and investigate your claim.

This work is downloaded from Delft University of Technology.
For technical reasons the number of authors shown on this cover page is limited to a maximum of 10.

Development of inorganic nanoparticles for radionuclide therapy in cancer treatment

Runze WANG

Development of inorganic nanoparticles for radionuclide therapy in cancer treatment

Dissertation

For the purpose of obtaining the degree of doctor
at Delft University of Technology,
By the authority of the Rector Magnificus Prof.dr.ir. T.H.J.J. van der Hagen,
chair of the Board for Doctorates,
to be defended publicly on Wednesday 15th of May 2024 at 12:30 hours

by

Runze WANG

Master of Science in Chemical Engineering, Delft University of Technology, the Netherlands
Born in Harbin city, China

This dissertation has been approved by the promotors.

Composition of the doctoral committee:

Rector Magnificus	Chairman
Dr. ir. A.G. Denkova	Delft University of Technology, promotor
Prof. dr. H.T. Wolterbeek	Delft University of Technology, promotor

Independent members:

Dr. B.T. Cornelissen	University of Groningen
Dr. J.F.W. Nijsen	Radboudumc
Dr. R. Eelkema	Delft University of Technology
Dr. K. Djanashvili	Delft University of Technology
Prof. dr. S.J. Picken	Delft University of Technology
Prof. dr. ir. J.L. Kloosterman	Delft University of Technology, reserve member

The research presented in this thesis was performed at the Applied Radiation and Isotopes section of the department of Radiation Science and Technology, Faculty of Applied Sciences, Delft University of Technology, the Netherlands. This research was funded by the China Scholarship Council (CSC).

Cover designed based on a picture generated by Suno AI

Auditory abstract generated by ChatGPT 3.5 and Suno AI

Printed by Proefschriftspecialist

ISBN: 978-94-6384-538-0

Copyright © 2024 by Runze Wang

All rights reserved. No part of the material protected by this copyright notice may be reproduced or utilized in any form or by any other means, electronic or mechanical, including photocopying, recording or by any information storage and retrieval system, without written permission from the author.

Printed in the Netherlands

Sic Parvis Magna

Greatness from Small Beginnings

-Sir Francis Drake

CONTENTS

Chapter 1 General introduction **1**

Chapter 2 Core-shell structured gold nanoparticles as carrier for ^{166}Dy/^{166}Ho *in vivo* generator **29**

Chapter 3 Ultra-small gold nanoparticles radiolabeled with Iodine-125 as potential new radiopharmaceutical **53**

Chapter 4 Indium-111 radiolabeled ultra-small gold and silver telluride nanoparticles for radionuclide therapy **79**

Chapter 5 Inorganic nanoparticles as carriers for the lead-212/bismuth-212 *in vivo* generator: a solution to the loss of bismuth-212 caused by internal conversion **107**

Chapter 6 General conclusions and future perspectives **125**

Summary **129**

Samenvatting **133**

List of publications **137**

Acknowledgements **139**

Curriculum Vitae **143**

General introduction

1

1. Radionuclide therapy

The application of radiation in the treatment of various diseases, especially cancer, could be dated back to 1900s when the phenomenon of natural radiation was discovered by Henri Becquerel, Marie and Pierre Curie. Nowadays, radiotherapy still plays an important role in cancer treatment. Annually, more than 50% of all cancer patients are treated by external beam radiation therapy (EBRT) using X-rays or charged particles.[1] Besides EBRT, radionuclide therapy (RNT) has also shown unique advantages in treating metastasized cancer. The radiopharmaceuticals used in RNT normally consist of three components: a radionuclide, a carrier and a tumor targeting moiety, all of which will be discussed in more detail in Chapter 1.

1.1. Radionuclides for RNT

Although there are hundreds of radionuclides in total, only a few have suitable physical properties such as appropriate half-life time so that they can be used in medical applications (Figure 1.1.1).[2] Radionuclides emitting low energy gamma photons and positrons are typically applied for imaging using single photon emission computed tomography (SPECT) and positron emission tomography (PET) respectively.[3] In the case of cancer treatment, α, β^-, and Auger electron (AE) emitters are preferred. The main properties of these particles are summarized in Table 1.1.1. β^- particles have the longest range (up to several millimeters in tissue) which allows them to irradiate the whole tumor volume by the so called "crossfire effect".[4] In the case of α particles and AEs, their ranges are relatively shorter, covering a few cell diameters (in μm) and a few nanometers respectively. Thus, α and AE emitters are preferred for the eradication of small tumors such as metastases.[5] Considering the short range of α particles and AEs, it is critical to deliver the radionuclides to the tumor site for proper tumor control. Specifically, AE emitters need to be delivered to the cell nucleus in order to induce sufficient damage to the DNA molecules.[6] However, there have been a few studies showing that the cell membranes could also function as a target for AE emitters and achieve tumor destruction.[7-9]

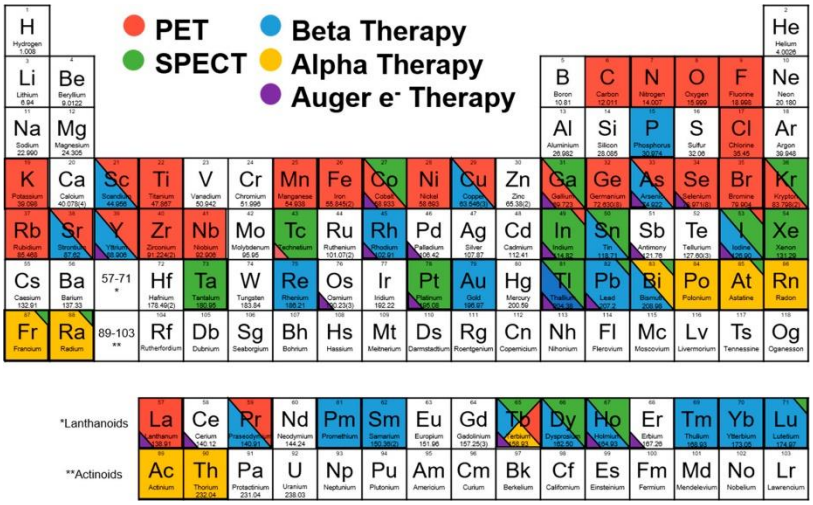

Figure 1.1.1. Color-coded periodic table with current or potential applications of each element in diagnostic and/or therapeutic applications (Adapted from Ref. [2] with permission. Copyright 2019, American Chemical Society).

The concept of linear energy transfer (LET) has long been employed in the field of radiation oncology to describe the "quality" of radiation. LET refers to the energy deposited by ionizing particles along their path through matter and is indicative of the density of ionization events. High-LET particles, such as α particles and AEs, deposit their energy in a more intense manner, resulting in dense ionizations along their path. This can lead to direct and lethal damage to the tumor cells, including DNA double-strand breaks (DSBs). In contrast, low-LET particles, such as β^- particles, tend to deposit their energy sparsely and can often produces sub-lethal damage that can be repaired.[10] However, when the number of sub-lethal damage events exceeds the threshold value, it can still lead to lethal damage and eventually cell death.[11]

Table 1.1.1. Main physical properties of α particles, β^- particles and AEs

	Energy	LET	Range in tissue
α particles	2-10 MeV	50-230 keV/μm	50-100 μm
β^- particles	0.05-2.3 MeV	0.2 keV/μm	1-5 mm
Auger electrons	10 eV-10 keV	4-26 keV/μm	Nanometers

A selection of radionuclides that have been applied in cancer treatment are summarized in Table 1.1.2. The half-life, maximum energy of emitted particles, number of AEs and common production method of these radionuclides are listed.

Table 1.1.2. Representatives of radionuclides for cancer treatment [a]

Nuclide	Decay mode	Half-life ($t_{1/2}$)	Maximum energy of the emitted particles	Production Route
β⁻ particle emitters				
^{90}Y	β⁻	64.1 h	2.278 MeV	^{89}Y(n,γ)^{90}Y ^{90}Sr/^{90}Y generator
^{131}I	β⁻	193.0 h	606 keV	^{130}Te(n,γ)^{131}Te→^{131}I
^{161}Tb	β⁻	165.4 h	522 keV	^{160}Gd(n,γ)^{161}Gd→^{161}Tb
^{166}Ho	β⁻	26.8 h	1.854 MeV	^{165}Ho(n,γ)^{166}Ho ^{166}Dy/^{166}Ho generator
^{177}Lu	β⁻	161.0 h	496.8 keV	^{176}Lu(n,γ)^{177}Lu ^{176}Yb(n,γ)^{177}Yb → ^{177}Lu
^{186}Re	β⁻ (92.5%) EC (7.5%)	90.6 h	1.073 MeV	^{185}Re(n,γ)^{186}Re
^{188}Re	β⁻	17.0 h	2.120 MeV	^{188}W/^{188}Re generator
α particle emitters				
^{211}At	EC (58.2%) α (41.8%)	7.2 h	5.869 MeV	^{209}Bi(α,2n)^{211}At
^{212}Pb/^{212}Bi	β⁻/ β⁻ (64.1%) α (35.9%)	10.6 h/1.0 h	6.051 MeV	^{224}Ra/^{212}Pb generator
^{213}Bi	β⁻ (97.9%) α (2.1%)	45.6 min	5.875 MeV	^{225}Ac/^{213}Bi generator
^{223}Ra	α	274.3 h	5.979 MeV	^{227}Th/^{223}Ra generator
^{225}Ac	α	240.0 h	5.830 MeV	^{229}Th/^{225}Ac generator ^{226}Ra(p,2n)^{225}Ac ^{232}Th(p,2p6n)^{225}Ac
Auger electron emitters [b]				
^{67}Ga	EC	78.3 h	5.0 AEs	^{67}Zn(p,n)^{67}Ga
^{111}In	EC	67.3 h	7.4 AEs	^{111}Cd(p,n)^{111m,g}In ^{112}Cd(p,2n)^{111m,g}In
^{123}I	EC	13.3 h	13.7 AEs	^{124}Xe(p,pn)^{123}Xe → ^{123}I
^{125}I	EC	60.1 d	23.0 AEs	^{124}Xe(n,γ)^{125m,g}Xe→ ^{125}I
^{161}Tb	β⁻	165.4 h	0.9 AEs	^{160}Gd(n,γ)^{161}Gd→^{161}Tb
^{195m}Pt	IT	96.5 h	36.6 AEs	^{194}Pt(n,γ)^{195m}Pt
^{203}Pb	EC	51.9 h	23.3 AEs	^{203}Tl(p,n)^{203}Pb

[a]The decay data was obtained from the Evaluated Nuclear Structure Data File (ENSDF) datasets, National Nuclear Data Center, Brookhaven National Laboratory, NY, USA.
[b]The number of Auger electrons per decay was obtained from ref [12]. The data of ^{161}Tb was taken from ref [13].

Iodine-131 (^{131}I) is one of the first radionuclides investigated for cancer treatment. As iodine could naturally accumulate in the thyroid, ^{131}I has been widely applied for treating thyroid cancer including papillary and follicular thyroid carcinoma.[14-16] Yttrium-90 (^{90}Y) and holmium-166 (^{166}Ho) both emit highly energetic β^- particles which makes them very suitable for treating large metastases. Actually, ^{90}Y loaded glass or resin microspheres[17-19] and ^{166}Ho loaded polymeric microspheres[20-21] have been approved for the treatment of hepatocellular carcinoma and liver metastases. The mother nuclide of ^{166}Ho, dysprosium-166 (^{166}Dy) has a half-life time of 81.6 h, approximately three times longer than that of ^{166}Ho.[22] By using ^{166}Dy as the internal source of ^{166}Ho, i.e. ^{166}Dy/^{166}Ho *in vivo* generator, same treatment outcome could be expected with less administrated activity. ^{177}Lu emits not only β^- particles but also γ particles which could be tracked by SPECT. Extensive research has been performed to link ^{177}Lu to various tumor targeting agents via chelation. ^{177}Lu-DOTATATE and ^{177}Lu-PSMA-617 have successfully passed the clinical trials and are now approved by the U.S. Food and Drug Administration (FDA) and the European Medicines Agency (EMA) for treating neuroendocrine tumors and prostate cancer respectively.[23-25] Terbium-161 (^{161}Tb) has been recently proposed for cancer treatment because of its similar chemical and physical properties as ^{177}Lu and has shown better therapeutic effect than ^{177}Lu in a few preclinical studies.[26] However, the supply of ^{161}Tb is still limited, restraining the development of ^{161}Tb based radiopharmaceuticals.

Some α emitters like radium-223 (^{223}Ra) and actinium-225 (^{225}Ac) can generate multiple α particles via their decay chains, leading to irreparable DNA damage in tumor cells.[27-29] In fact, radium-223 chloride (Xofigo®) was the first alpha radiopharmaceutical that has been approved by the FDA for the treatment of bone metastases.[30] Despite the positive results from pre-clinical and clinical studies of ^{223}Ra and ^{225}Ac, the distribution of their daughter nuclides in healthy tissues as a result of the recoil effect has raised a concern of possible radiotoxicity to patients.[31] There have been several attempts to reduce the side effects from the dissociated daughter nuclides of ^{225}Ac using nanoparticles.[32-33] However, these approaches all require carriers with large sizes which will mainly accumulate in the liver or spleen after being intravenously administrated. Apart from using chemical approaches to deal with the recoil problem, it is also possible to use α emitters with short decay chains such as ^{211}At and ^{212}Pb/^{212}Bi which do not suffer from the recoil problem.[34]

β^+ and electron capture (EC) decay are usually accompanied by the emission of Auger electrons. When these AEs are emitted close enough to the DNA molecules, they can deposit high dose on the DNA strands, leading to DSBs.[35] In addition to the direct interaction between AEs and DNA molecules, the formation of free radicals from the radiolysis of water by the AEs also plays an important role in cell death by causing indirect damage to the DNAs.[13] Due to the short range of the AEs, several strategies have been proposed to deliver the AE emitters to the cell nucleus and achieve maximum cytotoxicity. AE emitters such as ^{111}In and ^{161}Tb have been linked to antibodies targeting the epidermal growth factor receptor (EGFR) or prostate-specific membrane antigen (PSMA) and resulted in good tumor control in both *in vitro* and *in vivo* studies.[7, 36-37] Nucleosides are also potential carriers for AE emitters because of their direct incorporation in the DNA molecules. For example, 5-iodo-2-deoxyuridine (IUdR) radiolabeled with ^{125}I and ^{123}I were reported to cause profound cytotoxicity to tumor cells even at low activity.[38-39] However, the results from clinical trials of AE emitters-based radiopharmaceuticals were not satisfying, hindering their translation to the clinic.[40]

1.2. Conventional radionuclide carriers

A good match between carriers and radionuclides is essential for the design of radiopharmaceuticals. As most of the therapeutic radionuclides are metals, their radiolabeling can be generally achieved by forming complexes with chelators.[41] Macrocyclic chelators such as 2,2′,2″,2‴-(1,4,7,10-Tetraazacyclododecane-1,4,7,10-tetrayl) tetraacetic acid (DOTA), 1,4,7-triazacyclononane-1,4,7-triacetic acid (NOTA), 4-[2-(bis-carboxymethylamino)-ethyl]-7-carboxymethyl-[1,4,7]triazonan-1-yl-acetic acid (NETA) and their derivatives have been extensively used for the radiolabeling of ^{64}Cu, ^{166}Ho, ^{90}Y, ^{177}Lu, ^{212}Pb and ^{225}Ac.[42] Besides these macrocyclic molecules, acyclic chelators such as diethylenetriaminepentaacetic acid (DTPA) and desferrioxamine (DFO) are also commonly used in the radiolabeling of ^{111}In and ^{89}Zr respectively.[43-45]

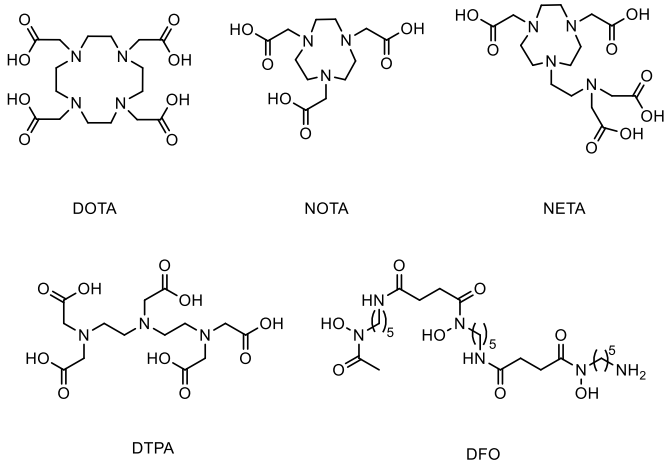

Figure 1.1.2. Structure of chelators commonly used in RNT.

1.3. Active tumor targeting

One of the most important properties of a radiopharmaceutical is the specificity to tumor sites. This can be achieved by linking tumor targeting moieties to the radionuclides using chelators as linking molecules. Common targeting moieties include antibodies, peptides, transferrin and some small molecules such as folic acid.[46-48] The antibodies and peptides usually target specific receptors which are overexpressed on a specific type of tumor cells such as EGFR for breast cancer[49] and PSMA for mainly prostate cancer[50-52]. Fibroblast activation protein (FAP) is overexpressed in the fibroblasts surrounding the tumor cells, thus has also been considered as a potential target for radiopharmaceuticals.[53-54] Currently, targeting molecules such as the PSMA inhibitor[55-56] and FAP inhibitor[57-58] are extensively studied for radio-ligand targeted therapy in both preclinical and clinical studies.

2. Combining nanomedicine with radionuclide therapy: a promising approach for cancer treatment?

Nanomedicine is an interdisciplinary subject that makes the use of nanotechnology to diagnose, treat, and prevent diseases. Taking the advantages of small size, large surface area, and ability to penetrate biological barriers, nanoparticles have been widely utilized for drug delivery.[59] Recently, the application of nanoparticles in cancer treatment has been extended

from traditional chemotherapy to novel modalities such as gene therapy, immunotherapy and radionuclide therapy.[60-61]

In this section, factors influencing the biodistribution of nanoparticles are first discussed. Then a special type of nanoparticles, renal clearable nanoparticles, is introduced. Finally, current research on using radiolabeled nanoparticles for cancer diagnosis and treatment is briefly reviewed.

2.1. Biodistribution of nanoparticles after systemic administration

There are two main delivery routes for nanoparticles in cancer treatment: local and systemic delivery. Intra tumoral (i.t.) injection is one of the most common local delivery methods.[62] Nanoparticles are usually injected into solid tumors following the guidance of imaging techniques. The nanoparticles will then diffuse throughout the injected area, thereby achieving a very high initial local tissue concentration for optimal tumor control. However, i.t. injection is a relatively invasive procedure and is limited to treat local tumors that are easily accessible.[63] On the other hand, intravenous (i.v.) injection, a systemic administration route, is more commonly used in nanomedicine. The nanoparticles are normally dispersed in physiological saline and administrated into the blood. After being injected, the nanoparticles will circulate in the body and passively accumulate at the tumor sites making use of the so-called enhanced permeation and retention (EPR) effect or actively by using targeting moieties.[64]

The EPR effect was first reported in 1986 and was hypothesized to originate from anatomical and pathophysiological difference between solid tumors and normal tissues.[65] Solid tumors usually have large gaps between endothelial cells in their vasculature, favoring the extravasation of nanoparticles (enhanced permeation). Due to the distorted structure of vasculature in solid tumors, nanoparticles can be retained at the tumor site while the extravasation back to blood was diminished (enhanced retention). It is widely accepted that only large nanoparticles can benefit from the EPR effect.[66] However, it has been reported that PEGylated gold nanoparticles as small as 2 nm also achieved high tumor uptake by the EPR effect.[67] Therefore, there is still more knowledge to be acquired to achieve complete understanding of the mechanism behind the EPR effect.

There have been numerous studies showing that only a small fraction of nanoparticles could eventually accumulate at the tumor site while most of the nanoparticles end up in liver or spleen.[68] The main reason for the high liver and spleen uptake is the capture of nanoparticles by the mononuclear-phagocytic system (MPS) (previously described as the reticuloendothelial system). As part of the immune system, the MPS filters blood and removes foreign particulates from the blood circulation. The Kupffer cells, a type of phagocytic immune cells which are usually located inside of liver sinusoids, account for most of the capture of nanoparticles from blood.[69] As soon as the nanoparticles are injected into the blood, they will be immediately exposed to serum proteins, eventually forming a structure called protein corona on the surface. The formation of protein corona increases the hydrodynamic diameter (HD) of the nanoparticles and makes the nanoparticles more easily recognizable by the macrophage cells (i.e. the opsonization effect).[70-71] More specifically, nanoparticles with HD larger than 5.5 nm are normally engulfed by the macrophage cells in the MPS organs, i.e. liver and spleen.[72] Although most of the nanoparticles used in medical application are biocompatible, there are still concerns related to long-term toxicity due to the slow clearance of nanoparticles from liver and spleen.[73]

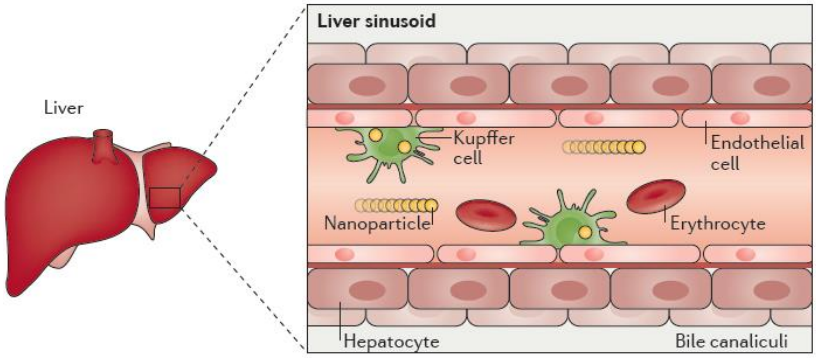

Figure 1.2.1. Schematic illustration of the clearance of nanoparticles by MPS. (Adapted from Ref [74] with permission. Copyright 2016, Nature Publishing Group).

To achieve high tumor uptake while minimizing the toxicity to the body, the non-specific uptake of nanoparticles by the MPS has to be suppressed. PEGylation is a common method to extend the circulation time of nanoparticles, thus improving the tumor uptake.[75-77] Polyethylene glycol (PEG) chains coated on nanoparticles could sterically shield the surface from aggregation, opsonization and phagocytosis, thereby prolonging the circulation time of

nanoparticles.[78] However, PEGylation could just extend the circulation time and delay the MPS capture. Most of the PEGylated nanoparticles will still end up in liver or spleen.[68, 74] Using biodegradable nanoparticles is a possible solution to the high liver uptake as reported in literature.[79] Instead of directly decreasing the liver uptake, these nanoparticles can decompose quickly into smaller fragments once in the MPS organs, thus allowing for faster clearance. Besides modifying the nanoparticles, the MPS capture can also be reduced by inhibiting the Kupffer cell phagocytosis using chemicals such as gadolinium chloride and chloroquine, hereby deactivating the liver macrophages.[80-82]

2.2. Renal clearable nanoparticles

An alternative solution to address the issue of high MPS uptake is to decrease the HD of nanoparticles to less than 5.5 nm. Such small nanoparticles can escape from MPS capture and be eliminated from the body through the urinary system. The clearance of nanoparticles via the urinary system, known as renal clearance, was first reported in 2007.[83] In this work, Choi et.al. studied the clearance of cysteine coated CdSe@ZnS quantum dots with HDs ranging from 4.6 nm to 7.2 nm. The renal clearance efficiency of the nanoparticles was quantified by measuring the fluorescence intensity in the bladder 2 h post injection. As shown in Figure 1.2.2, only nanoparticles with HD of less than 5.5 nm resulted in high fluorescence intensity in the bladder, indicating that the nanoparticles within this size range can be cleared by the kidneys.

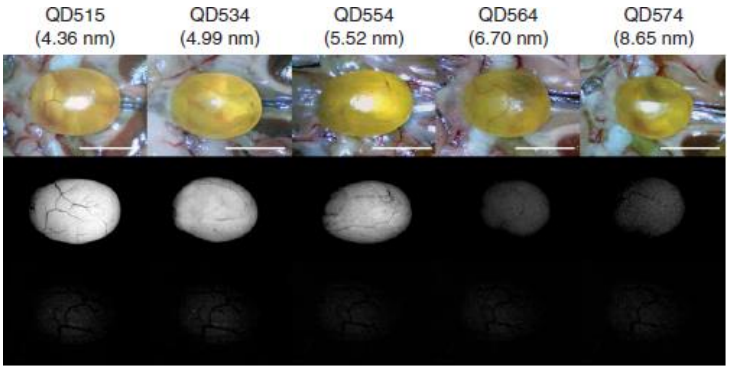

Figure 1.2.2. Imaging of mouse bladders after i.v. injection of Cys-CdSe@ZnS quantum dots with different HDs. Top: color images; middle: fluorescence images; bottom: fluorescence images of control groups. Scale bar=1 cm. (Adapted from Ref. [83] with permission. Copyright 2007, Nature Publishing Group).

In the past decades, the mechanism of renal clearance has been well-understood due to anatomical studies of kidneys going down to cell level.[84-85] In short, blood is filtered in the kidneys by the glomerular filtration membrane (GFM) which only enables substances less than 5.5 nm to pass. The GFM is a complex structure composed of endothelial glycocalyx, endothelial cells, the glomerular basement membrane (GBM) and podocytes. To reach the Bowman's space, the nanoparticles have to first pass the gap between the endothelial cells (70-90 nm). Subsequently, the nanoparticles will be filtered by the GBM which has a pore size between 2 and 8 nm. Then the nanoparticles are filtered by a layer of podocytes with a pore size of 4 to 11 nm. After passing this final layer, the nanoparticles reach the Bowman's space and are eventually transferred to the bladder. Because of the multiple-layer structure of GFM, the renal clearance efficiency of nanoparticles is determined by many factors, including size, charge, shape, composition, and interaction with different kidney compartments.

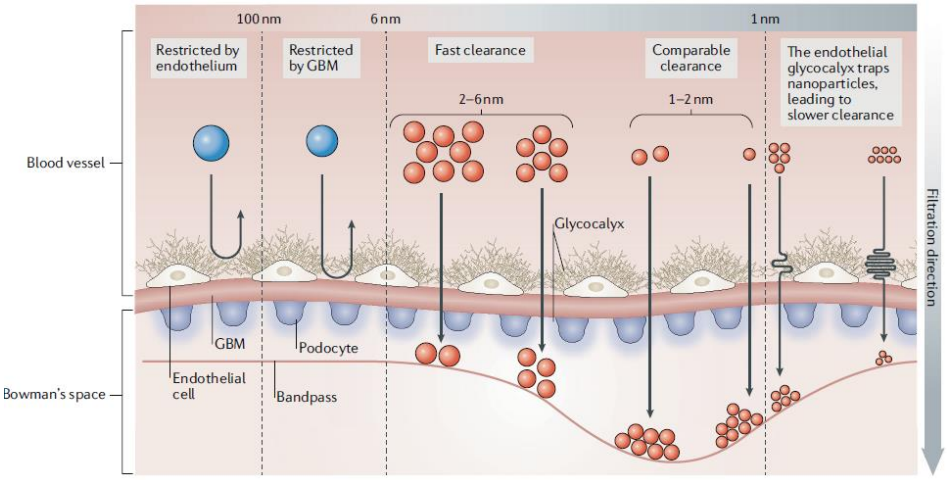

Figure 1.2.3. Schematic illustration of the size-scaling law in the glomerular filtration of nanoparticles (Adapted from Ref. [84] with permission. Copyright 2018, Nature Publishing Group).

The size of nanoparticles plays the dominant role in determining the renal clearance efficiency. As mentioned in the previous section, only nanoparticles with a HD of less than 5.5 nm can be readily cleared via urinary system. Smaller nanoparticles are usually cleared faster than the large ones. However, the clearance of sub-nanometer sized nanoparticles is relatively slower because of the interaction with the endothelial glycocalyx.

The surface charge of nanoparticles also plays an important role in renal clearance. As the endothelial glycocalyx, GBM and podocytes glycocalyx are all negatively charged, positively charged nanoparticles are generally cleared faster than neutral nanoparticles while the clearance of negatively charged nanoparticles is relatively slower. Interestingly, the clearance of highly negative charged nanoparticles is usually faster than the weakly negative charged ones.

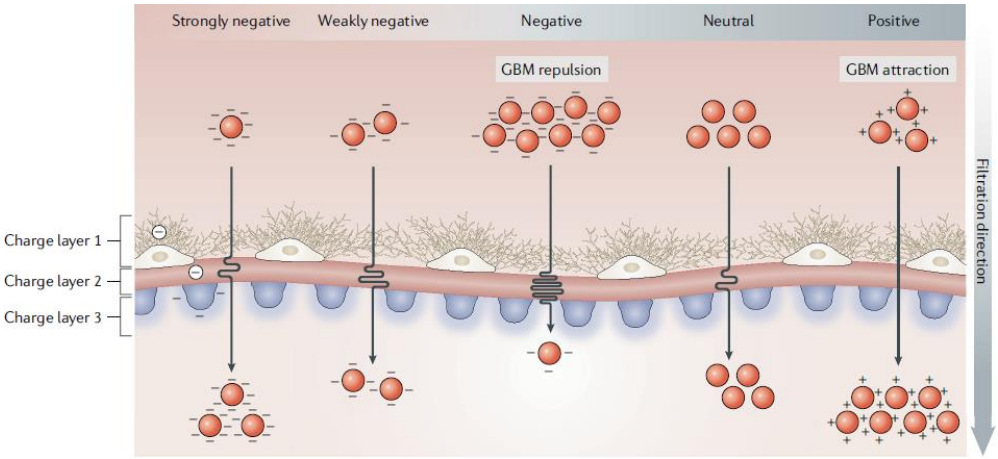

Figure 1.2.4. Schematic illustration of the charge-scaling law in the glomerular filtration of nanoparticles (Adapted from Ref. [84] with permission. Copyright 2018, Nature Publishing Group).

Besides spherical nanoparticles, nanoparticles in the shape of rods, tubes and sheets have also been well studied for medical applications. The geometry of these nanoparticles is characterized by a long and a short axis. If these particles have the right orientation in blood they could also pass the GFM.

Moreover, the core material of the nanoparticles also has an impact on the renal clearance efficiency. It has been experimentally proved that the renal clearance of nanoparticles can be enhanced by using low density core materials.[86-87] This effect is attributed to the fact that nanoparticles with higher density approach the blood vessel wall more rapidly and move slowly in the laminar blood flow during circulation. Thus, their elimination through the urinary system takes longer than that of the low-density ones.

Table 1.2.1. Representatives of renal clearable nanoparticles

	Core size (nm)/ HD (nm)	Zeta potential (mV)	Synthesis method	Renal clearance efficiency	Tumor uptake	Refs
GSH-AuNP	2.0/3.5	Negative	Thermal decomposition	**50.5% ID** at 24 h p.i., male BALB/c mice	-	[88]
GSH-[^{198}Au]AuNP	2.6/3.0	-50.0	Thermal decomposition	**42% ID** at 24 h p.i., male BALB/c mice	-	[89]
GSH-AuNP	2.5/3.3	Negative	Thermal decomposition	**~45% ID** at 24 h p.i., female BALB/c mice	**2.3% ID** at 12 h p.i., MCF-7 bearing mice	[90]
PEG-AuNP	2.3/5.5	Neutral	Thermal decomposition	**~50% ID** at 24 h p.i., female mice	**8.3% ID** at 12 h p.i., MCF-7 bearing mice	[67]
GSH-AuNP	2.6/3.4	-38.5	Thermal decomposition	**52.5% ID** at 24 h p.i., BALB/c mice	**0.18% ID** at 24 h p.i., glioma bearing mice	[91]
GSH/Cys-AuNP	2.3/2.9	-22.1	Thermal decomposition	**40-50% ID** at 24 h p.i., BALB/c mice	**4.36% ID** at 24 h p.i., PC-3 bearing mice; **9.48% ID** at 24 h p.i., LNCaP bearing mice	[92]
DOX-PEG-AuNP	2.1/4.7	Neutral	Thermal decomposition	**56% ID** at 24 h p.i., female CD-1 mice	**4.1% ID** at 12 h p.i., MCF-7 bearing mice	[93]
GSH-Au/Ag(1)NP	2.6/3.0	Negative	Thermal decomposition	**49.2% ID** at 24 h p.i., female BALB/c mice	-	[86]
GSH-Au/Ag(2)NP	2.6/3.0	Negative	Thermal decomposition	**45.4% ID** at 24 h p.i., female BALB/c mice	-	[86]
GSH-AgNP	2.6/3.0	Negative	Thermal decomposition	**50.7% ID** at 24 h p.i., female BALB/c mice	-	[86]
02PMIZ-AuNP	1.7/4.2	-11.4	Thermal decomposition	**60% ID** at 24 h p.i., normal mice	**8.6% ID** at 1 h p.i., 4T1 bearing mice	[94]
TG-AuNP	2.4/4.2	Negative	Thermal decomposition	**15% ID** at 72 h p.i., nude mice	**3.42% ID** at 12 h p.i., MCF-7 bearing mice	[95]
^{64}Cu-NOTA-GSH-AuNP	2.0/2.6	Negative	Thermal decomposition	**75% ID** at 24 h p.i., BALB/c mice	-	[96]
Phosphorylcholine-AuNC	1.6/-	-	$NaBH_4$ reduction	**92% ID** at 24h p.i., BALB/c mice	-	[97]
GSH--[^{64}Cu]CuNP	2.0/2.2	Negative	$NaBH_4$ reduction	**~80% ID** at 24 h p.i., female BALB/c mice	-	[98]
[^{64}Cu]CuS	4.3/5.6	+2.9	Chemical precipitation	**~95% ID** at 24h p.i., female Swiss mice	**0.22% ID** at 24 h p.i., 4T1 bearing mice	[99]
Cys-[^{99m}Tc]CdSe@ZnS	2.8/4.4	Zwitterionic	Hydrolysis-nucleation reaction	**75.13% ID** at 4h p.i., CD-1 mice	-	[83]
Cys-[^{99m}Tc]CdSe@ZnS	3.0/5.0	Zwitterionic	Hydrolysis-nucleation reaction	**62.18% ID** at 4h p.i., CD-1 mice	-	[83]
Cys-[^{99m}Tc]CdSe@ZnS	3.3/5.5	Zwitterionic	Hydrolysis-nucleation reaction	**43.65% ID** at 4h p.i., CD-1 mice	-	[83]
Dextran@i-IONP	3.0/5.0	-5.0	Cross-linking	High clearance at 24 h p.i., SD rats	-	[100]
GSH-Ag_2S NP	3.1/4.9	-11	Thermal decomposition	**85% ID** at 24h p.i., female nude mice	-	[101]
GSH-Ag_2Te NP	3/<4 nm	-23	N_2H_4 reduction	**93% ID** at 24h p.i., female nude mice	-	[87]
C dots	–/3.3	Neutral	Stöber method	**73% ID** at 48h p.i., NCRNU-M-M homozygous (nu/nu) nude mice	-	[102]

(Continued Table 1.2.1)

^{89}Zr-cRGDY-DFO-PEG-C' dots	-/6.5	Neutral	Stöber method	**~60% ID** at 1h p.i., NCRNU-M-M homozygous (nu/nu) nude mice	**12% ID** at 24 h p.i., M21 bearing mice	[103]
^{89}Zr-scFv-DFO-PEG-C' dots	-/7.3	Neutral	Stöber method	**~2% ID** at 72h p.i., female nude mice	**13% ID** at 24 h p.i., BT-474 bearing mice	[104]
^{89}Zr-PSMAi-DFO-PEG-C' dots	4.0/6.2	Neutral	Stöber method	**~45% ID** at 24h p.i., NOD.CB17-PrkdcSCID/J mice	**8.1% ID** at 24 h p.i., LNCap bearing mice	[105]
^{124}I-cRGD-PEG-C' dots	-/-	-	Stöber method	**Strong bladder signal** at 0.5h p.i., Nestin-tv-a Ink4a-Arf-/- mice	**7% ID** at 24 h p.i., AB3 bearing mice	[106]
^{177}Lu-DOTA-αMSH-PEG-Cy5-C′ dot	-/5.8	Neutral	Stöber method	**~40% ID** at 24h p.i., NOD.CB17-PrkdcSCID/J mice	**9.3% ID** at 24 h p.i., M21 bearing mice **10.6% ID** at 24 h p.i., B16F10 bearing mice	[107]
BODIPY derivatives	-/5.6	+35	Self-assemble	**70% ID** at 12h p.i., nude mice	11.5 SBR at 3 h p.i., HELA bearing mice	[108]
Porphyrin@ silica dots	6.2/7.0	-16	Stöber method	**Strong fluorescence in urine** 1h p.i. BALB/c mice	-	[109]

'-' means unknown or unreported; AuNP, gold nanoparticles; GSH, glutathione; SD rats, Sprague-Dawley rats; BODIPY, boron dipyrromethene; SBR ratio, signal-to-background ratio; HD, hydrodynamic diameter; %ID, percentage of injected dose; Cys, cysteine; TG, thiolated glucose; PEG, polyethylene glycol; PMIZ2, PEG linked imidazole ring.

To better understand the state of art on the development of renal clearable nanoparticles, several representative studies are summarized in Table 1.2.1. Over the past 17 years since the first report of renal clearable nanoparticles, there has been only a small number of papers published in this filed. Among these published papers, there are mainly three types of nanoparticles reported to be renal clearable: gold nanoparticles coated by glutathione (GSH) or PEG, PEG coated silica nanoparticles (the C dot and C' dot) and a few quantum dots. Besides the inorganic nanoparticles, a few self-assembled organic nanoparticles have also been reported to be renal clearable.

The GSH or PEG coated gold nanoparticles (GSH-AuNPs and PEG-AuNPs) are normally prepared by the thermal decomposition of the polymeric Au(I) thiolates.[67, 88] The nanoparticles produced using this method are normally as small as 2~3 nm in diameter and 3~5 nm in HD. More importantly, these nanoparticles were found to have emission at near infrared region (NIR) which makes them detectable by fluorescent imaging.[110] Extensive work has been carried out by the group of prof. Jie Zheng from the University of Texas at Dallas on the application of renal clearable gold nanoparticles for imaging and drug delivery in cancer treatment. The high renal clearance efficiency and tumor uptake have been verified

in various cancer models including glioblastoma[91], breast cancer[67, 90, 93] and prostate cancer[92]. Moreover, Tan et. al. reported the targeting of metastasized tumor cells with renal clearable gold nanoparticles using charge reversible surface modification.[94] These nanoparticles remain negatively charged in blood but turn positively charged at the tumor sites when at slightly acidic environment. Therefore, tumor uptake was improved due to the attraction of the nanoparticles by the negatively charged cell membrane. Another interesting work based on gold nanoparticles was reported by Wang et. al. in 2019.[95] Instead of GSH and PEG, the gold nanoparticles were coated by thiolated glucose (TG) which naturally targets the tumor cells. However, the clearance of the TG-AuNP was found to be much slower when compared to GSH-AuNPs.

Another type of renal clearable inorganic nanoparticles is the Cornell dot (C dot). Developed by the group of prof. Ulrich Wiesner from Cornell University, the C dot has been approved for clinical trials in 2011 by the FDA. It is worth mentioning that this was the first time that the FDA approved the usage of inorganic nanomaterials for human applications. The C dots are composed of PEG coated silica nanoparticles incorporating fluorescent dye molecules and ^{124}I. The HD of a typical C dot is as small as 3.3 nm, leading to a high renal clearance efficiency.[102] In 2015, a new version of C dot, the prime Cornell dot (C' dot) has been invented by Ma et.al.[111] The C' dot was synthesized in a water-based system instead of in ethanol, making it more convenient for biological applications. In addition, the PEG coating methodology has been simplified and optimized with minimal particle aggregation. Most importantly, the incorporation efficiency of the fluorescent dyes in C' dots has been greatly improved, significantly reducing the treatment costs. The C' dots have been modified by various targeting agents such as cRGDY, scFv, αMSH and PSMAi and have shown high tumor accumulation and fast clearance from the body.[103-107] Motivated by the positive results from all these preclinical studies, the first clinical trial of the C' dot has been initiated in 2021 to evaluate the safety and tumor control efficacy.

Based on the discussion above, a few common aspects on the design of renal clearable nanoparticles can be concluded. First, the synthesis of the nanoparticles is always performed following a one-pot procedure. Small molecules or short PEG molecules are usually used as the capping ligands to achieve small HD values. Besides, the capping ligands must be highly resistant to protein absorption to maintain the small HD during blood circulation. There has

been no report on synthesizing renal clearable nanoparticles by first making nanoparticles with a large HD then reducing the HD by exchanging the surface ligands. It is likely that the surface modification of nanoparticles requires very precise control on the reaction kinetics to avoid the formation of aggregates, making this process very challenging. Second, there is always a size selection step required after the synthesis of renal clearable nanoparticles. This can be achieved by simple purification methods such as passing the nanoparticles through size exclusion columns (e.g., PD-10) and syringe filters or by more complex techniques such as gel permeation chromatography (GPC). Third, linking tumor targeting agents can improve the tumor uptake of the renal clearable nanoparticles, mostly by increasing the retention at the tumor sites. However, the renal clearance of these targeted nanoparticles might take longer time due to the increased HD.

2.3. Radiolabeled nanoparticles for cancer diagnosis and treatment

The application of nanotechnology in nuclear medicine was first reported on using liposomes and polymeric nanoparticles such as polymersomes and micelles as radionuclide carriers. In case of inorganic nanoparticles, their applications in cancer treatment used to be limited to radiosensitization in EBRT, for which nanoparticles with high Z number are desired.[112] In the past decades, the application of inorganic nanoparticles as carriers for radionuclides has raised more and more attention. Compared to the conventional antibody-chelator modality, using nanoparticles can improve the circulation time of radionuclides in the body and eventually increase tumor uptake.[61, 113] As the size, shape, composition and surface properties of the nanoparticles can be finely tuned, the biodistribution of radionuclides loaded on these nanoparticles can be well anticipated and likely controlled. In this section, the radiolabeling methods used for nanoparticles will be briefly reviewed and discussed.

As shown in Figure 1.2.5, the radiolabeling of nanoparticles can be classified into six main approaches: chelation, surface adsorption, encapsulation, radionuclide doping, cation exchange and bombardment by neutrons or protons.

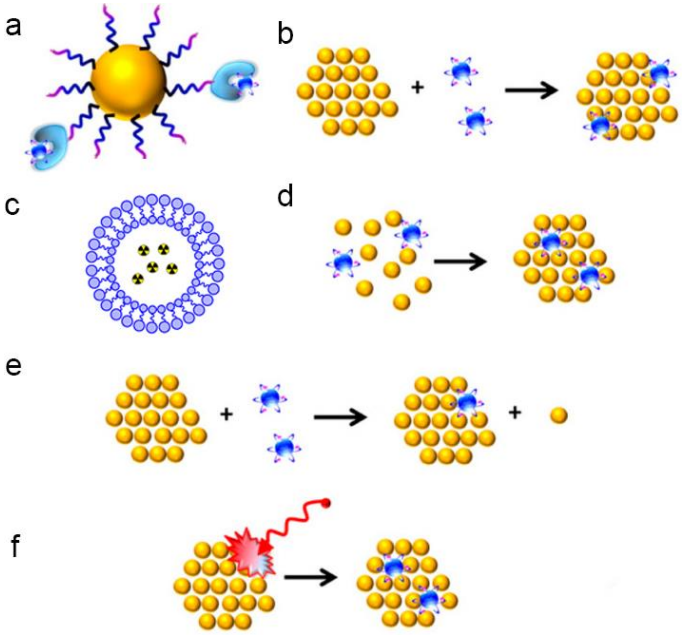

Figure 1.2.5. Radiolabeling of nanoparticles via a) chelation; b) surface adsorption; c) encapsulation; d) radionuclide doping; e) cation exchange and f) bombardment by neutrons or protons. (Adapted from Ref. [114-115] with permission. Copyright 2017, American Chemical Society).

Due to the large surface area of the nanoparticles, chelators can be easily linked on the surface of nanoparticles to complex with radionuclides. For instance, Chen et. al. reported the radiolabeling of DFO modified silica nanoparticles (C' dot) with ^{89}Zr with nearly 100% radiolabeling efficiency and supreme radiochemical stability both *in vitro* and *in vivo*.[103-105] NOTA modified AuNPs were reported to be radiolabeled with ^{64}Cu with high radiolabeling efficiency and radiochemical stability.[96] The radiolabeling of chelator modified nanoparticles is simple and highly reproducible due to the well-established protocols when using conventional chelators. However, there are a few disadvantages of this chelator-based method. The most important one is the change of surface charge and HD of the nanoparticles after the linkage of chelators. Besides, the radiolabeling with some radionuclide and chelator combinations require harsh conditions such as high temperature or extreme pH values.[42] These harsh conditions might disrupt the colloidal stability of the nanoparticles and lead to the formation of aggregates. The stability of the bonds between chelators and the nanoparticles posts another potential threat on the *in vivo* radiochemical stability. The

complex environment in the body might induce the release of chelators from the nanoparticles due to the degradation of the linking bonds.[116]

Nanoparticles can also be directly radiolabeled by chemical adsorption according to the Pearson's hard and soft acids and bases (HSAB) theory. All the Lewis acids and bases could be classified into either hard acids (e.g. Zr, Y, Sr, Sc) and bases (e.g. O) or soft acids (e.g. Ag, Au, Cu) and bases (e.g. S, I, Br, At).[117] The hard acids react faster and form stronger bonds with the hard bases while the soft acids react faster and form stronger bonds with the soft bases. A typical example is the radioiodination of gold nanoparticles. The radioactive iodine has high affinity to gold and can form stable covalent bonds with the gold atoms on the surface of gold nanoparticles.[118-121] Shaffer et.al. reported the chelator-free radiolabeling of amorphous silica nanoparticles with ^{89}Zr, ^{68}Ga, ^{90}Y, ^{111}In, ^{177}Lu and ^{64}Cu by using the interaction between O^- sites on the surface of silica nanoparticles and the radioactive ions.[122] The radiolabeling efficiency for all radionuclides was as high as 99%. Moreover, these radionuclides were found to be tightly retained within the nanoparticles even after being challenged by serum or concentrated chelator solutions, except for ^{64}Cu. The low radiochemical stability of ^{64}Cu was attributed to the mismatch between Cu and O, a soft acid and a hard base. After adding extra thiol groups (-SH) on the silica nanoparticles, the retention of ^{64}Cu on the carriers was significantly improved.[123] Besides chemical adsorption, physical adsorption has also been applied for radiolabeling nanoparticles. Karpov et al. developed a universal method for radiolabeling nanoparticles made of polylactic acid, silica, gold and iron oxide with ^{99m}Tc and ^{188}Re.[124] The $^{99m}TcO_4^-$ and $^{188}ReO_4^-$ were precipitated on the surface of the nanoparticles and turned into insoluble $^{99m}TcO_2$ and $^{188}ReO_2$ nanoaggregates which were tightly adopted on the surface of the nanoparticles, leading to high radiolabeling efficiency and high radiochemical stability.

Despite the simplicity of these adsorption-based methods, there is still concern on the *in vivo* radiochemical stability of the products. The radionuclides are likely to bond to reactive sites both inside and outside of the nanoparticles.[103, 125] The outer-bound radionuclides might be stripped out from the carrier when interacting with the proteins in blood. To avoid the dissociation of the absorbed radionuclides from the nanoparticles, various approaches have been proposed, such as adding an extra layer on top of the nanoparticles and increasing the affinity to the nanoparticles by pre-treating the radionuclides before radiolabeling.[125-127]

Doping is a common way to introduce "impurities" into the lattice structure of semiconductors to achieve different electrical and optical properties.[128-129] The doping of lanthanide ions into iron oxide nanoparticles has also been reported to improve their performance as magnetic resonance imaging (MRI) contrast agents.[130] Since trace amounts of radionuclides could already account for high level of radioactivity, doping the inside structure of nanoparticles with radionuclides provides another route for radiolabeling of nanoparticles. To make sure that radionuclides are properly incorporated into the structure of nanoparticles, it is critical to find the right combination between the host materials and the dopants. In many cases, the radionuclides could be mixed with the non-radioactive precursors of the same element. Due to the same chemical properties, the formation of nanoparticles usually remains undisturbed. The radiochemical stability is always improved when applying radionuclide doping, as the radionuclides are stably trapped inside the nanoparticles. As reported in the literature, ^{64}Cu has been successfully incorporated into CuS nanoparticles by using a mixture of ^{64}Cu with nonradioactive $CuCl_2$.[99] In the work of Zhou et. al., PEG-AuNPs have been radiolabeled by introducing $^{198}AuCl_4^-$ to the reaction.[89] Cerium oxide nanoparticles have also been radiolabeled with ^{141}Ce for SPECT imaging.[131] ^{111}Ag with a half-life time of 7.45 days and the emission of highly energetic β^- particles has been previously incorporated into silver nanoparticles for antimicrobial applications.[132] In other cases, the radionuclides and nanoparticles are composed of different elements. In the literature, ^{111}In[133], ^{68}Ga[134-135], ^{64}Cu[136-139], ^{103}Pd[140], ^{89}Zr[135] and ^{89}Sr[135] have been radiolabeled on gold nanoparticles while ^{111}In[141] and ^{89}Zr[142] have been radiolabeled on iron oxide nanoparticles. $BaSO_4$ nanoparticles have also been used as the carrier of ^{89}Zr, ^{111}In, ^{177}Lu and ^{224}Ra.[143]

Although radionuclide doping is simple and straightforward, its application is still limited. As the radionuclides are usually supplied in strong acid or bases, the formation of nanoparticles might be interfered due to the change of pH values after the addition of the radionuclides. Besides, the lattice mismatch between the dopant and the host material must be considered which might result in low radiolabeling efficiency.[144] Furthermore, the specific activity of the nanoparticles radiolabeled by radionuclide doping might be lower compared to the chelator-based products. To address the current drawbacks, more combinations between radionuclides and host nanoparticles have to be explored

experimentally or theoretically using density functional theory (DFT) calculations. It is also important to find a fast and mild synthesis method to avoid the loss of activity during the synthesis and ease the radiation burden on the experimentalists.

Encapsulation of radionuclides inside the cavity of nanoparticles is also a typical radiolabeling method. Self-assembled nanoparticles such as liposomes and polymersomes have a hydrophilic cavity while micelles have a hydrophobic core. When the radionuclides are transferred into the core of these nanoparticles, high radiolabeling could be achieved by trapping the radionuclides via chelation or precipitation depending on the particle type.[145]

Cation exchange has been widely utilized in the processing of ionic and semiconductor nanocrystals.[146] The radionuclide cations can react at the surface of the nanoparticles and replace the non-radioactive atoms. High radiolabeling efficiency and high radiochemical stability can be achieved using this method as reported in the literature. However, a long contact time between the radionuclides and the nanoparticles is normally necessary for successful radiolabeling using this method, hindering its application for radiolabeling with short-lived radionuclides.

Nanoparticles can also be first prepared and then activated by bombarding them with thermal neutrons or with protons. The stable nuclides composing the nanoparticles can then be converted into the desired radionuclide by inducing a nuclear reaction.[116] However, the organic coatings as well as the biological moieties (e.g., peptides) of the nanoparticles might be damaged due to the high temperature or strong radiation field.[113]

Despite the exciting outcomes from the preclinical research, the translation of nanomaterials-based radiopharmaceuticals to clinical trials is rarely reported, mainly due to radiotoxicity originating from high liver and spleen uptake. In addition, the *in vivo* radiochemical stability of the radiolabeled nanoparticles might differ from what had been determined *in vitro*. Regulatory considerations also limit the clinical application of nanocarriers. It remains challenging to obtain the Good Manufacturing Practice (GMP) certification for the manufacturing of nanoparticles. Other drawbacks such as extra costs of the nanoparticles and difficulties on scaling-up should also be properly addressed to expand the potential of radiolabeled nanoparticles in clinical applications.

3. Outline of this thesis

The research goal of this thesis is to design nanoparticle-based radiopharmaceuticals for cancer treatment. Ultra-small inorganic nanoparticles which are likely to be quickly cleared from the body were chosen as the carriers for radionuclides to minimize the potential side effects on healthy tissues. Furthermore, extra benefits of using nanoparticles as radionuclide carriers were explored. The outline of this thesis is given below.

In **Chapter 2**, the radiolabeling of core-shell structured gold nanoparticles and platinum-gold bimetallic nanoparticles with ^{166}Dy is described. The radiolabeling with ^{166}Dy was achieved via the co-reduction of ^{166}Dy ions with gold salts. The influence of various factors on the radiolabeling efficiency including different initial Dy:Au ratios, addition of Pt salts during the synthesis and the addition of extra layer of gold was studied. The retention of ^{166}Ho, the daughter of ^{166}Dy, was measured in various solvents to understand the mechanism behind the stabilization effect of the nanoparticles on internally converted radionuclides.

In **Chapter 3**, ultra-small PEG-AuNPs were synthesized and radiolabeled with ^{125}I via chemical adsorption. After the characterization of physical and radiochemical properties, the cell uptake and sub-cellular distribution of the ^{125}I-PEG-AuNPs were studied *in vitro*. Finally, the *in vitro* tumor killing efficiency of the ^{125}I-PEG-AuNPs was evaluated using both 2D and 3D U87 cell models.

In **Chapter 4**, ultra-small GSH-AuNPs and GSH-Ag_2TeNPs with similar core sizes and hydrodynamic diameters were synthesized, modified with DTPA and radiolabeled with ^{111}In. The cellular distribution of these two types of nanoparticles were studied by cell fractionation assay and/or fluorescence imaging. Finally, the *in vitro* tumor killing efficiency of the ^{111}In-DTPA-AuNPs and ^{111}In-DTPA-Ag_2TeNPs were determined using 2D and 3D U87 cell models.

In **Chapter 5**, ^{212}Pb was radiolabeled on various inorganic nanoparticles via the co-reduction or the co-precipitation method. The radiochemical stability of ^{212}Pb and the internally converted ^{212}Bi was studied using a chelator challenge assay.

In **Chapter 6**, general conclusions and outlook are given based on the results of previous chapters.

References

[1] IAEA, *Radiotherapy in Cancer Care: Facing the Global Challenge* **2017**.
[2] T. I. Kostelnik, C. Orvig, *Chemical Reviews* **2019**, *119*, 902-956.
[3] J. K. Willmann, N. van Bruggen, L. M. Dinkelborg, S. S. Gambhir, *Nat Rev Drug Discov* **2008**, *7*, 591-607.
[4] G. W. Barendsen, *Nature* **1962**, *193*, 1153-1155.
[5] J. P. Pouget, I. Navarro-Teulon, M. Bardies, N. Chouin, G. Cartron, et al., *Nat Rev Clin Oncol* **2011**, *8*, 720-734.
[6] F. Buchegger, F. Perillo-Adamer, Y. M. Dupertuis, A. Bischof Delaloye, *European Journal of Nuclear Medicine and Molecular Imaging* **2006**, *33*, 1352-1363.
[7] A. Fasih, H. Fonge, Z. Cai, J. V. Leyton, I. Tikhomirov, et al., *Breast Cancer Research and Treatment* **2012**, *135*, 189-200.
[8] P. Jean-Pierre, S. Lore, R. Laure, C. Nicolas, B. Manuel, et al., *Radiation Research* **2008**, *170*, 192-200.
[9] S. Lore, B. Samir, G. Véronique, B.-M. Caroline, B. Vincent, et al., *Journal of Nuclear Medicine* **2009**, *50*, 2033.
[10] I. K. Amin, S. J. Adelstein, *Journal of Nuclear Medicine* **2005**, *46*, 4S.
[11] W. J. Cannan, D. S. Pederson, *Journal of Cellular Physiology* **2016**, *231*, 3-14.
[12] Endo, K. F. Eckerman, A. Endo, MIRD Radionuclide Data and Decay Schemes, The Society of Nuclear Medicine, Reston (VA), **2007**.
[13] A. Ku, V. J. Facca, Z. Cai, R. M. Reilly, *EJNMMI Radiopharm Chem* **2019**, *4*, 27.
[14] M. Schlumberger, S. Leboulleux, B. Catargi, D. Deandreis, S. Zerdoud, et al., *The Lancet Diabetes & Endocrinology* **2018**, *6*, 618-626.
[15] A. L. Ho, R. K. Grewal, R. Leboeuf, E. J. Sherman, D. G. Pfister, et al., *New England Journal of Medicine* **2013**, *368*, 623-632.
[16] B. de Keizer, H. P. F. Koppeschaar, P. M. J. Zelissen, C. J. M. Lips, P. P. van Rijk, et al., *European Journal of Nuclear Medicine* **2001**, *28*, 198-202.
[17] R. Salem, R. D. Hunter, *Int J Radiat Oncol Biol Phys* **2006**, *66*, S83-88.
[18] G. Vesselle, I. Petit, S. Boucebci, T. Rocher, S. Velasco, et al., *Diagn Interv Imaging* **2015**, *96*, 547-562.
[19] M. A. Westcott, D. M. Coldwell, D. M. Liu, J. F. Zikria, *Adv Radiat Oncol* **2016**, *1*, 351-364.
[20] J. F. W. Nijsen, B. A. Zonnenberg, J. R. W. Woittiez, D. W. Rook, I. A. Swildens-van Woudenberg, et al., *European Journal of Nuclear Medicine* **1999**, *26*, 699-704.
[21] M. L. J. Smits, J. F. W. Nijsen, M. A. A. J. van den Bosch, M. G. E. H. Lam, M. A. D. Vente, et al., *The Lancet Oncology* **2012**, *13*, 1025-1034.
[22] S. V. Smith, N. Di Bartolo, S. Mirzadeh, R. M. Lambrecht, F. Knapp Jr, et al., **1995**, *46*, 759-764.
[23] M. S. Hofman, J. Violet, R. J. Hicks, J. Ferdinandus, S. P. Thang, et al., *The Lancet Oncology* **2018**, *19*, 825-833.
[24] T. Derlin, S. Schmuck, *The Lancet Oncology* **2018**, *19*, e372.
[25] J. Strosberg, G. El-Haddad, E. Wolin, A. Hendifar, J. Yao, et al., *New England Journal of Medicine* **2017**, *376*, 125-135.
[26] C. Müller, C. A. Umbricht, N. Gracheva, V. J. Tschan, G. Pellegrini, et al., *European Journal of Nuclear Medicine and Molecular Imaging* **2019**, *46*, 1919-1930.
[27] K. E. Baidoo, K. Yong, M. W. Brechbiel, *Clinical Cancer Research* **2013**, *19*, 530-537.

[28] L. Marcu, E. Bezak, B. J. Allen, *Critical Reviews in Oncology/Hematology* **2018**, *123*, 7-20.
[29] M. M. Sathekge, F. Bruchertseifer, M. Vorster, A. Morgenstern, I. O. Lawal, *European Journal of Nuclear Medicine and Molecular Imaging* **2021**, *49*, 30-46.
[30] C. Parker, S. Nilsson, D. Heinrich, S. I. Helle, J. M. O'Sullivan, et al., *New England Journal of Medicine* **2013**, *369*, 213-223.
[31] R. M. De Kruijff, H. T. Wolterbeek, A. G. Denkova, in *Pharmaceuticals, Vol. 8*, **2015**, pp. 321-336.
[32] G. Wang, R. de Kruijff, M. C. A. Stuart, E. Mendes, H. T. Wolterbeek, et al., *Soft Matter* **2013**, *9*, 727-734.
[33] R. M. Kruijff, R. Raavé, A. Kip, J. Molkenboer-Kuenen, A. Morgenstern, et al., *Scientific Reports* **2019**, *9*.
[34] U. Holzwarth, I. Ojea Jimenez, L. Calzolai, *EJNMMI Radiopharm Chem* **2018**, *3*, 9.
[35] R. W. Howell, V. Narra, K. S. R. Sastry, D. V. J. R. r. Rao, **1993**, *134 1*, 71-78.
[36] M. R. Raymond, K. Reza, G. C. Ross, P. Nicole, S. Jasbir, et al., *Journal of Nuclear Medicine* **2000**, *41*, 429.
[37] C. Zhongli, C. Zhuo, E. B. Kristy, A. S. Deborah, M. R. Raymond, et al., *Journal of Nuclear Medicine* **2008**, *49*, 1353.
[38] A. Kassis, F. Fayad, B. Kinsey, K. Sastry, S. Adelstein, *Radiation research* **1989**, *118*, 283-294.
[39] G. Makrigiorgos, A. Kassis, J. Baranowska-Kortylewicz, K. McElvany, M. Welch, et al., **1989**, *118*, 532-544.
[40] C. Rebischung, D. Hoffmann, L. Stéfani, M. D. Desruet, K. Wang, et al., *International Journal of Radiation Biology* **2008**, *84*, 1123-1129.
[41] A. Dash, F. F. Knapp, R. A. M. Pillai, *Current Radiopharmaceuticals* **2013**, *6*, 152-180.
[42] E. W. Price, C. Orvig, *Chem Soc Rev* **2014**, *43*, 260-290.
[43] Y. Sun, C. J. Anderson, T. S. Pajeau, D. E. Reichert, R. D. Hancock, et al., *Journal of Medicinal Chemistry* **1996**, *39*, 458-470.
[44] S. Liu, D. S. Edwards, *Bioconjugate Chemistry* **2001**, *12*, 630-634.
[45] B. M. Zeglis, P. Mohindra, G. I. Weissmann, V. Divilov, S. A. Hilderbrand, et al., *Bioconjugate Chemistry* **2011**, *22*, 2048-2059.
[46] S. M. Larson, J. A. Carrasquillo, N.-K. V. Cheung, O. W. Press, *Nature Reviews Cancer* **2015**, *15*, 347-360.
[47] P. S. Steeg, *Nature Reviews Cancer* **2016**, *16*, 201-218.
[48] G. L. Zwicke, G. Ali Mansoori, C. J. Jeffery, *Nano Reviews* **2012**, *3*, 18496.
[49] D. C. Koboldt, R. S. Fulton, M. D. McLellan, H. Schmidt, J. Kalicki-Veizer, et al., *Nature* **2012**, *490*, 61-70.
[50] D. A. Silver, I. Pellicer, W. R. Fair, W. D. W. Heston, C. Cordon-Cardo, *Clinical Cancer Research* **1997**, *3*, 81-85.
[51] O. C. Farokhzad, J. Cheng, B. A. Teply, I. Sherifi, S. Jon, et al., *Proceedings of the National Academy of Sciences of the United States of America* **2006**, *103*, 6315-6320.
[52] M. Eiber, T. Maurer, M. Souvatzoglou, A. J. Beer, A. Ruffani, et al., *Journal of Nuclear Medicine* **2015**, *56*, 668-674.
[53] S. Welt, C. R. Divgi, A. M. Scott, P. Garin-Chesa, R. D. Finn, et al., *Journal of Clinical Oncology* **1994**, *12*, 1193-1203.
[54] B. M. Privé, M. A. Boussihmad, B. Timmermans, W. A. van Gemert, S. M. B. Peters, et al., *European Journal of Nuclear Medicine and Molecular Imaging* **2023**, *50*, 1906-1918.

[55] M. Eder, M. Schäfer, U. Bauder-Wüst, W. E. Hull, C. Wängler, et al., *Bioconjugate Chemistry* **2012**, *23*, 688-697.
[56] O. Sartor, J. De Bono, K. N. Chi, K. Fizazi, K. Herrmann, et al., *New England Journal of Medicine* **2021**, *385*, 1091-1103.
[57] A. Loktev, T. Lindner, W. Mier, J. Debus, A. Altmann, et al., *Journal of Nuclear Medicine* **2018**, *59*, 1423-1429.
[58] C. Kratochwil, P. Flechsig, T. Lindner, L. Abderrahim, A. Altmann, et al., *Journal of Nuclear Medicine* **2019**, *60*, 801-805.
[59] J. Shi, P. W. Kantoff, R. Wooster, O. C. Farokhzad, *Nat Rev Cancer* **2017**, *17*, 20-37.
[60] M. J. Mitchell, M. M. Billingsley, R. M. Haley, M. E. Wechsler, N. A. Peppas, et al., *Nat Rev Drug Discov* **2021**, *20*, 101-124.
[61] J. Ge, Q. Zhang, J. Zeng, Z. Gu, M. Gao, *Biomaterials* **2020**, *228*, 119553.
[62] E. P. Goldberg, A. R. Hadba, B. A. Almond, J. S. Marotta, *J Pharm Pharmacol* **2002**, *54*, 159-180.
[63] I. Melero, E. Castanon, M. Alvarez, S. Champiat, A. Marabelle, *Nature Reviews Clinical Oncology* **2021**, *18*, 558-576.
[64] M. T. Manzari, Y. Shamay, H. Kiguchi, N. Rosen, M. Scaltriti, et al., *Nat Rev Mater* **2021**, *6*, 351-370.
[65] Y. Matsumura, H. J. C. r. Maeda, **1986**, *46*, 6387-6392.
[66] D. Kalyane, N. Raval, R. Maheshwari, V. Tambe, K. Kalia, et al., *Materials Science and Engineering: C* **2019**, *98*, 1252-1276.
[67] J. Liu, M. Yu, X. Ning, C. Zhou, S. Yang, et al., *Angew Chem Int Ed Engl* **2013**, *52*, 12572-12576.
[68] Q. Dai, S. Wilhelm, D. Ding, A. M. Syed, S. Sindhwani, et al., *ACS Nano* **2018**, *12*, 8423-8435.
[69] K. M. Tsoi, S. A. MacParland, X. Z. Ma, V. N. Spetzler, J. Echeverri, et al., *Nat Mater* **2016**, *15*, 1212-1221.
[70] C. D. Walkey, J. B. Olsen, F. Song, R. Liu, H. Guo, et al., *ACS Nano* **2014**, *8*, 2439-2455.
[71] C. D. Walkey, J. B. Olsen, H. Guo, A. Emili, W. C. W. Chan, *Journal of the American Chemical Society* **2012**, *134*, 2139-2147.
[72] M. Yu, J. Zheng, *ACS Nano* **2015**, *9*, 6655-6674.
[73] S. Fraga, A. Brandão, M. E. Soares, T. Morais, J. A. Duarte, et al., *Nanomedicine: Nanotechnology, Biology and Medicine* **2014**, *10*, 1757-1766.
[74] S. Wilhelm, A. J. Tavares, Q. Dai, S. Ohta, J. Audet, et al., *Nature Reviews Materials* **2016**, *1*, 16014.
[75] A. S. Karakoti, S. Das, S. Thevuthasan, S. Seal, *Angewandte Chemie International Edition* **2011**, *50*, 1980-1994.
[76] K. G. Neoh, E. T. Kang, *Polymer Chemistry* **2011**, *2*, 747-759.
[77] X. Xia, M. Yang, Y. Wang, Y. Zheng, Q. Li, et al., *ACS Nano* **2012**, *6*, 512-522.
[78] J. V. Jokerst, T. Lobovkina, R. N. Zare, S. S. Gambhir, *Nanomedicine* **2011**, *6*, 715-728.
[79] W. Lee, G. Il An, H. Park, S. Sarkar, Y. S. Ha, et al., *ACS Nano* **2021**, *15*, 17348-17360.
[80] E. Husztik, G. Lazar, A. Parducz, *British Journal of Experimental Pathology* **1980**, *61*, 624-630.
[81] P. Diagaradjane, A. Deorukhkar, J. G. Gelovani, D. M. Maru, S. Krishnan, *ACS Nano* **2010**, *4*, 4131-4141.
[82] J. Wolfram, S. Nizzero, H. Liu, F. Li, G. Zhang, et al., *Scientific Reports* **2017**, *7*.

[83] H. S. Choi, W. Liu, P. Misra, E. Tanaka, J. P. Zimmer, et al., *Nat Biotechnol* **2007**, *25*, 1165-1170.
[84] B. Du, M. Yu, J. Zheng, *Nature Reviews Materials* **2018**, *3*, 358-374.
[85] P. Cheng, K. Pu, *Nature Reviews Materials* **2021**, *6*, 1095-1113.
[86] S. Tang, C. Peng, J. Xu, B. Du, Q. Wang, et al., *Angew Chem Int Ed Engl* **2016**, *55*, 16039-16043.
[87] L. M. Nieves, Y. C. Dong, D. N. Rosario-Berrios, K. Mossburg, J. C. Hsu, et al., *ACS Appl Mater Interfaces* **2022**, *14*, 34354-34364.
[88] C. Zhou, M. Long, Y. Qin, X. Sun, J. Zheng, *Angew Chem Int Ed Engl* **2011**, *50*, 3168-3172.
[89] C. Zhou, G. Hao, P. Thomas, J. Liu, M. Yu, et al., *Angew Chem Int Ed Engl* **2012**, *51*, 10118-10122.
[90] J. Liu, M. Yu, C. Zhou, S. Yang, X. Ning, et al., *J Am Chem Soc* **2013**, *135*, 4978-4981.
[91] C. Peng, X. Gao, J. Xu, B. Du, X. Ning, et al., *Nano Res* **2017**, *10*, 1366-1376.
[92] M. Yu, C. Zhou, L. Liu, S. Zhang, S. Sun, et al., *Angew Chem Int Ed Engl* **2017**, *56*, 4314-4319.
[93] C. Peng, J. Xu, M. Yu, X. Ning, Y. Huang, et al., *Angew Chem Int Ed Engl* **2019**, *58*, 8479-8483.
[94] Y. Tan, K. He, B. Tang, H. Chen, Z. Zhao, et al., *ACS Nano* **2020**, *14*, 13975-13985.
[95] Y. Wang, S. Ma, Z. Dai, Z. Rong, J. Liu, *Nanoscale* **2019**, *11*, 16336-16341.
[96] F. Chen, S. Goel, R. Hernandez, S. A. Graves, S. Shi, et al., *Small* **2016**, *12*, 2775-2782.
[97] A. Baghdasaryan, F. Wang, F. Ren, Z. Ma, J. Li, et al., *Nat Commun* **2022**, *13*, 5613.
[98] S. Yang, S. Sun, C. Zhou, G. Hao, J. Liu, et al., *Bioconjug Chem* **2015**, *26*, 511-519.
[99] M. Zhou, J. Li, S. Liang, A. K. Sood, D. Liang, et al., *ACS Nano* **2015**, *9*, 7085-7096.
[100] J.-w. Kim, J. Cheong, H. Cheong, J. G. Yoon, J.-Y. Jung, et al., *ACS Applied Nano Materials* **2021**, *4*, 12943-12948.
[101] J. C. Hsu, E. D. Cruz, K. C. Lau, M. Bouche, J. Kim, et al., *Chem Mater* **2019**, *31*, 7845-7854.
[102] A. A. Burns, J. Vider, H. Ow, E. Herz, O. Penate-Medina, et al., *Nano Letters* **2009**, *9*, 442-448.
[103] F. Chen, K. Ma, L. Zhang, B. Madajewski, P. Zanzonico, et al., *Chem Mater* **2017**, *29*, 8269-8281.
[104] F. Chen, K. Ma, B. Madajewski, L. Zhuang, L. Zhang, et al., *Nat Commun* **2018**, *9*, 4141.
[105] F. Chen, K. Ma, L. Zhang, B. Madajewski, M. Z. Turker, et al., *ACS Appl Mater Interfaces* **2019**, *11*, 43879-43887.
[106] R. Juthani, B. Madajewski, B. Yoo, L. Zhang, P. M. Chen, et al., *Clin Cancer Res* **2020**, *26*, 147-158.
[107] X. Zhang, F. Chen, M. Z. Turker, K. Ma, P. Zanzonico, et al., *Biomaterials* **2020**, *241*, 119858.
[108] D. Zhang, K.-X. Teng, L. Zhao, L.-Y. Niu, Q.-Z. Yang, *Advanced Materials* **2023**, *35*, 2209789.
[109] S. Hameed, P. Bhattarai, Z. Gong, X. Liang, X. Yue, et al., *Nanoscale Adv* **2022**, *5*, 277-289.
[110] M. Yu, J. Xu, J. Zheng, *Angew Chem Int Ed Engl* **2019**, *58*, 4112-4128.
[111] K. Ma, C. Mendoza, M. Hanson, U. Werner-Zwanziger, J. Zwanziger, et al., *Chemistry of Materials* **2015**, *27*, 4119-4133.

[112] J. Xie, L. Gong, S. Zhu, Y. Yong, Z. Gu, et al., *Adv Mater* **2019**, *31*, e1802244.
[113] S. Goel, F. Chen, E. B. Ehlerding, W. Cai, *Small* **2014**, *10*, 3825-3830.
[114] B. R. Smith, S. S. Gambhir, *Chem Rev* **2017**, *117*, 901-986.
[115] J. Jeon, *Int J Mol Sci* **2019**, *20*.
[116] W. G. Kreyling, A. M. Abdelmonem, Z. Ali, F. Alves, M. Geiser, et al., *Nature Nanotechnology* **2015**, *10*, 619-623.
[117] K. P. Kepp, *Inorg Chem* **2016**, *55*, 9461-9470.
[118] Y. H. Kim, J. Jeon, S. H. Hong, W. K. Rhim, Y. S. Lee, et al., *Small* **2011**, *7*, 2052-2060.
[119] H. W. Kao, Y. Y. Lin, C. C. Chen, K. H. Chi, D. C. Tien, et al., *Bioorg Med Chem Lett* **2013**, *23*, 3180-3185.
[120] N. Su, Y. Dang, G. Liang, G. Liu, *Nanoscale Res Lett* **2015**, *10*, 160.
[121] M. H. Choi, H.-E. Shim, S.-J. Yun, S.-H. Park, D. S. Choi, et al., *ACS Applied Materials & Interfaces* **2016**, *8*, 29227-29231.
[122] T. M. Shaffer, M. A. Wall, S. Harmsen, V. A. Longo, C. M. Drain, et al., *Nano Lett* **2015**, *15*, 864-868.
[123] T. M. Shaffer, S. Harmsen, E. Khwaja, M. F. Kircher, C. M. Drain, et al., *Nano Lett* **2016**, *16*, 5601-5604.
[124] T. Karpov, A. Postovalova, D. Akhmetova, A. R. Muslimov, E. Eletskaya, et al., *Chemistry of Materials* **2022**, *34*, 6593-6605.
[125] P. Wang, W. Sun, Q. Wang, J. Ma, X. Su, et al., *ACS Applied Nano Materials* **2019**, *2*, 1374-1381.
[126] S. B. Lee, S. B. Ahn, S.-W. Lee, S. Y. Jeong, Y. Ghilsuk, et al., *NPG Asia Materials* **2016**, *8*, e281-e281.
[127] S. B. Lee, S. W. Lee, S. Y. Jeong, G. Yoon, S. J. Cho, et al., *ACS Appl Mater Interfaces* **2017**, *9*, 8480-8489.
[128] P. Wu, X. P. Yan, *Chemical Society Reviews* **2013**, *42*, 5489-5521.
[129] C. H. Lu, G. V. Biesold-Mcgee, Y. Liu, Z. Kang, Z. Lin, *Chemical Society Reviews* **2020**, *49*, 4953-5007.
[130] M. Bottrill, L. Kwok, N. J. Long, *Chemical Society Reviews* **2006**, *35*, 557-571.
[131] L. Yang, G. Sundaresan, M. Sun, P. Jose, D. Hoffman, et al., *Journal of Materials Chemistry B* **2013**, *1*, 1421-1431.
[132] C. Blackadar, K. G. Choi, M. F. Embree, H. M. Hennkens, C. Rodriguez-Rodriguez, et al., *ACS Appl Mater Interfaces* **2022**.
[133] Q. K. Ng, C. I. Olariu, M. Yaffee, V. F. Taelman, N. Marincek, et al., *Biomaterials* **2014**, *35*, 7050-7057.
[134] B. Zheng, Q. Wu, Y. Jiang, M. Hou, P. Zhang, et al., *Mater Sci Eng C Mater Biol Appl* **2021**, *128*, 112291.
[135] Y. Jiang, Q. Wu, M. Hou, W. Hai, M. Zhang, et al., *Mater Today Bio* **2023**, *19*, 100578.
[136] X. Sun, X. Huang, X. Yan, Y. Wang, J. Guo, et al., *ACS Nano* **2014**, *8*, 8438-8446.
[137] Y. Zhao, D. Sultan, L. Detering, H. Luehmann, Y. Liu, *Nanoscale* **2014**, *6*, 13501-13509.
[138] Y. Zhao, D. Sultan, L. Detering, S. Cho, G. Sun, et al., *Angew Chem Int Ed Engl* **2014**, *53*, 156-159.
[139] A. F. Frellsen, A. E. Hansen, R. I. Jolck, P. J. Kempen, G. W. Severin, et al., *ACS Nano* **2016**, *10*, 9887-9898.

[140] M. Laprise-Pelletier, J. Lagueux, M. F. Cote, T. LaGrange, M. A. Fortin, *Adv Healthc Mater* **2017**, *6*.
[141] J. Zeng, B. Jia, R. Qiao, C. Wang, L. Jing, et al., *Chem Commun (Camb)* **2014**, *50*, 2170-2172.
[142] E. Boros, A. M. Bowen, L. Josephson, N. Vasdev, J. P. Holland, *Chem Sci* **2015**, *6*, 225-236.
[143] F. Reissig, K. Zarschler, R. Hubner, H. J. Pietzsch, K. Kopka, et al., *ChemistryOpen* **2020**, *9*, 797-805.
[144] A. F. Alvarez-Paneque, B. Rodríguez-González, I. Pastoriza-Santos, L. M. Liz-Marzán, *The Journal of Physical Chemistry C* **2013**, *117*, 2474-2479.
[145] H. Liu, R. M. de Kruijff, A. C. Laan, F. J. Beekman, E. van den Heuvel, et al., *Advanced Therapeutics* **2022**, *5*, 2200077.
[146] D. H. Son, S. M. Hughes, Y. Yin, A. Paul Alivisatos, *Science* **2004**, *306*, 1009-1012.

Core-shell structured gold nanoparticles as carrier for ^{166}Dy/^{166}Ho *in vivo* generator

2

The content of this chapter is adapted from EJNMMI radiopharm. chem. 2022, 7, 16.

Abstract

Background: Radionuclide therapy (RNT) has become a very important treatment modality for cancer nowadays. Comparing with other cancer treatment options, sufficient efficacy could be achieved in RNT with lower toxicity. β^- emitters are frequently used in RNT due to the long tissue penetration depth of the β^- particles. The dysprosium-166/holmium-166 (^{166}Dy/^{166}Ho) *in vivo* generator shows great potential for treating large malignancies due to the long half-life time of the mother nuclide ^{166}Dy and the emission of high energy β^- from the daughter nuclide ^{166}Ho. However, the internal conversion occurring after β^- decay from ^{166}Dy to ^{166}Ho could cause the release of about 72% of ^{166}Ho when ^{166}Dy is bound to conventional chelators. The aim of this study is to develop a nanoparticle based carrier for ^{166}Dy/^{166}Ho *in vivo* generator such that the loss of the daughter nuclide ^{166}Ho induced by internal conversion is prevented. To achieve this goal, we radiolabeled platinum-gold bimetallic nanoparticles (PtAuNPs) and core-shell structured gold nanoparticles (AuNPs) with ^{166}Dy and studied the retention of both ^{166}Dy and ^{166}Ho under various conditions.

Results: The ^{166}Dy was co-reduced with gold and platinum precursor to form the ^{166}DyAu@AuNPs and ^{166}DyPtAuNPs. The ^{166}Dy radiolabeling efficiency was determined to be 60% and 70% for the two types of nanoparticles respectively. The retention of ^{166}Dy and ^{166}Ho were tested in MiliQ water or 2.5 mM DTPA for a period of 72 hours. In both cases, more than 90% of both ^{166}Dy and ^{166}Ho was retained. The results show that the incorporation of ^{166}Dy in AuNPs can prevent the escape of ^{166}Ho released due to internal conversion.

Conclusion: We developed a chelator-free radiolabeling method for ^{166}Dy with good radiolabeling efficiency and very high stability and retention of the daughter nuclide ^{166}Ho. The results from this study indicate that to avoid the loss of the daughter radionuclides by internal conversion, carriers composed of electron-rich materials should be used.

Key words: Radionuclide therapy, Dysprosium-166, Holmium-166, *in vivo* generator, internal conversion, gold nanoparticle

Introduction

Cancer is one of the leading causes of death in the world.[1,2] Nowadays, surgery and external beam radiation therapy (EBRT) are still the most common treatment modalities for localized tumors. In the case of metastases, systemic treatments such as radionuclide therapy (RNT) are preferred. RNT has been proved to be able to significantly prolong the life expectancy of terminal patients without affecting quality of life.[3,4] In RNT, the therapeutic radionuclides are usually linked to chelators conjugated to tumor targeting vectors such as peptides, nucleotides and antibodies. Once distributed to the tumor site, the ionizing radiation emitted by the radionuclides can damage the DNA of the cancer cells and lead to apoptosis.[5–9]

Over the past decades, many radiopharmaceuticals have been developed and some of them have been already applied in the clinic.[10] Radionuclides that emit β^- particles are more commonly applied in the clinic but the interest in α emitters is also growing.[8,11] Since β^- particles have relatively long tissue penetration depth, they are suitable for treating larger metastases.[12,13] Moreover, additional benefits can be achieved with β^- emitters by the so called "cross-fire" effect, i.e. due to the long range of β^- particles, it is not essential to target every single tumor cell to efficiently irradiate the whole tumor.[12]

Holmium-166 (^{166}Ho) is a β^- emitter that decays to ^{166}Er with a half-life time of 26.8 h and emits β^- particles with maximum energy of 1.85 MeV (Figure 2.1 a). The high energy of the β^- particles results in a maximum tissue penetration depth of 8.7 mm which makes ^{166}Ho a promising radionuclide for treating larger malignancies.[14] In addition, ^{166}Ho can also be imaged by single-photon emission computed tomography (SPECT) due to its gamma emission at 80.57 keV.[15] ^{166}Ho is generally produced by the neutron activation of ^{165}Ho following the (n, γ) reaction. An alternative route for ^{166}Ho production is the ^{166}Dy/^{166}Ho generator.[14] Dysprosium-166 (^{166}Dy) has a half-life time of 81.6 h , decays to ^{166}Ho via β^- decay and can be produced by a double neutron capture reaction from ^{164}Dy (Figure 2.1 b). ^{166}Dy/^{166}Ho can also serve as *in vivo* generator which is capable of delivering higher radiation dose per administrated activity due to the three times longer half-life time of ^{166}Dy than ^{166}Ho.[16–18] Therefore, better treatment outcome could be expected by using ^{166}Dy/^{166}Ho *in vivo* generator instead of the direct administration of ^{166}Ho.

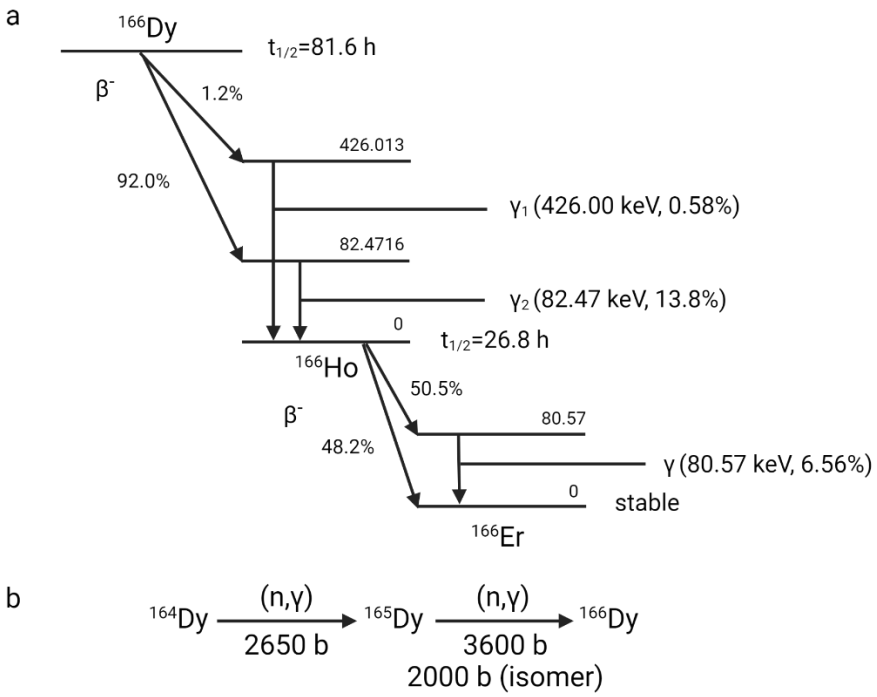

Figure 2.1. a) Decay scheme of ^{166}Dy and ^{166}Ho including the major transitions. b) The double-neutron capture nuclear reaction of ^{164}Dy to produce ^{166}Dy and the corresponding cross-sections.

However, Zeevaart et al. reported the radiolabeling of ^{166}Dy on dodecane tetraacetic acid (DOTA) and surprisingly found that about 72% of the daughter ^{166}Ho was released from the ^{166}Ho-DOTA complex.[19] The ^{166}Ho loss was attributed to the de-excitation of ^{166}Ho* via internal conversion instead of γ emission. Internal conversion is a process where the excited daughter nucleus electromagnetically interacts with inner orbital electrons and results in the emission of an inner electron from K shell or L shell along with the creation of electron vacancies. The electrons from the outer shells will be reorganized to fill in the vacancies while emitting Auger electrons as well as characteristic X-ray. As the result of the emission of Auger electrons, the de-excited ^{166}Ho ions become highly charged and will extract electrons from the surrounding environment (i.e. DOTA). Due to the electron transfer to ^{166}Ho, the DOTA component also becomes positively charged while the ^{166}Ho ion acquires its original oxidation state (+3). The repulsion force between the two components having the same charge results in the rupture of the bonds between ^{166}Ho and DOTA. Thus, ^{166}Ho is

released as free ion. The theoretical calculation predicts 73.6% ^{166}Ho release which matches well with the published experimental results.[19] Being an isotope of a lanthanide element, free ^{166}Ho tends to accumulate in liver, kidney, spleen and bone and may cause severe side effect to the patient.[20] Therefore, to implement the ^{166}Dy/^{166}Ho *in vivo* generator in the clinic, a carrier that can prevent the loss of the internally converted ^{166}Ho has to be developed.

Nowadays, the medical application of different types of nanoparticles has been extensively reported for diagnostics and the treatment of cancer and other diseases.[21–25] Gold nanoparticles (AuNP) have shown great potential as carriers for anti-cancer agents due to their unique properties such as biocompatibility, precisely controlled size and the possibility of easy surface modification.[26,27] Besides using AuNP as carriers for conventional payloads, multiple reports on the chelator-free labelling of medical radionuclides on AuNP have been published.[28,29] In these studies, radionuclides in the form of metallic ions or halogen ions are either co-reduced into the lattice of AuNP (e.g. ^{64}Cu[30–33], ^{111}In[34] and ^{68}Ga[34]) or chemically absorbed on the surface of AuNP (^{125}I, ^{124}I[35,36] and ^{211}At[37]). In most cases, the radiolabeling stability and the tumor uptake of the radionuclides appear to be improved after being loaded on AuNPs when compared to the common chelator approaches.[32] The improved tumor uptake is likely from the prolonged circulation time of AuNPs comparing with small molecules. However, the toxicity of AuNP itself have to be considered even gold is considered to be biocompatible.[38]

In this study, we developed a chelator-free radiolabeling method to incorporate ^{166}Dy in AuNP. In this radiolabeling method, we co-reduced $^{166}Dy^{3+}$ ions with gold and platinum precursors to form either a bimetallic (^{166}DyAuNP) or trimetallic (^{166}DyPtAuNP) nanoparticle. In addition, an extra gold layer was added to the ^{166}DyAuNP to form a core-shell structured ^{166}DyAu@AuNP. We first characterized the physical properties of the DyAu@AuNP and DyPtAuNP with non-radioactive Dy. Then the radiolabeling of ^{166}Dy was performed and the retention of ^{166}Ho on ^{166}DyAu@AuNP and ^{166}DyPtAuNP was evaluated.

Methods and materials:

1. Materials

Gold(III) chloride trihydrate (≥ 99.9%, $HAuCl_4 \cdot 3H_2O$), chloroplatinic acid hexahydrate (≥ 37.50% Pt, $H_2PtCl_6 \cdot 6H_2O$), sodium borohydride (≥ 98.0%, $NaBH_4$), cetyltrimethylammonium bromide (≥ 98%, CTAB), cetyltrimethylammonium chloride solution (25 wt.% in water, CTAC), L-Ascorbic acid (≥ 99%, AA), sodium hydroxide (NaOH) and dysprosium(III) chloride hexahydrate (≥ 99.9%) were purchased from Sigma-Aldrich (Zwijndrecht, the Netherlands). 90% enriched dysprosium-164 oxide powder ($^{164}Dy_2O_3$) was obtained from Oak Ridge National Laboratory (sample number 122502, ORNL, Tennessee, USA). Ethylenediaminetetraacetic acid disodium salt dihydrate ($Na_2EDTA \cdot 2H_2O$), Diethylenetriamine pentaacetate (DTPA), hydrochloric acid (HCl, 30%, Suprapur®) and nitric acid (HNO_3, 69%, Supelco®) was supplied by Merck. All chemicals were used as received without further purification. MiliQ water was obtained from an in-house MiliQ system (Millipore) and used throughout this study.

2. Production of ^{166}Dy

^{166}Dy was produced by the double neutron capture reaction of ^{164}Dy. 3 mg 90% enriched $^{164}Dy_2O_3$ powder was irradiated in the reactor facilities of the SCK•CEN - BR2 Reactor (Mol, Belgium), the Institute of Energy Security and Environmental Safety Centre for Energy Research (Budapest, Hungary) or the nuclear reactor research facility (HOR, Hoger Onderwijs Reactor) at the Department of Radiation Science and Technology of the Delft University of Technology (Delft, the Netherlands). The obtained $^{166}Dy_2O_3$ powder was dissolved in 5 ml 1 M HCl under mild heating to prepare a stock solution of $^{166}DyCl_3$. 2.5 ml of the stock solution was transferred to a 20-ml glass vial and the pH of the stock solution was adjusted to ~5.5 by adding 2.35 ml of 1 M NaOH solution (checked by pH test paper). The activity of ^{166}Dy and ^{166}Ho in the stock solution was measured on a calibrated well-type HPGe detector (Canberra).

3. Synthesis of AuNP seed

The synthesis was adapted from a published protocol with some changes[39] and is schematically illustrated in Figure 2.2. The AuNP seeds were synthesized by the reduction of $HAuCl_4$ by $NaBH_4$ using CTAB as capping agent. 0.1 ml 25 mM $HAuCl_4$, 4 ml 250 mM

CTAB and 5.9 ml MiliQ water was added to a glass vial and mixed for 10 min. 0.6 ml freshly prepared, ice-cold 10 mM $NaBH_4$ solution was added to the mixture dropwise under vigorous stirring. The color of the solution changed from yellow to dark brown rapidly. The obtained AuNP seeds were left undisturbed at 27 ℃ for 1.5 h before further usage.

4. Growth of AuNP seed to 5 nm AuNP

2 ml 200 mM CTAC, 1.5 ml 100 mM AA and 1 ml AuNP seed dispersion were added to a glass vial and mixed for 5 min at 27 ℃. 2 ml 0.5 mM $HAuCl_4$ was then added in one-shot by a pipet. The reaction was continued at 27 ℃ for another 15 min.

5. Synthesis of 5 nm non-radioactive DyAu@AuNP

33 µl, 20 µl or 10 µl 25 mM $DyCl_3$ solution (pH 5.5) was mixed with 0.1 ml 25 mM $HAuCl_4$ and 4 ml 250 mM CTAB in a glass vial to achieve the Dy:Au (n:n) feeding ratio of 1:3, 1:5 or 1:10. The total volume was adjusted to 10 ml by MiliQ water. 0.6 ml ice-cold 10 mM $NaBH_4$ solution was then added to the mixture dropwisely under vigorous stirring. The growth of the DyAuNP seed to 5 nm core-shell structured DyAu@AuNP was performed in the same way as the growth of AuNP seed to 5 nm AuNP after aging the DyAuNP seed at 27 ℃ for 1.5 h.

6. Synthesis of non-radioactive DyPtAuNP

10 µl 25 mM H_2PtCl_6, 90 µl 25 mM $HAuCl_4$ and 4 ml 250 mM CTAB were mixed in a glass vial. 33 µl or 10 µl 25 mM $DyCl_3$ solution (pH 5.5) was then added to achieve the Dy:(Pt+Au) (n/n) feeding ration of 1:3 or 1:10. MiliQ water was added to adjust the total volume to be 10 ml and stirred for 10 min. 0.6 ml freshly prepared, ice-cold 10 mM $NaBH_4$ solution was added to the mixture dropwise under vigorous stirring. The colour of the solution changed from yellow to dark brown rapidly. The obtained DyPtAuNP was left undisturbed at 27 ℃ for 1.5 h before purification.

7. Synthesis of 5 nm ^{166}DyAu@AuNP

88.2 µl stock solution of $^{166}DyCl_3$ containing approximately 0.134 MBq ^{166}Dy and 0.2 MBq ^{166}Ho was mixed with 0.1 ml 25 mM $HAuCl_4$ and 4 ml 250 mM CTAB in a glass vial. 30.1 µl, 17.1 µl or 7.1 µl of 25 mM $DyCl_3$ solution (pH 5.5) was then added to ensure the Dy:Au (n:n) feeding ratio to be 1:3, 1:5 or 1:10. The synthesis of ^{166}DyAuNP seed and growth to

^{166}DyAu@AuNP was performed in the same way as non-radioactive DyAu@AuNP which was described above.

8. Synthesis of ^{166}DyPtAuNP

88.2 µl stock solution of $^{166}DyCl_3$ containing approximately 0.134 MBq ^{166}Dy and 0.2 MBq ^{166}Ho was mixed with 10 µl 25 mM H_2PtCl_6, 90 µl 25 mM $HAuCl_4$ and 4 ml 250 mM CTAB in a glass vial. 30.1 µl or 7.1 µl of 25 mM $DyCl_3$ solution (pH 5.5) was then added to ensure Dy:Au (n:n) feeding ratio of 1:3 or 1:10. The final volume was then adjusted to 10 ml by MiliQ water and stirred for 10 min. 0.6 ml freshly prepared, ice-cold 10 mM $NaBH_4$ solution was added to the mixture dropwise under vigorous stirring. The obtained ^{166}DyPtAuNP was left undisturbed at 27 ℃ for 1.5 h before purification.

9. Characterization of non-radioactive nanoparticles

The morphology and size of the AuNP, DyAu@AuNP and DyAuNP was determined with a JEM-1400 Plus transmission electron microscope (TEM, JEOL) at the acceleration voltage of 120 kV. The UV−vis absorption spectra of AuNPs were measured by a UV-VIS-NIR spectrophotometer (UV-6300PC, VWR). The hydrodynamic radius of the samples was determined by dynamic light scattering (DLS) which consisted of a JDS uniphase 633 nm 35 mW laser source, an ALV sp 125 s/w 93 goniometer, a fibre detector and a Perkin Elmer photo counter. The data was fitted using the CONTIN method and the Stokes-Einstein equation (Equation 1) was used to determine the hydrodynamic radius of the nanoparticles.

$$R_H = \frac{kT}{6\pi\eta D} \qquad (1)$$

10. Determination of ^{166}Dy radiolabeling efficiency

100 µl 100 mM EDTA or 100 mM DTPA was added to the ^{166}DyAu@AuNP and ^{166}DyPtAuNP samples and incubated at 27 ℃ for 30 min to bind with free $^{166}Dy^{3+}$ ions. Then the samples were centrifuged (4000 rpm, 10 min) and washed three times using spin filters (MWCO 10 KDa, Amicon). The final volume of the washed samples was adjusted to 4 ml by MiliQ water and stored at 37 ℃. The counts of the nanoparticles and filtrates (^{166}Dy-EDTA) of all samples were measured by an automatic gamma counter (Wallac Wizard^2 2480, Perkin Elmer) or a low energy Ge-detector (GL2020R, Canberra). ^{166}Dy was measured using

its gamma emission at 425.99 keV. The radiolabeling efficiency of ^{166}Dy was calculated by the following formula: Counts(NPs)/[Counts(NPs)+ ∑Counts(filtrate)] × 100%.

11. Determination of ^{166}Ho and ^{166}Dy retention

To assess the stability of ^{166}Ho and ^{166}Dy on nanoparticles, the samples were dispersed in 4 ml MiliQ water or 2.5 mM DTPA (pH 7.5) and incubated at 37 ℃ for 24, 48 and 72 h. At each time point, the samples were collected and washed by MiliQ water using spin filters under centrifugation (4000 rpm, 10 min). The counts of the nanoparticles and the filtrate was measured to calculate the retention of both ^{166}Ho and ^{166}Dy.

12. Determination of gold and dysprosium content in ^{166}DyAu@AuNP and ^{166}DyPtAuNP

1 ml of each completely decayed sample was completely destructed in 1 ml aqua regia (HCl/HNO_3=3:1) and diluted by MiliQ water to a final volume of 10 ml. The concentration of Au and Dy were then measured by ICP-OES (Optima 8000, Perkin Elmer).

Results and discussion

1. Synthesis and characterization of non-radioactive DyAu@AuNP

In this study, we designed a core-shell structured AuNP to function as the carrier for ^{166}Dy /^{166}Ho *in vivo* generator. The gold precursor was first co-reduced with $^{166}Dy^{3+}$ ions to form the ^{166}DyAuNPs. Subsequently, an extra gold shell was grown by reducing gold precursor with ascorbic acid to prevent the possible escape of free $^{166}Ho^{3+}$ ions. Besides assisting to retain free $^{166}Ho^{3+}$ ions, the growth of an extra gold layer can also improve the colloidal stability of the DyAuNPs.[39] It is important that the original physiochemical properties of the AuNPs are not altered upon ^{166}Dy encapsulation. Thus, we first performed a pilot study with non-radioactive $DyCl_3$ to explore the influence of Dy content on the physical properties of the DyAu@AuNPs. The non-radioactive $DyCl_3$ was co-reduced with $HAuCl_4$ by a strong reducing agent $NaBH_4$ to form the bimetallic DyAuNPs. Three samples with different Dy:Au feeding ratios of 1:3, 1:5 and 1:10 were prepared. An extra gold shell was then grown on the seed particles via the reduction of $HAuCl_4$ at lower concentration using ascorbic acid and resulting in the core-shell structured DyAu@AuNPs. The non-incorporated Dy^{3+} ions were removed by incubating DyAu@AuNPs with EDTA or DTPA, followed by multiple cycles

of washing with MiliQ water. Au@AuNP without Dy content was also prepared with the same method and used as the control group.

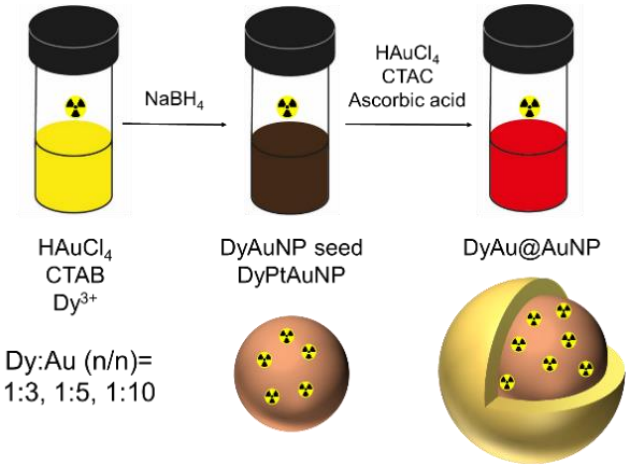

Figure 2.2. Schematic illustration of the synthesis of ^{166}DyAu@AuNP and ^{166}DyPtAuNP.

The size and shape of the DyAu@AuNPs were characterized by transmission electron microscope (TEM). As shown in Figure 2.3 a-d, DyAu@AuNPs with varying Dy:Au feeding ratios as well as the Au@AuNP all showed a diameter of 4.9 nm. The hydrodynamic radius (R_H) of the DyAu@AuNPs and Au@AuNP was measured by dynamic light scattering (DLS). As shown in Figure 2.3 e, the intensity weighted R_H was determined to be within the range of 12~14 nm for both the DyAu@AuNPs and the Au@AuNP. The hydrodynamic radius of the DyAu@AuNPs was found to be larger than the radius measured by TEM, since DLS measures the hydration layer formed around CTAB/CTAC on the surface of the nanoparticles. Due to the surface plasmon resonance (SPR) effect of AuNPs, the characteristic UV-vis spectrum can be used as an indication of the size of AuNPs.[40] The UV-vis spectrum of the DyAu@AuNPs and Au@AuNP is shown in Figure 2.3 f. The wavelength of the SPR peak (λ_{SPR}) of all samples were detected near 520 nm, indicating that the DyAu@AuNPs all had comparable size to the Au@AuNP. All results of the characterization of the DyAu@AuNPs and Au@AuNP are summarized in Table 2.1.

Table 2.1. Summary of the physical properties of DyAu@AuNPs with different Dy:Au feeding ratios.

	No Dy	1:3	1:5	1:10
d (nm)	4.9 ± 0.8	4.9 ± 0.6	4.9 ± 0.7	4.9 ± 0.7
R_H (nm)	12.3 ± 0.3	12.9 ± 0.3	14.1 ± 0.5	11.8 ± 0.3
λ_{SPR} (nm)	518	522	519	520

Based on the TEM, UV-vis and DLS measurements, we conclude that incorporating different amounts of Dy into the gold nanoparticle had no influence on the final size and shape of the core-shell structured DyAu@AuNPs.

2. Synthesis and characterization of non-radioactive DyPtAuNP

To better understand the behavior of ^{166}Ho and ^{166}Dy on nanoparticles and check if internally converted ^{166}Ho can be retained even without the extra gold layer, we attempted to directly use the DyAuNPs as the carrier for ^{166}Dy. However, the DyAuNPs were not stable and aggregated to larger AuNPs within 24 h (Figure S2.3). To improve the colloidal stability of DyAuNPs, we hereby prepared trimetallic DyPtAuNPs by replacing 10% of Au with Pt while the Dy:(Au+Pt) feeding ratios was still set to be 1:3 and 1:10. PtAuNP with no Dy content was also prepared and used as control. The size of the DyPtAuNPs as determined by TEM are shown in Figure 2.4 a-c. The diameter of the DyPtAuNP with Dy feeding ratio of 1:3 was measured to be 4.4 ± 1.1 nm which is comparable to the PtAuNP (4.0 ± 1.3 nm). However, larger particles (d=6.6 ± 1.8 nm) were measured for the DyPtAuNP with Dy feeding ratio of 1:10. The UV-vis spectrum of the DyPtAuNPs and PtAuNP is given in Figure 2.4 d. The absence of SPR peak near 500 nm further confirmed the small size of the nanoparticles.[41]

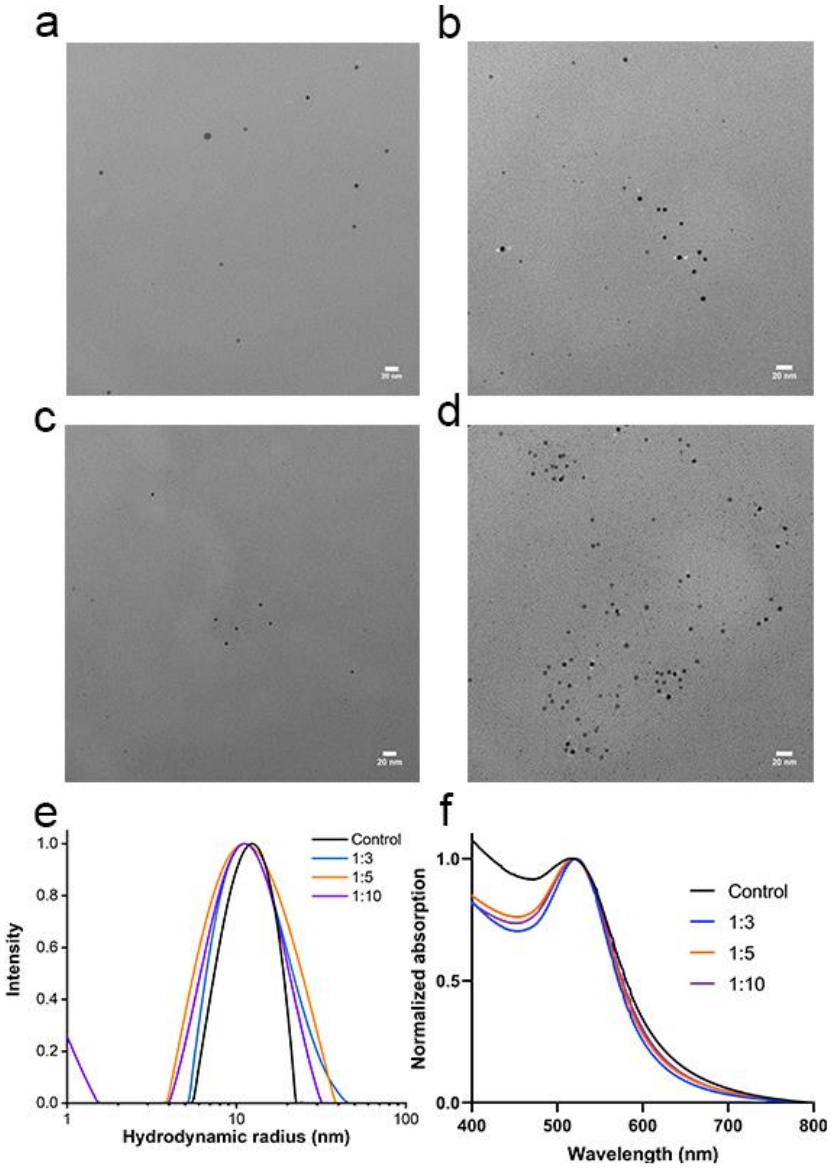

Figure 2.3. Characterization of DyAu@AuNPs. a-d) Representative TEM image of samples with different Dy:Au feeding ratios: Dy:Au=1:3 (a), 1:5 (b), 1:10 (c), no Dy addition (d). Scale bar is 20 nm. See supporting information for size distribution histograms **(Figure S2.1**). e) Hydrodynamic radius (R_H) of the samples measured by DLS. f) UV-vis spectrum of the DyAu@AuNPs.

3. Radiolabeling of ^{166}Dy on DyAu@AuNP and DyPtAuNP

The radiolabeling of ^{166}Dy was carried out by a similar method as used for the preparation of non-radioactive DyAu@AuNPs and DyPtAuNPs. The Dy source was changed to a mixture

of non-radioactive $DyCl_3$ and $^{166}DyCl_3$ stock solution containing 0.134 MBq ^{166}Dy. Due to the decay of ^{166}Dy, ^{166}Ho was also present in the stock solution of $^{166}DyCl_3$. Considering the trace amount of $^{166}Ho^{3+}$ ions, we expect that this to have negligible influence on the formation of the NPs. Three independent samples of ^{166}DyAu@AuNP and ^{166}DyPtAuNP with different Dy:Au feeding ratios were prepared and washed thoroughly by EDTA/DTPA and MiliQ water to remove all unbounded ^{166}Dy. The ^{166}Dy radiolabeling efficiency was calculated by comparing the counts of nanoparticles and the washing solution at 425.99 keV. The calculated results are shown in Figure 2.5. Radiolabeling efficiency of 60% and 70% was achieved for ^{166}DyAu@AuNPs and ^{166}DyPtAuNPs respectively. No significant difference of the radiolabeling efficiency was found among the groups with different Dy:Au feeding ratios.

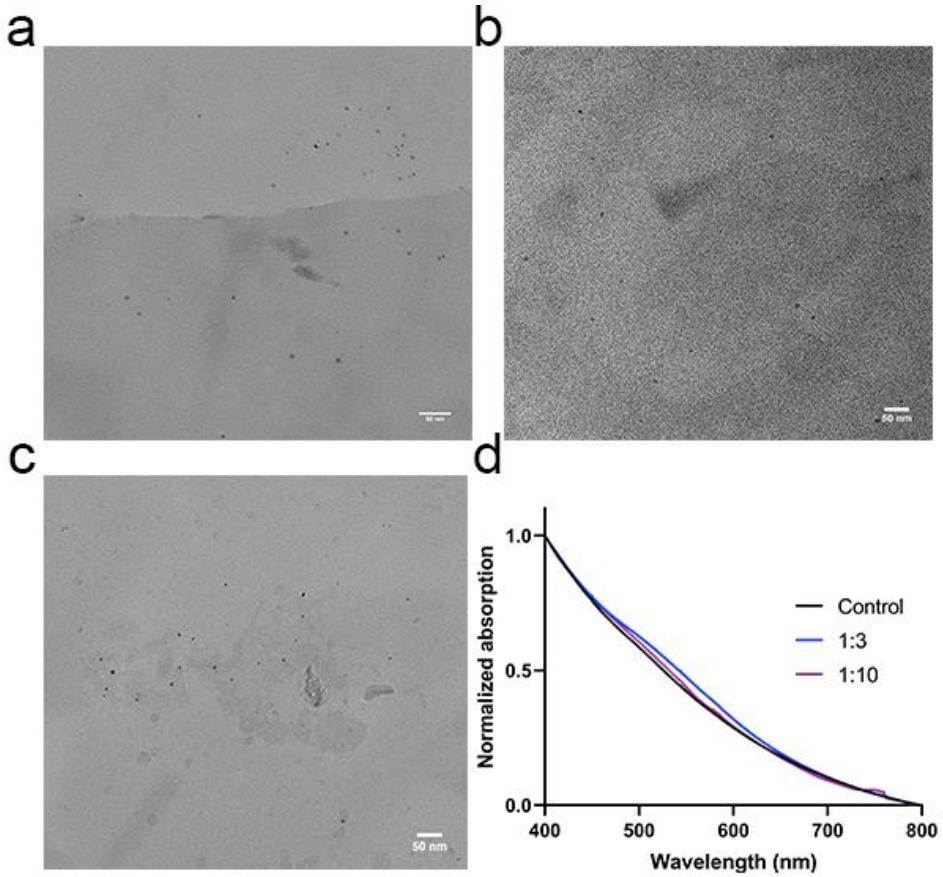

Figure 2.4. Characterization of DyPtAuNPs. a-c) Representative TEM image of samples with different Dy:Au feeding ratios: Dy:Au=1:3 (a), 1:10 (b) and no Dy addition(c). Scale bar is 50 nm. See supporting information for size distribution histograms (**Figure S2.2**). d) UV-vis spectrum of the DyPtAuNPs.

Due to the big lattice mismatch (11.9%) and the large difference of reduction potential between Dy (III, -2.29 V) and Au (III, $[AuCl_4]^-$, +0.93 V), not all initially added Dy was reduced in the AuNP core which resulted in ^{166}Dy radiolabeling efficiency of around 60%. As the same activity of $^{166}DyCl_3$ was used during the synthesis of ^{166}DyAu@AuNPs and ^{166}DyPtAuNPs, the activity of radiolabeled ^{166}Dy was the same for all samples with different Dy:Au feeding ratios. No improvement of the ^{166}Dy radiolabeling efficiency was achieved by lowering the initial amount of Dy^{3+}.

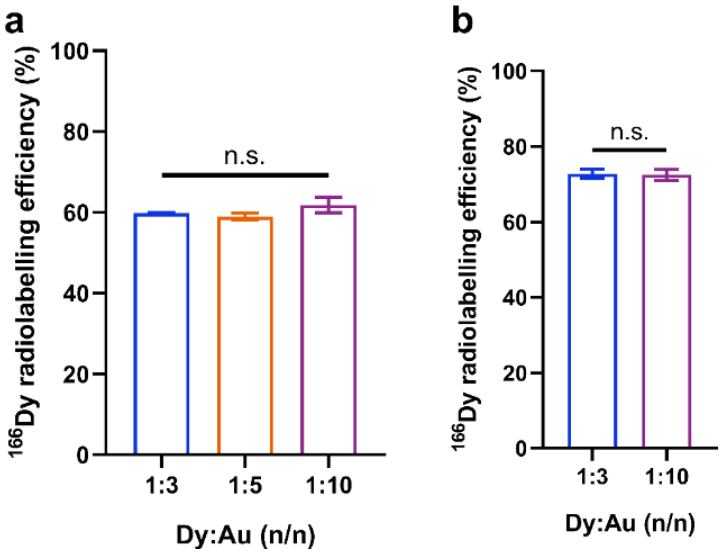

Figure 2.5. ^{166}Dy radiolabeling efficiency of ^{166}DyAu@AuNP (a) and ^{166}DyPtAuNP (b) with different Dy:Au feeding ratios. The error bars represent the standard deviations of three independent experiments (n.s. indicates non-significant difference, 2way ANOVA test)

The completely decayed ^{166}DyAu@AuNP and ^{166}DyPtAuNP samples were also destructed and further analyzed by ICP-OES to measure the concentration of Au and Dy. Comparing with the Au concentration of the Au@AuNP and PtAuNP samples, little difference of the Au concentration was found from the ^{166}DyAu@AuNP and ^{166}DyPtAuNP samples (**Table S2.1**). Taking ICP-OES measurements together with other characterizations, we further confirmed that the reduction of gold precursor by $NaBH_4$ as well as the formation of nanoparticles was not affected by the addition of Dy^{3+}. The ^{166}Dy radiolabeling efficiency was also calculated using the total concentration of Dy (including both radioactive and non-radioactive Dy) measured by ICP-OES (Figure S2.4). Similar to the results from Ge-detector

measurement, the radiolabeling efficiency was not influenced by the Dy:Au feeding ratios. However, we found that the ^{166}Dy radiolabeling efficiency calculated from ICP-OES data was approximately 10% lower than that from the Ge-detector data. Further studies will be carried out to explain this phenomenon.

In vivo generator of therapeutic radionuclides can generally increase the delivered dose per administrated activity because of the longer half-life time of the mother nuclides.[18] To make sure the radiation dose is mainly delivered to the tumor while sparing the normal tissues, both the mother and the daughter nuclides should be kept within the carrier. Therefore, we radiolabeled core-shell structured gold nanoparticles, i.e. the ^{166}DyAu@AuNPs with ^{166}Dy. An outer layer of gold was added to prevent the diffusion of free ^{166}Ho if it escapes from the core nanoparticle. On the other hand, nanoparticles without the shell structure, i.e. the ^{166}DyPtAuNPs were also radiolabeled with ^{166}Dy for comparison. ^{166}DyAuNP seeds were not studied because of the low colloidal stability (Figure S2.3).

To measure the retention of the internally converted ^{166}Ho as well as the retention of ^{166}Dy, ^{166}DyAu@AuNPs and ^{166}DyPtAuNPs were incubated in MiliQ water or 2.5 mM DTPA (pH 7.5) at 37 °C for 72 h. Every 24 hour, the samples were centrifuged to separate NPs from free $^{166}Dy^{3+}$ and $^{166}Ho^{3+}$. The counts of the nanoparticles and the washing solution was measured at 65~90 keV and 340~460 keV for ^{166}Ho and ^{166}Dy respectively. As the NPs were still capped by CTAB/CTAC, the nanoparticles would form aggregation upon interaction with high concentration salt solution or protein.[42] Thus, the *in vitro* stability tests were not performed in PBS or serum to avoid the interference of nanoparticle aggregation. As shown in Figure 2.6, more than 95% of ^{166}Ho was found to be retained in both ^{166}DyAu@AuNPs and ^{166}DyPtAuNPs for at least 72 h in MiliQ water (Figure 2.6 a, b). The retention of ^{166}Dy was also found to be more than 95% for both ^{166}DyAu@AuNPs and ^{166}DyPtAuNPs during the 72 h incubation in MiliQ water (Figure 2.6 c, d). For all the samples challenged by DTPA, about 90% of both ^{166}Ho and ^{166}Dy was still bounded to the nanoparticles even after 72 h incubation (Figure 2.7). These results indicate that very high ^{166}Ho and ^{166}Dy retention was achieved independent from the Dy:Au feeding ratio and the extra shell of coating.

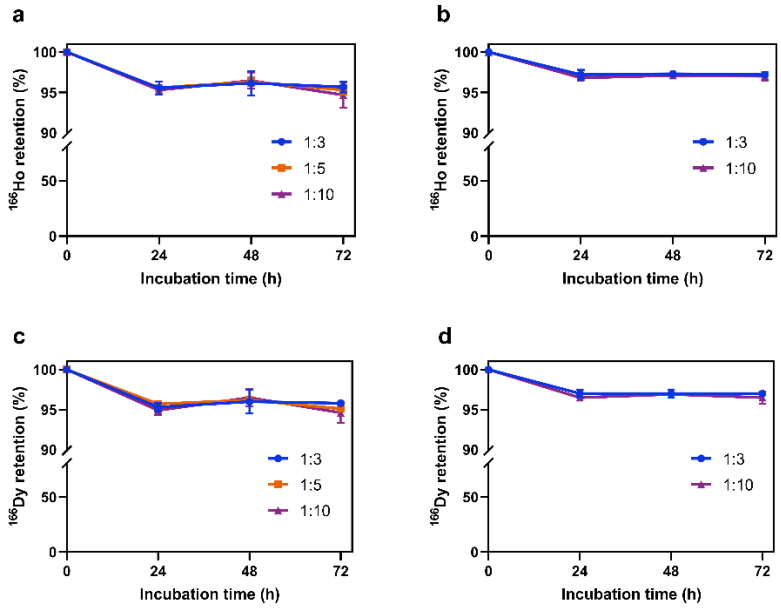

Figure 2.6. ^{166}Ho and ^{166}Dy retention of ^{166}DyAu@AuNPs (a, c) and ^{166}DyPtAuNPs (b, d) with different Dy:Au feeding ratios in MiliQ water at 37 °C as function of time. The error bars represent the standard deviation of three independent experiments.

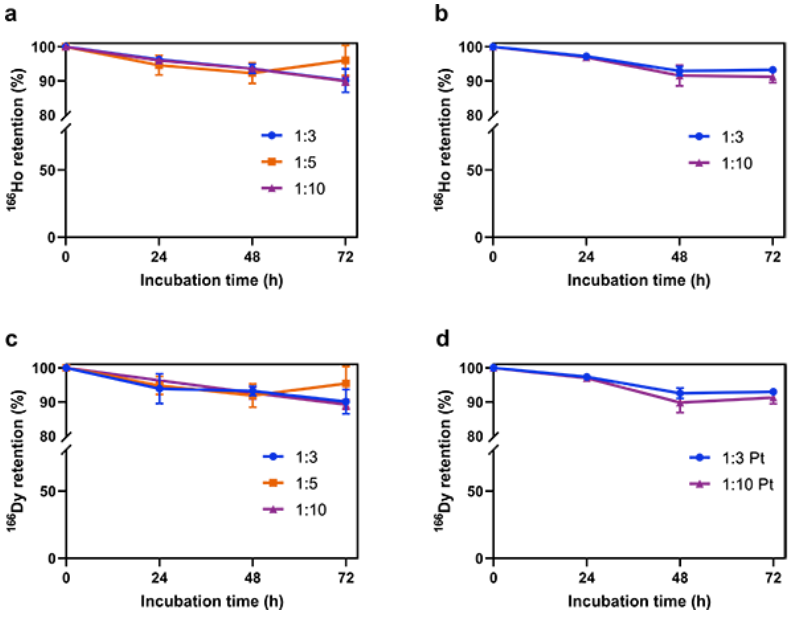

Figure 2.7. ^{166}Ho and ^{166}Dy retention of ^{166}DyAu@AuNPs (a, c) and ^{166}DyPtAuNPs (b, d) with different Dy:Au feeding ratios in 2.5 mM DTPA at 37 °C as function of time. The error bars represent the standard deviation of three independent experiments.

Surprisingly, the ^{166}DyPtAuNPs were found to be able to retain the same percentage of ^{166}Ho as the ^{166}DyAu@AuNPs. This result suggests that high ^{166}Ho retention could still be achieved even without the addition of an extra gold layer. This finding made us think about the possible mechanism responsible for the high ^{166}Ho retention on AuNPs. The internal conversion of ^{166}Dy results in highly charged ^{166}Ho ions which tend to seek electrons from the surrounding environment, i.e. the carrier. In the case of ^{166}Dy coupled to a simple chelator composed of low Z elements such as dodecane tetraacetic acid (DOTA), the number of free electrons in the system is low. Therefore, DOTA molecule could be easily altered to be positively charged after the electron migration to the ^{166}Ho ions. Due to the repulsion between the entities having the same charge, i.e. $^{166}Ho^{3+}$ and $[DOTA]^{n+}$, the ^{166}Ho-DOTA complex is ruptured. When a high Z material is used as the carrier for ^{166}Dy, such as AuNP, many more free electrons are available. When the highly positive ^{166}Ho ion extracts electrons from its neighboring Au atoms, electrons can be quickly redistributed to fill in the new vacancies. The redistribution of electrons might cause a transient change of the surface charge of AuNP, but then electrons from the solvent (i.e. water) will be attracted to the AuNP due to the ultra-high affinity of Au to solvated electrons.[43] Therefore, the colloidal stability of AuNP is preserved while the release of ^{166}Ho is avoided. A similar method was reported to improve the retention of ^{80}Br which was internally converted from ^{80m}Br (49 and 37 keV, α=1.6 and 300 respectively) by Adamson et al.[44,45] The authors found that 100% and 86% of ^{80}Br was released from $[Co(NH_3)_5Br]^{2+}$ (aq) and solidified $[Co(NH_3)_5Br](NO_3)_2$ (s) while 47% and even 0% of ^{80}Br was released from $[PtBr_6]^{2-}$ (aq) and solidified $(NH_4)_2PtBr_6$ (s). This result supported our hypothesis on the function of AuNP as electron source for the internally converted ^{166}Ho. Besides, the results from these studies also suggest that in our case the reduction of $^{166}Dy^{3+}$ into solid state (Dy^0) might also contribute to the high retention of ^{166}Ho.

Besides the high retention of the internally converted ^{166}Ho, our radiolabeling method is also simple and quick. The whole procedure can be finished within 8 hours without the need of separating ^{166}Dy from ^{166}Ho. The interaction between the β^- particle emitted by ^{166}Ho and gold atoms is also favorable for a more efficient dose delivery due to the formation of secondary electrons and free radicals such as ·OH radicals.[46] To make the ^{166}DyPtAuNPs and ^{166}DyAu@AuNPs more applicable for clinical application, the current capping ligand, CTAB/CTAC, has to be exchanged with biocompatible ligands such as PEG. In previous

studies it has been shown that small AuNPs not conjugated with targeting agents have tumor uptake around 4-5% ID/g depending on the morphology and surface properties of the nanoparticles.[31,47] In comparison, small molecules such as PSMA can achieve much higher tumor uptake.[48] Therefore, it will be very interesting to determine whether the addition of such targeting moieties will increase tumor accumulation.

Conclusions

In summary, we developed a chelator-free radiolabeling method to obtain a ^{166}Dy/^{166}Ho *in vivo* generator and prevented the loss of ^{166}Ho that is caused by internal conversion. The explanation for the high ^{166}Ho retention was not experimentally proven but might be related to the high electron density of the gold nanoparticles. To further understand the mechanism of ^{166}Ho retention on gold nanoparticles, the structure of the nanoparticles should be studied by both experiments as well as theoretical simulations. Besides the further research on ^{166}Ho retention mechanism, the capping ligands of the nanoparticles should be replaced to increase the biocompatibility of the nanoparticles and make them suitable for medical applications.

References

[1] H. Sung, J. Ferlay, R. L. Siegel, M. Laversanne, I. Soerjomataram, A. Jemal, F. Bray, *CA. Cancer J. Clin.* **2021**, *71*, 209–249.
[2] F. Bray, J. Ferlay, I. Soerjomataram, R. L. Siegel, L. A. Torre, A. Jemal, *CA. Cancer J. Clin.* **2018**, *68*, 394–424.
[3] S. E. Pool, E. P. Krenning, G. A. Koning, C. H. J. van Eijck, J. J. M. Teunissen, B. Kam, R. Valkema, D. J. Kwekkeboom, M. de Jong, *Semin. Nucl. Med.* **2010**, *40*, 209–218.
[4] J. L. Humm, O. Sartor, C. Parker, O. S. Bruland, R. Macklis, *Int. J. Radiat. Oncol. Biol. Phys.* **2015**, *91*, 898–906.
[5] S. V Gudkov, N. Y. Shilyagina, V. A. Vodeneev, A. V Zvyagin, *Int. J. Mol. Sci.* **2016**, *17*.
[6] A. Dash, F. F Russ Knapp, M. Ra Pillai, *Curr. Radiopharm.* **2013**, *6*, 152–180.
[7] G. Sgouros, L. Bodei, M. R. McDevitt, J. R. Nedrow, *Nat. Rev. Drug Discov.* **2020**, *19*, 589–608.
[8] N. K. Tafreshi, M. L. Doligalski, C. J. Tichacek, D. N. Pandya, M. M. Budzevich, G. El-Haddad, N. I. Khushalani, E. G. Moros, M. L. McLaughlin, T. J. Wadas, *Molecules* **2019**, *24*, 4314.
[9] T. I. Kostelnik, C. Orvig, *Chem. Rev.* **2019**, *119*, 902–956.
[10] S. K. Suman, S. Subramanian, A. Mukherjee, *Nucl. Med. Biol.* **2021**, *98–99*, 40–58.
[11] B. J. B. Nelson, J. D. Andersson, F. Wuest, *Pharmaceutics* **2021**, *13*, 1–28.
[12] J.-P. Pouget, I. Navarro-Teulon, M. Bardiès, N. Chouin, G. Cartron, A. Pèlegrin, D. Azria, *Nat. Rev. Clin. Oncol.* **2011**, *8*, 720–734.
[13] L. Marcu, E. Bezak, B. J. Allen, *Crit. Rev. Oncol. Hematol.* **2018**, *123*, 7–20.
[14] N. J. M. Klaassen, M. J. Arntz, A. Gil Arranja, J. Roosen, J. F. W. Nijsen, *EJNMMI Radiopharm. Chem.* **2019**, *4*, 1–26.
[15] M. Elschot, J. F. W. Nijsen, A. J. Dam, H. W. A. M. de Jong, *PLoS One* **2011**, *6*, e26174.
[16] S. Poty, L. C. Francesconi, M. R. McDevitt, M. J. Morris, J. S. Lewis, *J Nucl Med* **2018**, *59*, 1020–1027.
[17] K. E. Baidoo, D. E. Milenic, M. W. Brechbiel, *Nucl. Med. Biol.* **2013**, *40*, 592–599.
[18] P. Edem, J. Fonslet, A. Kjaer, M. Herth, G. Severin, *Bioinorg. Chem. Appl.* **2016**, *2016*, 1–8.
[19] J. R. Zeevaart, Z. Szücs, S. Takács, N. V. Jarvis, D. Jansen, *Radiochim. Acta* **2012**, *100*, 109–113.
[20] Y. S. Suzuki, Y. Momose, N. Higashi, A. Shigematsu, K.-B. Park, Y. M. Kim, J. R. Kim, J. M. Ryu, *J. Nucl. Med.* **1998**, *39*, 2161 LP – 2166.
[21] M. J. Mitchell, M. M. Billingsley, R. M. Haley, M. E. Wechsler, N. A. Peppas, R. Langer, *Nat. Rev. Drug Discov.* **2021**, *20*, 101–124.
[22] B. Pelaz, C. Alexiou, R. A. Alvarez-Puebla, et al, *ACS Nano* **2017**, *11*, 2313–2381.
[23] O. S. Thomas, W. Weber, *Front. Bioeng. Biotechnol.* **2019**, *7*, DOI 10.3389/fbioe.2019.00415.
[24] J. Shi, P. W. Kantoff, R. Wooster, O. C. Farokhzad, *Nat. Rev. Cancer* **2017**, *17*, 20–37.
[25] X. Y. Wong, A. Sena-Torralba, R. Álvarez-Diduk, K. Muthoosamy, A. Merkoçi, *ACS Nano* **2020**, *14*, 2585–2627.
[26] P. Singh, S. Pandit, V. R. S. S. Mokkapati, A. Garg, V. Ravikumar, I. Mijakovic, *Int. J. Mol. Sci.* **2018**, *19*, DOI 10.3390/ijms19071979.
[27] E. Boisselier, D. Astruc, *Chem. Soc. Rev.* **2009**, *38*, 1759–1782.

[28] J. Ge, Q. Zhang, J. Zeng, Z. Gu, M. Gao, *Biomaterials* **2020**, *228*, DOI 10.1016/j.biomaterials.2019.119553.
[29] F. Silva, M. P. C. Campello, A. Paulo, *Materials (Basel).* **2021**, *14*, 1–32.
[30] A. F. Frellsen, A. E. Hansen, R. I. Jølck, P. J. Kempen, G. W. Severin, P. H. Rasmussen, A. Kjær, A. T. I. Jensen, T. L. Andresen, *ACS Nano* **2016**, *10*, 9887–9898.
[31] X. Sun, X. Huang, X. Yan, Y. Wang, J. Guo, O. Jacobson, D. Liu, L. P. Szajek, W. Zhu, G. Niu, D. O. Kiesewetter, S. Sun, X. Chen, *ACS Nano* **2014**, *8*, 8438–8446.
[32] M. Pretze, N. P. van der Meulen, C. Wängler, R. Schibli, B. Wängler, *J. Label. Compd. Radiopharm.* **2019**, *62*, 471–482.
[33] Y. Zhao, D. Sultan, L. Detering, H. Luehmann, Y. Liu, *Nanoscale* **2014**, *6*, 13501–13509.
[34] B. Zheng, Q. Wu, Y. Jiang, M. Hou, P. Zhang, M. Liu, L. Zhang, B. Li, C. Zhang, *Mater. Sci. Eng. C* **2021**, *128*, 112291.
[35] S. B. Lee, S. B. Ahn, S.-W. Lee, S. Y. Jeong, Y. Ghilsuk, B.-C. Ahn, E.-M. Kim, H.-J. Jeong, J. Lee, D.-K. Lim, Y. H. Jeon, *NPG Asia Mater.* **2016**, *8*, e281–e281.
[36] S. B. Lee, S. W. Lee, S. Y. Jeong, G. Yoon, S. J. Cho, S. K. Kim, I. K. Lee, B. C. Ahn, J. Lee, Y. H. Jeon, *ACS Appl. Mater. Interfaces* **2017**, *9*, 8480–8489.
[37] L. Dziawer, P. Koźmiński, S. Męczyńska-Wielgosz, M. Pruszyński, M. Łyczko, B. Wąs, G. Celichowski, J. Grobelny, J. Jastrzębski, A. Bilewicz, *RSC Adv.* **2017**, *7*, 41024–41032.
[38] S. Ranjbar Bahadori, A. Mulgaonkar, R. Hart, C.-Y. Wu, D. Zhang, A. Pillai, Y. Hao, X. Sun, *WIREs Nanomedicine and Nanobiotechnology* **2021**, *13*, e1671.
[39] Y. Zheng, X. Zhong, Z. Li, Y. Xia, *Part. Part. Syst. Charact.* **2014**, *31*, 266–273.
[40] S. Barbosa, A. Agrawal, L. Rodríguez-Lorenzo, I. Pastoriza-Santos, R. A. Alvarez-Puebla, A. Kornowski, H. Weller, L. M. Liz-Marzán, *Langmuir* **2010**, *26*, 14943–14950.
[41] C. Alric, I. Miladi, D. Kryza, J. Taleb, F. Lux, R. Bazzi, C. Billotey, M. Janier, P. Perriat, S. Roux, O. Tillement, *Nanoscale* **2013**, *5*, 5930–5939.
[42] Z. Zhang, M. Lin, *RSC Adv.* **2014**, *4*, 17760–17767.
[43] K. Ghandi, A. D. Findlater, Z. Mahimwalla, C. S. MacNeil, E. Awoonor-Williams, F. Zahariev, M. S. Gordon, *Nanoscale* **2015**, *7*, 11545–11551.
[44] A. W. Adamson, J. M. Grunland, *J. Am. Chem. Soc.* **1951**, *73*, 5508.
[45] S. Wexler, G. R. Anderson, *J. Chem. Phys.* **1960**, *33*, 850–863.
[46] K. Haume, S. Rosa, S. Grellet, M. A. Śmiałek, K. T. Butterworth, A. V Solov'yov, K. M. Prise, J. Golding, N. J. Mason, *Cancer Nanotechnol.* **2016**, *7*, 8.
[47] X. Zhang, L. Detering, D. Sultan, G. S. Heo, H. Luehmann, S. Taylor, A. Choksi, J. B. Rubin, Y. Liu, *ACS Appl. Bio Mater.* **2022**, *5*, 235–242.
[48] S. R. Banerjee, M. Pullambhatla, C. A. Foss, S. Nimmagadda, R. Ferdani, C. J. Anderson, R. C. Mease, M. G. Pomper, *J. Med. Chem.* **2014**, *57*, 2657–2669.

Supplemental information

Theoretical calculation of ^{166}Ho loss due to internal conversion

The possibility of internal conversion and emission of gamma rays can be described by a factor called internal conversion coefficient (α).

$$\alpha = \frac{number\ of\ de-excitations\ by\ the\ release\ of\ conversion\ electrons}{number\ of\ de-excitations\ via\ gamma\ ray\ emission}$$

In the case of ^{166}Dy, its emission at 82.5 keV has an overall internal conversion coefficient of 4.02 which indicates that about 80% of this transition is by internal conversion.

$$Probability\ of\ internal\ conversion = \frac{\alpha}{1+\alpha}$$

Taking the branching ratio of this transition line (92.5%) into account, the probability of internal conversion of the β^- decay of ^{166}Dy can be calculated by 80% × 92.5%=73.6%.

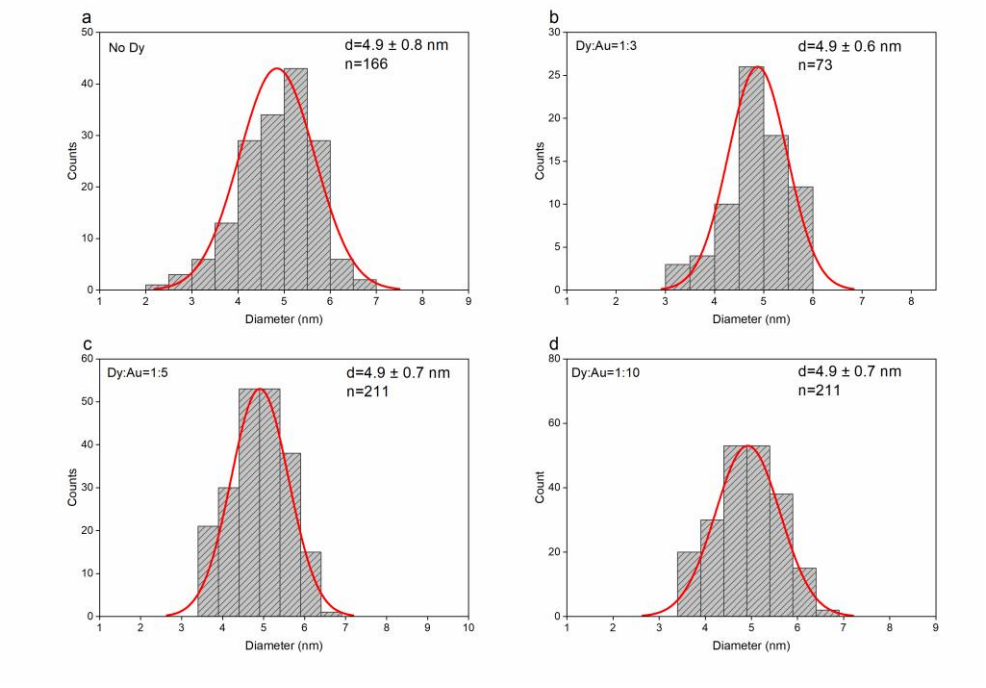

Figure S2.1. Size distribution histogram of DyAu@AuNPs with different Dy:Au feeding ratios: No addition of Dy (a), Dy:Au=1:3 (b), 1:5 (c) and 1:10 (d).

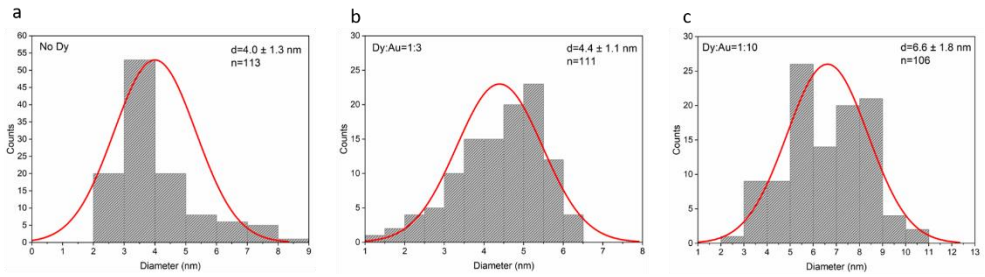

Figure S2.2. Size distribution histogram of DyPtAuNPs with different Dy:Au feeding ratios: No addition of Dy (a), Dy:Au=1:3 (b) and 1:10 (c).

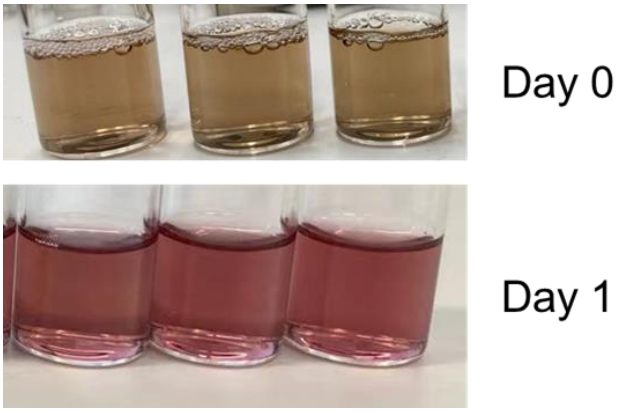

Figure S2.3. Representative picture of ^{166}DyAuNP (Dy:Au=1:3) after 24 h incubation at 37 °C. The color change from dark brown to purple red is an indication of change of the nanoparticle size. To avoid the interference of the nanoparticle size change on the ^{166}Ho retention and ^{166}Dy radiostability, the ^{166}DyAuNPs were not further studied in this work.

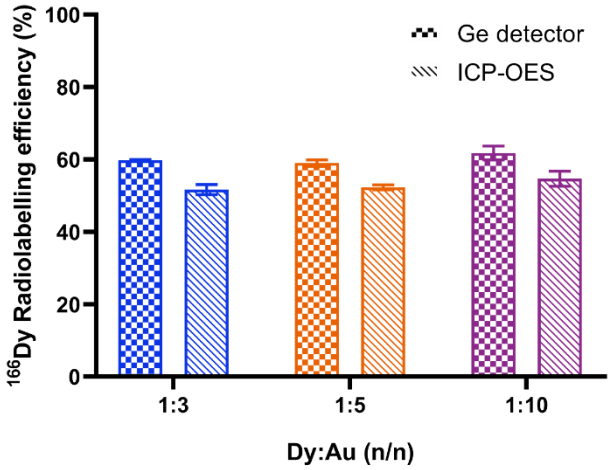

Figure S2.4. Comparison of ^{166}Dy radiolabeling efficiency calculated from Ge-detector data (dot) or ICP-OES (line) data. The ICP-OES data based ^{166}Dy radiolabeling efficiency was found to be about 10% lower than that calculated using Ge-detector data.

Table S2.1. Comparison of Au concentration among Au@AuNP, ^{166}DyAu@AuNP, PtAuNP and ^{166}DyPtAuNP. The Au concentration was measured by ICP-OES after the complete decay of ^{166}Dy.

	Dy:Au feeding ratio	[Au] mg/L*
Au@AuNP	-	109.7
^{166}DyAu@AuNP	1:3	115.1
^{166}DyAu@AuNP	1:5	109.7
^{166}DyAu@AuNP	1:10	110.1
PtAuNP	-	93.9
^{166}DyPtAuNP	1:3	89.5
^{166}DyPtAuNP	1:10	91.5

*The [Au] concentration for core-shell structured NPs and PtAuNPs are all based on a final volume of 4 ml after washing.

Ultra-small gold nanoparticles radiolabeled with Iodine-125 as potential new radiopharmaceutical

3

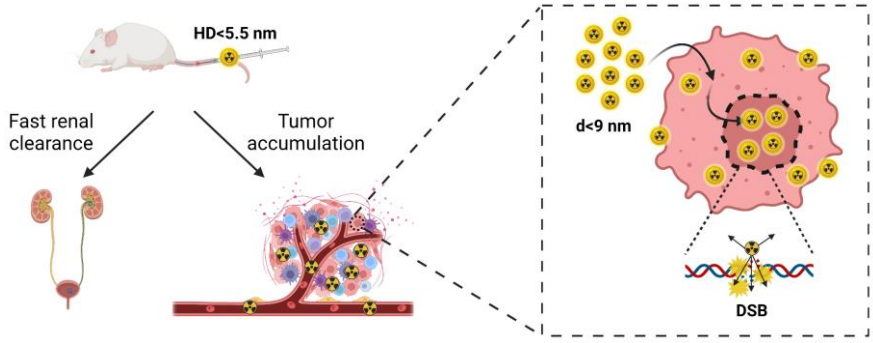

The content of this chapter is adapted from ACS Appl. Bio Mater. 2024, 7, 1240−1249.

Abstract

The relatively high linear energy transfer of Auger electrons, which can cause clustered DNA damage and hence efficient cell death, makes Auger emitters excellent candidates for attacking metastasized tumors. Moreover, gammas or positrons are usually emitted along with the Auger electrons, providing the possibility of theragnostic applications. Despite the promising properties of Auger electrons, only a few radiopharmaceuticals employing Auger emitters have been developed so far. This is most likely explained by the short ranges of these electrons requiring the delivery of the Auger emitters to crucial cell parts such as the cell nucleus. In this work, we combined the Auger emitter ^{125}I and ultra-small gold nanoparticles to prepare a novel radiopharmaceutical. The ^{125}I labeled gold nanoparticles were shown to accumulate at the cell nucleus, leading to high tumor killing efficiency in both 2D and 3D tumor cell models. The results from this work indicate that ultra-small nanoparticles, which passively accumulate at the cell nucleus, have the potential to be applied in targeted radionuclide therapy. Even better tumor killing efficiency can be expected if tumor targeting moieties are conjugated to the nanoparticles.

Key words: radionuclide therapy, Auger therapy, Auger electron, iodine-125, ultrasmall gold nanoparticle

Introduction

Radionuclide therapy (RNT) is a cancer treatment modality that uses internal radiation to primarily attack cancer metastases. Targeting agents such as antibodies and peptides are typically coupled via bifunctional chelators to radionuclides emitting α particles, β^- particles or Auger electrons (AE).[1] The emitted particles can damage DNA molecules of cancer cells either directly or indirectly, eventually leading to the death of the tumor cells.[2] Numerous pre-clinical and clinical trials have been carried out to verify the clinical potential of α and β^- emitters based radiopharmaceuticals in the past years.[3-7] However, studies on applying AE emitters for cancer treatment are still limited.

AEs are commonly emitted by radionuclides that decay by electron capture (EC) or internal conversion (IC). The AEs have energy from 10 eV to 10 keV but with a very short range of only a few nanometers, resulting in intermediate linear energy transfer (LET) from 4 to 26 keV/µm. Due to the short range of AEs, they must be emitted close enough to the DNA strands to produce dense ionizations and excitations.[8] Thus, the AE emitters must be targeted to the cell nucleus or other crucial cell organelles to achieve optimal tumor killing efficiency.[9] High nucleus uptake of AE emitters has been previously achieved by radiolabeling AE emitters on nucleosides or tumor targeting peptides containing nuclear localization sequence (NLS).[10-14]

Besides nucleosides and antibodies, nanoparticles have also been found to accumulate at the cell nucleus actively or passively.[15-16] As reported previously, spherical nanoparticles with a size of 9 nm or less are able to cross the nuclear pore complex by diffusion.[17] For larger nanoparticles, surface modification by peptides with NLS is always required to achieve high accumulation at the cell nucleus.[18-19] For instance, 10 to 30 nm gold nanoparticles (AuNP) modified with epidermal growth factor (EGF) or trastuzumab have been radiolabeled with ^{111}In and have shown high tumor killing efficiency due to the enhanced localization at the cell nucleus.[20-22] However, the high liver and spleen uptake of these large nanoparticles due to the mononuclear phagocyte system (MPS) capture limits their tumor uptake and might lead to radiation burden to the liver and spleen.[23]

Iodine-125 (^{125}I) is a typical AE emitter having 23.0 AEs emitted per decay and a half-life of 59.4 days, which is widely used therapeutically in the brachytherapy for brain tumors,

prostate cancer as well as head and neck cancer.[24-30] Besides brachytherapy, other clinical application of ^{125}I in RNT is very rare and the results rather disappointing. In early studies, primarily nucleoside 5-iodo-2-deoxyuridine (^{125}I-UdR) has been used which showed only tiny tumor accumulation due to metabolic breakdown of the ^{125}I-UdR. These findings have led to direct tumor injection of the radiopharmaceutical rather than systemic treatment, which, unfortunately, does not help in attacking metastasized cancer.[31-33] Preclinically, a number of studies do show that ^{125}I has good therapeutic potential provided that sufficient tumor accumulation is achieved.[34-37] Instead of using small organic molecules to carry ^{125}I that are prone to metabolic breakdown, we suggest applying ultra-small gold nanoparticles as the carrier for ^{125}I. Such nano-particles radiolabeled with ^{125}I have already been reported in positron emission tomography (PET) imaging studies, showing the fast tumor targeting and high radiochemical stability *in vivo*.[38-39] However, few studies on the therapeutic effect of ^{125}I radiolabeled nanoparticles have been reported so far.[40]

In this work, we investigated the potential of polyethylene-glycol (PEG) coated AuNPs with a size of just 2 nm, radiolabeled with ^{125}I through a simple and fast method achieving high radiolabeling efficiency and high radiochemical stability. The uptake, sub-cellular distribution and tumor killing efficiency of the ^{125}I-PEG-AuNPs were studied *in vitro* using 2D monolayer or 3D tumor spheroid cell models revealing high tumor killing efficiency.

Methods and materials

1. Materials

Gold(III) chloride trihydrate ($\geq$ 99.9%, $HAuCl_4 \cdot 3H_2O$) and crystal violet (1% solution) were purchased from Merck Sigma (Zwijndrecht, the Netherlands). PEG-SH (Mw=750 Da) was obtained from Rapp Polymere (Tuebingen, Germany). Iodine-125 (17 mCi/mg, pH 12~14, ^{125}I) was supplied by Perkin Elmer. All chemicals were used as received without further purification. MiliQ water was obtained from an in-house MiliQ system (Millipore) and used throughout this study.

2. Synthesis of 2 nm PEG-AuNPs

The synthesis of PEG-AuNPs was adapted from a published method with minor adjustments.[41] In a typical synthesis, 25 ml 2.4 mM PEG750-SH water solution was mixed with 75 µl 1 M $HAuCl_4$ at room temperature for 30 min. The mixture was then heated at 95 ℃ for 35 min under vigorous stirring. The resulting PEG-AuNPs were collected and filtered by a 220 nm syringe filter to remove the large aggregates, followed by thrice water wash using centrifuge filters (Amicon®, MWCO 10,000) to remove free small ligands. The final volume was adjusted to 2 ml after an extra wash by PBS buffer (pH 7.4) and stored at 4 ℃.

3. Characterization of PEG-AuNPs

The shape and size of the PEG-AuNPs were imaged by a 120 kV JEM-1400 Plus transmission electron microscope (TEM, JEOL). The size distribution of the nanoparticles was studied by measuring the size of at least 150 particles in each sample. The absorption spectrum of PEG-AuNPs was measured by a UV-VIS-NIR spectrophotometer (UV-6300PC, VWR). The hydrodynamic diameter and zeta-potential of the PEG-AuNPs were determined by a zeta sizer (nano-ZS, Malvern). To determine the concentration of gold content in each sample, 10 µl of a sample was first dissolved in 100 µl aqua regia and then measured using ICP-OES (Optima 8000, Perkin Elmer).

4. Radiolabeling of ^{125}I on PEG-AuNPs

The ^{125}I stock solution was neutralized by the same volume of 0.1 M HCl right before being added to the PEG-AuNPs. In typical sample preparation, 37 MBq ^{125}I was added to 100 µl 46 µM PEG-AuNPs (^{125}I:NP=0.1) and shaken at 600 rpm for 30 min at 37 ℃. The radiolabeling efficiency was monitored by iTLC (mobile phase: acetonitrile:water=1:3). The ^{125}I-PEG-AuNPs remained at the origin while the free ^{125}I was located at the top of the strip. The iTLC strips were dried in air and then exposed to a phosphor screen for 15 min. The phosphor screen was scanned using a Typhoon Trio phosphor imager (GE Healthcare). The obtained images were analyzed using ImageQuant TL software (GE Healthcare) to calculate the radiolabeling efficiency.

5. *In vitro* colloidal stability

The PEG-AuNPs were dispersed in PBS and 10% fetal bovine serum (FBS) in PBS and incubated at 37 ℃ for 72 h. The UV-vis spectrum of each PEG-AuNP dispersion was

measured every 24 h. Besides, the hydrodynamic diameter of PEG-AuNPs in PBS and MiliQ water was also measured every 24 h.

6. *In vitro* radiochemical stability

The ^{125}I-PEG-AuNPs were incubated in PBS and 10% FBS in PBS at 37 ℃ for 72 h. The release of ^{125}I from PEG-AuNPs was evaluated by iTLC every 24 h using the same mobile phase as described in section 3.

7. Cell Culture

The U87 human glioblastoma cells were obtained from ATCC and cultured in complete Dulbecco's modified Eagle's medium (DMEM) supplemented with 10% FBS and 1% penicillin/streptomycin in a cell incubator (Heracell®, Heraeus) providing a humidified atmosphere containing 5% CO_2 at 37 ℃.

8. *In vitro* cell viability assay

U87 cells were plated on 96-well plates with a cell density of 5000 cells/well. After pre-incubation for 24 h, the culture medium was replaced by fresh culture medium containing 1 nM to 1000 nM PEG-AuNPs and incubated for another 24 h. The cells unexposed to PEG-AuNPs were used as control. The cells were then washed twice with PBS and fed with fresh culture medium containing 10% Cell Counting Kit-8 (CCK-8, Dojindo Laboratories). The absorbance of the cells at 450 nm was measured by a microplate scanning spectrophotometer (PowerWave XS™, Bio-Tek) after incubating the cells at 37 ℃ for another 1 to 2 hours. The relative viability of each group was then calculated by comparing the Absorption at 450 nm with that of the control group.

9. Uptake and sub-cellular distribution of ^{125}I-PEG-AuNPs in monolayer cells

Total uptake: U87 cells were plated on 12-well plates and pre-incubated for 24 h (8×10^4 cells/well). On the next day, 1 ml fresh culture medium containing 10, 50, 100 nM ^{125}I-PEG-AuNPs (37 kBq) was added to the cells. The cells were then incubated for another 4 h or 24 h at 37 ℃. After incubation, the cells were washed three times with PBS to remove free PEG-AuNPs and completely lysed with 0.1 M NaOH. The wash fractions and the lysed cell fractions were finally counted in an automated gamma counter (Wallac Wizard^2 2480, Perkin Elmer).

Sub-cellular distribution: To determine the sub-cellular distribution of ^{125}I-PEG-AuNPs in monolayer cells, the cells were thoroughly washed after being incubated with different concentrations of ^{125}I-PEG-AuNPs for 4 or 24 h and then detached by trypsin. The sub-cellular fractions of cells were separated using the Subcellular Protein Fractionation Kit (Thermo Scientific) following the instructions of the manufacturer. The counts of each cell fraction were measured by an automated gamma counter (Wallac Wizard^2 2480, Perkin Elmer).

Silver staining: U87 cells were seeded on 6-well plates with the cell density of 8×10^4 cells/well and preincubated for 24 h. On the next day, the cells were treated by 1, 50 and 100 nM PEG-AuNPs for another 24 h followed by thrice PBS wash. Silver staining of the cells was performed using the LI silver enhancers kit (Nanoprobe) following the instructions from the manufacturer. The stained cells were imaged using an inverted light microscope (AE2000, Motic).

10. Uptake of ^{125}I-PEG-AuNPs in cell spheroids

U87 cells were seeded on U-shaped 96 well plates and pre-incubated for 7 days (2000 cells/well) to form the spheroids. After the formation of spheroids, 200 µl culture medium containing 10, 50 or 100 nM ^{125}I-PEG-AuNPs (37 kBq) was added to the spheroids and incubated for 4 or 24 h at 37 ℃. The spheroids were then washed three times by PBS before measuring the counts of the wash and the spheroid fractions using an automated gamma counter (Wallac Wizard^2 2480, Perkin Elmer).

11. *In vitro* cytotoxicity of ^{125}I-PEG-AuNPs in monolayer cells

Viability assay: U87 cells were seeded on 96-well plate with the cell density of 5000 cells/well and pre-incubated at 37 ℃ for 24 hours. After pre-incubation, the culture medium was removed and 100 µl fresh culture medium containing ^{125}I-PEG-AuNPs with 37, 370 or 740 kBq of ^{125}I was added and incubated at 37 ℃ for 24 h. The cells exposed to culture medium and cells exposed to 740 kBq [^{125}I]NaI were used as control. On the next day, the cells were washed three times by PBS, fed with 100 µl fresh culture medium and incubated at 37 ℃ for another 24 hours before the cell viability of each group was measured by the CCK-8 assay. (n=4)

DNA proliferation assay: After the CCK-8 assay, the cells were washed twice by PBS and 200 µl water was added to each well. The cells were hereby repetitively frozen (-20 ℃) and thawed (37 ℃) for membrane destruction. Then the DNA content of each well was measured using the AccuClear dsDNA quantification kit (Biotum) following the instructions from the manufacturer. In brief, 50 µl of each sample was added to 200 µl working solution prepared by diluting the dye 100 times with the DNA quantification buffer and mixed by pipetting. After incubating at room temperature for 5 min at dark, the plate was read on a fluorescent spectrometer with excitation and emission settings of 468 nm and 507 nm respectively. The obtained results were fitted to a DNA standard curve to determine the mass of DNA per sample and normalized to the control group to determine the proliferation capacity. (n=4)

Colony formation assay: U87 cells were seeded on 12-well plates with a cell density of 8×10^4 cells/well and pre-incubated at 37 ℃ for 24 hours. Then the cells were incubated with ^{125}I-PEG-AuNPs containing 0.37, 0.74, 1 or 3.7 MBq ^{125}I or 3.7 MBq [^{125}I]NaI for another 24 h. The cells exposed to culture medium were used as control. The next day, the cells were washed three times by PBS to remove free activity and reseeded in 6-well plates with a cell density of 500 cells/well. The cells were then left undisturbed for 14 days to allow colony formation. The culture medium was refreshed every 3 days. On the last day, the colonies were fixed by 4% (w/v) paraformaldehyde, stained by 1% crystal violet and counted manually on an inverted light microscope (Gapelcom, n=3).

12. *In vitro* cytotoxicity of ^{125}I-PEG-AuNPs in 3D cell spheroids

Spheroid growth inhibition assay: U87 cells were seeded in U-shaped 96-well plate at the cell density of 2000 cells/well and incubated for 7 days to form spheroids. After the formation of spheroids, the culture medium containing ^{125}I-PEG-AuNPs (37, 370 and 740 kBq ^{125}I) or 740 kBq [^{125}I]NaI was added and incubated at 37 ℃. After being incubated for 24 h, the spheroids were washed three times by PBS and fed with fresh medium. The growth of the spheroids was followed in time up to 13 days by capturing images using an inverted light microscope (Gapelcom). The size of the spheroids was analyzed with ImageJ. Non-treated spheroids were used as a control. (n=4)

13. Statistical analysis

Data are expressed as mean ± standard deviation based on at least three independent replicates. Student's t-test was used for the comparison between two samples. For the comparison among multiple samples, one-way or two-way ANOVA test was performed. P values: ns $p>0.05$, $^{*}p\leq0.05$, $^{**}p\leq0.01$, $^{***}p\leq0.001$, $^{****}p\leq0.0001$.

Results and Discussion

The application of nanomaterials in cancer treatment and diagnosis has been extensively reported.[42-43] However, the high off-target uptake of nanoparticles in liver and spleen has raised the concern of long-term toxicity to healthy tissues.[23] Nanoparticles with a hydrodynamic diameter less than 5.5 nm appear to be able to escape the MPS capture and to be rapidly excreted via the urinary system.[44-45] In addition, such small nanoparticles have been found to pass through the nuclear pore complex (NPC) and accumulate in the cell nucleus.[46-47] In this chapter, we combined 2 nm sized nanoparticles with ^{125}I to develop a potential AE radiopharmaceutical.

The ultra-small PEG-AuNPs were first synthesized by the thermal reduction of $HAuCl_4$ in the presence of PEG750-SH (Figure 3.1 a).[41] The core size of the PEG-AuNPs was determined by TEM imaging and appeared to be 1.9 ± 0.3 nm (Figure 3.1 b). The small size of the PEG-AuNPs was further proved by the recorded UV-vis spectrum where no obvious peak around 500 nm was observed (Figure 3.1 c). As shown in Figure 3.1 d, the hydrodynamic diameter of the PEG-AuNPs was measured by dynamic light scattering (DLS) and appeared to be 4.3 ± 0.8 nm. Furthermore, the PEG-AuNPs had neutral zeta-potential which can be ascribed to the PEG coating (Figure 3.1 e).

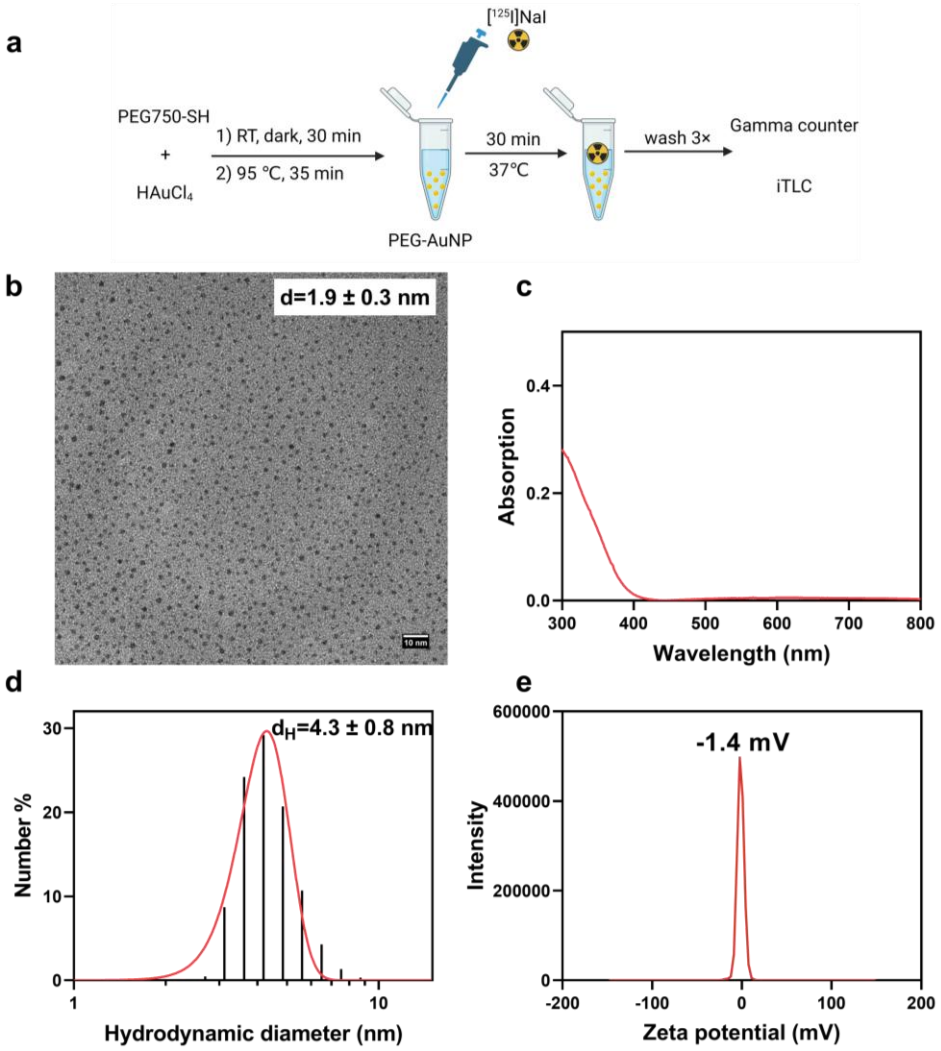

Figure 3.1. Synthesis and characterization of PEG-AuNPs: a) Schematic illustration of the synthesis and radiolabeling of PEG-AuNPs with ^{125}I; b) TEM image; c) UV-vis spectrum; d) number weighted hydrodynamic diameter and e) zeta-potential of PEG-AuNPs dispersed in PBS. Scale bar=10 nm.

Considering the complex environment in blood, the intravenously injected nanoparticles must maintain colloidal stability under similar conditions such as when dispersed in physiological solutions. The obtained PEG-AuNPs were therefore dispersed in PBS or 10% FBS in PBS and incubated at 37 °C for 72 h. As shown in Figure 3.2 a, the hydrodynamic diameter of the PEG-AuNPs in PBS was measured every 24 h and found to be unchanged for at least 72 h. Furthermore, no pronounced change in the UV-vis spectrum of PEG-AuNPs in

PBS (Figure S3.1) and 10% FBS (Figure 3.2 b) was detected during the 72 hours incubation, indicating the high colloidal stability of PEG-AuNPs even in the presence of serum proteins.

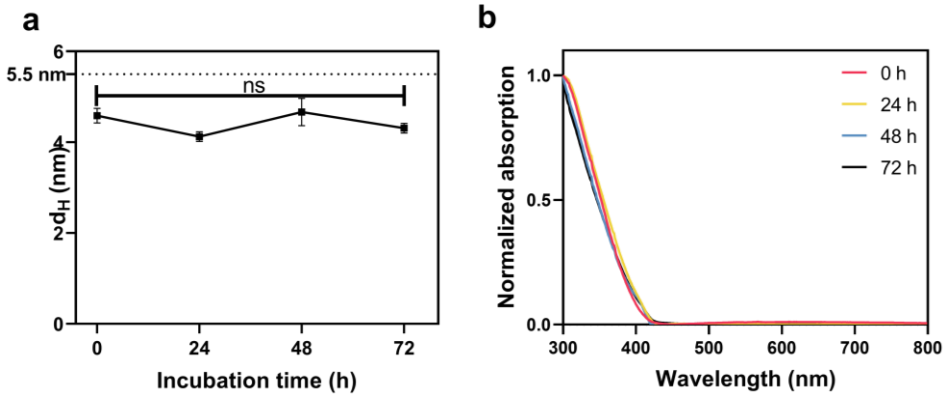

Figure 3.2. Colloidal stability of PEG-AuNPs: a) the number weighted hydrodynamic diameter of PEG-AuNPs in PBS at 37 °C as a function of time, n=3; b) Normalized UV-vis spectrum of PEG-AuNPs in 10% FBS at 37 °C and at different time points.

After confirming the small size and high colloidal stability of the PEG-AuNPs, the radiolabeling with ^{125}I was performed. As a soft base and acid respectively, I^- ions have strong affinity to Au^0.[48] Thus, the radiolabeling of the PEG-AuNPs with ^{125}I was utilized by chemisorption of ^{125}I on the surface of the particles. The radiolabeling conditions were optimized by using various molar ratios of the PEG-AuNPs and $^{125}I^-$ ions and the pH values of the [^{125}I]NaI solution. It was found that neutralizing the [^{125}I]NaI solution to pH 7 using 0.1 M HCl before adding it to the PEG-AuNPs could significantly increase the radiolabeling efficiency, i. e. from ~65% to more than 90% (Figure S3.2). We then studied the influence of the ^{125}I to NP ratio. As shown in Figure 3.3a and Figure S3.3, higher radiolabeling efficiency could be achieved by lowering the ^{125}I to NP ratio. The radiolabeling efficiency was determined to be ~100%, 92.5% and 36% by iTLC when there was 2500×, 10× and 2.5× excess of PEG-AuNPs, i. e. ^{125}I:NP=0.0004, 0.1 and 0.4 respectively. Increasing the number of PEG-AuNPs could boost the reaction between $^{125}I^-$ and PEG-AuNPs by providing larger surface area for reaction, thereby leading to higher radiolabeling efficiency. A ratio of ^{125}I:NP of 0.1 was chosen for all following experiments in order to ensure high enough specific activity. After removing non-bound ^{125}I with centrifuge filters, the ^{125}I-PEG-AuNPs and washing solutions were counted using an automated gamma counter for the determination of radiolabeling efficiency. A slightly lower radiolabeling efficiency of 85.7% was calculated based on these measurements versus iTLC, probably because of the removal of loosely bound

^{125}I from the PEG-AuNPs (Figure 3.3 a).

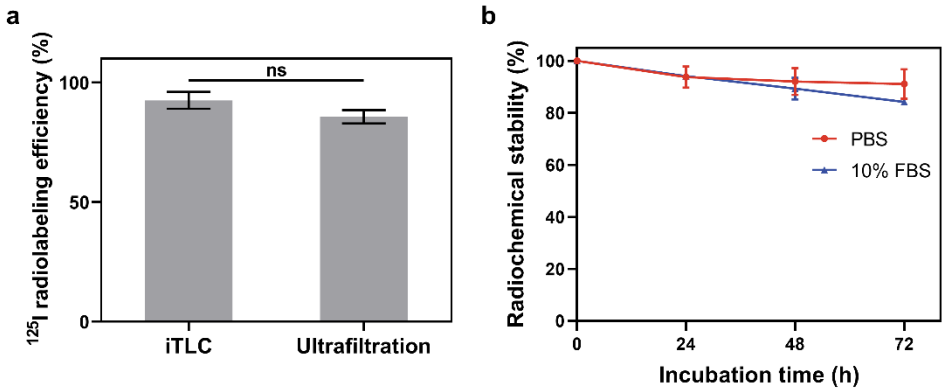

Figure 3.3. a) Radiolabeling efficiency of ^{125}I-PEG-AuNPs determined by iTLC and ultrafiltration experiments. ^{125}I:NP=0.1, [^{125}I]NaI was neutralized before usage, n=3; b) radiochemical stability of ^{125}I-PEG-AuNPs in PBS or 10% FBS over 72 h at 37 °C, n=3.

As free I^- could naturally accumulate in the thyroid, the high radiochemical stability of the ^{125}I-PEG-AuNPs is critical for further *in vivo* applications.[49] As shown in Figure 3.3 b, more than 90% of the ^{125}I was found to remain on the PEG-AuNPs for at least 72 h in PBS. In the case of the ^{125}I-PEG-AuNP challenged by serum, more than 85% of ^{125}I was still found to be retained on the nanoparticles after 72 h of incubation. The results of the *in vitro* stability assays indicate that the ^{125}I-PEG-AuNPs possess sufficient radiochemical stability and are suitable for biological applications. RCS of the ^{125}I-PEG-AuNPs can most likely be further improved by pre-oxidizing [^{125}I]NaI before adding it to the PEG-AuNPs or by using charged coating agents instead of PEG.[50]

To check the biocompatibility of the PEG-AuNPs, U87 cells were incubated with bare PEG-AuNPs for 24 h with concentrations ranging from 1 nM to 1 μM. The viability of the cells was then determined by CCK-8 assay. As shown in Figure 3.4 a, no significant difference on the cell viability was observed between the PEG-AuNPs treated groups and the control group, clearly indicating that the PEG-AuNPs are non-toxic to U87 cells even at a concentration as high as 1 μM.

The uptake of the PEG-AuNPs was then investigated in U87 cell monolayers. The uptake of bare PEG-AuNPs was first studied by silver staining (Figure S3.4). It can be seen from the silver staining images that the PEG-AuNPs was either internalized into U87 cells or it was

attached to the cell membrane. Next, ^{125}I-PEG-AuNPs having 37 kBq ^{125}I were mixed with non-radioactive PEG-AuNPs to achieve a final NP concentration of 10, 50 and 100 nM. The U87 cells were then incubated with the PEG-AuNPs for 4 or 24 h at 37 °C. The cell uptake of the PEG-AuNPs was found to be dependent on the concentration of the nanoparticles and the incubation time as shown in Figure 3.4 b. By extending the incubation time from 4 h to 24 h, the number of internalized nanoparticles increased by nearly 10 times for all tested concentrations. Furthermore, increasing the concentration of PEG-AuNPs from 10 nM to 100 nM resulted in an approximately 10 times higher uptake at 24 h. The highest cell uptake was achieved with 100 nM PEG-AuNPs and an incubation time of 24 h, reaching on average 4.3×10^5 NPs internalized per cell. The sub-cellular distribution assay showed that approximately 15% to 20% of the internalized PEG-AuNPs were found to accumulate at the cell nucleus after 24 h of incubation (Figure 3.4 d), matching well with the results from the literature.[47, 51]

The uptake of the ^{125}I-PEG-AuNPs in 3D U87 cell spheroids was also evaluated for 10, 50 and 100 nM ^{125}I-PEG-AuNPs having 37 kBq ^{125}I. Surprisingly, the uptake of the ^{125}I-PEG-AuNPs in spheroids seems to be saturated after 4 h of incubation. At 24 h, the number of nanoparticles per spheroid in all groups was similar to, or even lower, than found at 4 h (Figure 3.4 c). Due to the small size and non-targeted nature of the ^{125}I-PEG-AuNPs, passive uptake, i.e. diffusion is the dominant transport pathway of the ^{125}I-PEG-AuNPs inside the spheroids. Nanoparticles taken up by spheroids have been reported to mostly localize in the interstitial space instead of being internalized inside the cells.[52] Based on the results from our 3D spheroids uptake experiments, we assume that the intravasation and extravasation of nanoparticles reached a balance around 4 h of incubation, thus leading to similar uptake at 4 h and 24 h. However, higher spheroid uptake at 24 h in comparison to 3 h has been reported in literature using negatively charged gold nanoparticles with a diameter of 2 nm and coated by a small molecule (tiopronin).[46] Thus, the PEG coating might hinder the penetration of the ^{125}I-PEG-AuNPs inside the spheroids, probably due to the steric hinderance between the nanoparticles and the spheroid extracellular matrix (ECM).[53-55]

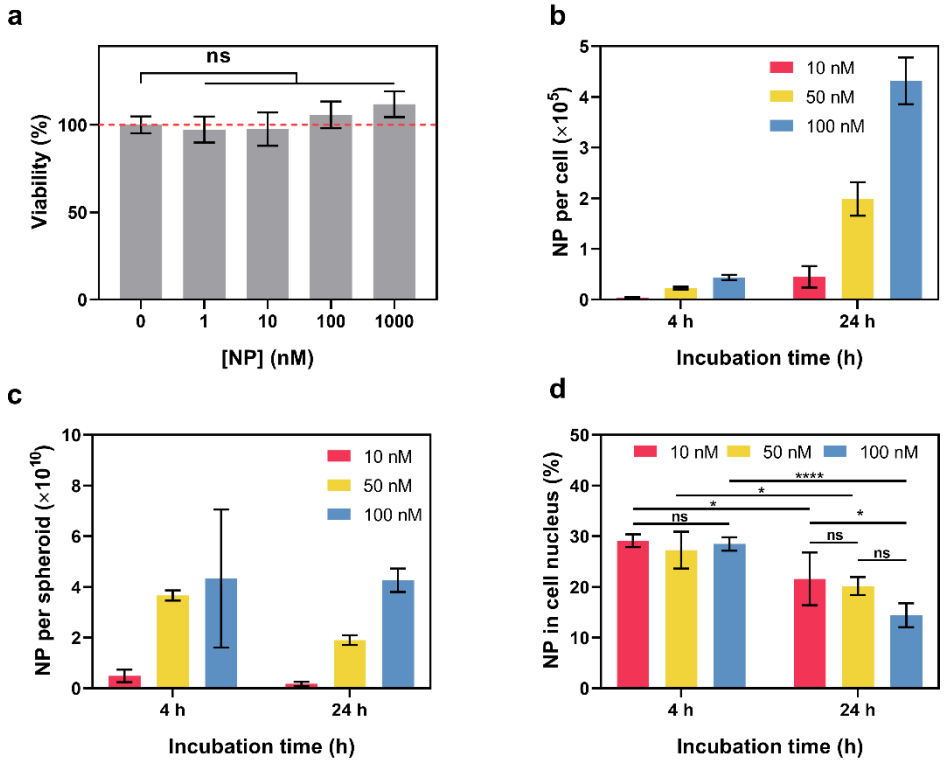

Figure 3.4. *In vitro* behavior of ^{125}I-PEG-AuNPs: a) viability of U87 cells treated with bare PEG-AuNPs at different concentrations, n=5; b) uptake of ^{125}I-PEG-AuNPs in U87 cell monolayers after 4 and 24 h incubation at 37 °C, data is shown as number of nanoparticles per single cell, n=3; c) uptake of ^{125}I-PEG-AuNPs in U87 cell spheroids after 4 and 24 h incubation at 37 °C, data is shown as number of nanoparticles per spheroid, n=3; d) Sub-cellular distribution of ^{125}I-PEG-AuNPs in U87 cell monolayers after 4 and 24 h incubation, data is shown as the percentage of nanoparticles present in the cell nucleus from all internalized nanoparticles, n=3.

Motivated by the accumulation of ^{125}I-PEG-AuNPs in the cell nucleus, the tumor killing efficiency of the ^{125}I-PEG-AuNPs was evaluated using both 2D and 3D *in vitro* cell models. U87 monolayer cells were treated by ^{125}I-PEG-AuNPs with ^{125}I activity ranging from 37 kBq to 740 kBq and an exposure time of 24 h. The viability of the cells was measured 24 h later after the removal of unbounded ^{125}I-PEG-AuNPs. As shown in Figure 3.5 a, a significant decrease in cell viability was detected after the treatment with the ^{125}I-PEG-AuNPs. The cell viability was reduced to only 36% when using 740 kBq ^{125}I. Moreover, the cells exhibited more than 95% viability after the treatment with 740 kBq [^{125}I]NaI, suggesting that the PEG-AuNPs played a vital role in cell killing.

After the measurement of cell viability, the DNA content of each sample was quantified

using a commercial dsDNA quantification kit. By comparing the DNA content of the ^{125}I-PEG-AuNPs treated groups with the control groups, the anti-proliferation effect of the ^{125}I-PEG-AuNPs on U87 could be determined.[56] As shown in Figure 3.5 b, a similar trend as found for the cell viability was observed for the proliferation efficiency of ^{125}I-PEG-AuNPs treated cells. The highest cell proliferate inhibition was achieved by 740 kBq ^{125}I-PEG-AuNPs where the proliferation efficiency was only 38%. The same ^{125}I activity of [^{125}I]NaI resulted in much less reduction on the cell proliferation efficiency (73%). The results of the DNA proliferation assay further supported the viability assay and clearly indicated that a high level of cell killing could be achieved by the ^{125}I-PEG-AuNPs.

The viability and DNA content of the U87 cells were also measured 48 h after the removal of ^{125}I-PEG-AuNPs. Reduction of cell viability and proliferation were again observed but were less pronounced compared to the 24 h results, probably due to repair of the inflicted DNA damage. (Figure S3.6)

To further verify the high tumor killing efficiency of the ^{125}I-PEG-AuNPs, a colony formation assay was performed to directly determine the level of cell reproductive death. The U87 cells were first treated by ^{125}I-PEG-AuNPs with increasing activity of ^{125}I ranging from 370 kBq to 3.7 MBq and then reseeded on 6-well plates for colony formation. The surviving fraction of each group was then calculated and shown in Figure 3.5 c. After being treated with 370 kBq and 740 kBq ^{125}I-PEG-AuNPs, the surviving fraction of U87 cells was reduced to ~70%. Increasing the ^{125}I from 370 kBq to 1 MBq resulted in a 3-fold decrease in surviving fraction, i. e. from 74% to 25%. When even higher ^{125}I activity (3.7 MBq) was applied, the surviving fraction was reduced to only 12% compared to the untreated cells.

As the spheroid models could mimic the difference between the actual tumor and monolayer cell models, the tumor killing efficiency of the ^{125}I-PEG-AuNPs was also assessed in U87 cell spheroids.[57] The size of the spheroids was monitored for up to 14 d after the treatment with ^{125}I-PEG-AuNPs. As shown in Figure 3.5 d, no difference between the volume of the ^{125}I-PEG-AuNPs treated spheroids and control spheroids was observed at early time points. On day 14, the growth of the treated spheroids seemed to be better controlled, while the untreated spheroids kept on growing. However, no influence of the administered ^{125}I activity on the spheroid growth was observed. This somewhat low response is most likely

due to the passive internalization of the ^{125}I-PEG-AuNPs, which might result in particles diffusing out of the spheroid. Despite the low uptake, the spheroids were continuously irradiated by ^{125}I over the 14 days incubation due to the long half-life of ^{125}I and resulted in better controlled growth. To determine whether the spheroid growth inhibition is a result of the treatment with the ^{125}I-PEG-AuNPs, spheroids were treated with 740 kBq [^{125}I]NaI, showing no obvious decrease of spheroid size over 14-days of incubation (Figure S3.7).

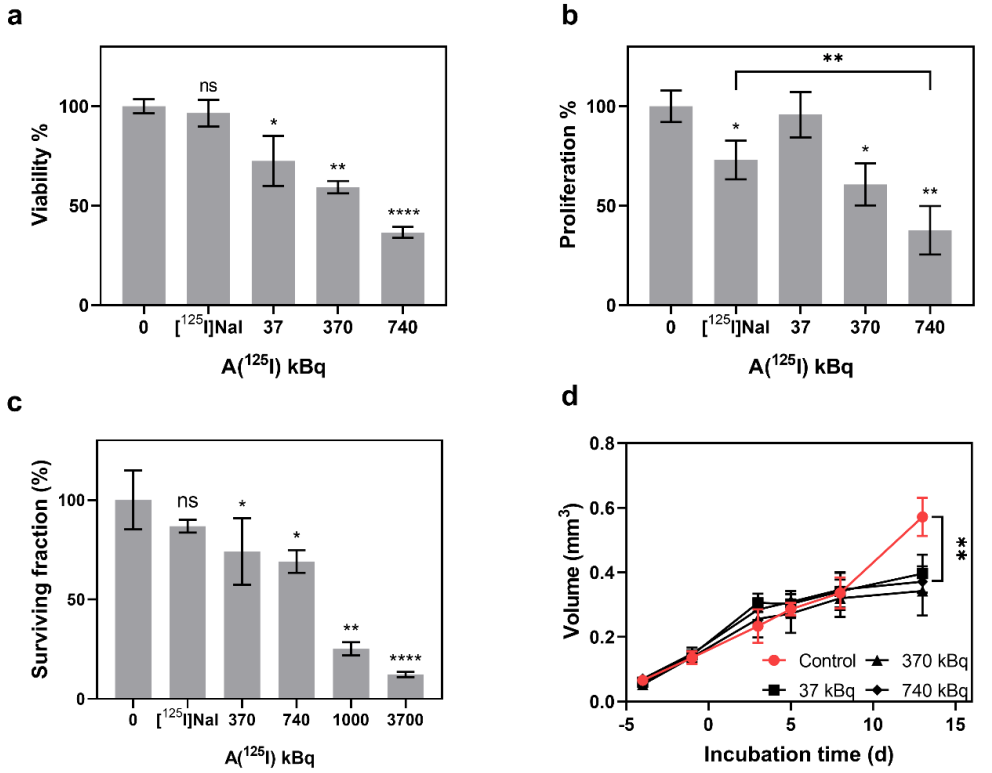

Figure 3.5. *In vitro* tumor killing efficiency of ^{125}I-PEG-AuNPs or [^{125}I]NaI with different ^{125}I activity determined by a) viability assay 24 h after removal of activity. The specific activity of the ^{125}I-PEG-AuNPs in each sample was 13.3 kBq/nM. The activity of [^{125}I]NaI was 740 kBq, n=4; b) DNA proliferation assay 24 h after removal of activity. The activity of [^{125}I]NaI is 740 kBq, n=4; c) colony formation assay. The specific activity of ^{125}I-PEG-AuNPs in each sample was 26.3 kBq/nM. The activity of [^{125}I]NaI is 3.7 MBq, n=3; d) 3D spheroid growth inhibition assay. The spheroids were treated by ^{125}I-PEG-AuNPs with 37, 370 or 740 kBq of ^{125}I for 24 h. The size change of the spheroids was monitored for another 13 d after the removal of activity. Non-treated spheroids were used as control, n=4.

In this work, we developed an ^{125}I based radiopharmaceutical using ultra-small gold nanoparticles as carriers and evaluated their tumor uptake and killing efficiency *in vitro*.

Compared with antibody or peptide-based carriers, the *in vitro* tumor uptake of the ^{125}I-PEG-AuNPs is modest. Possible reasons include the small size and the PEG coating on the AuNPs. The uptake mechanism of nanomaterials into cells is influenced by many factors including the size, surface charge and surface modification of the nanoparticles.[58] It has been experimentally shown that nanoparticles with a diameter of around 40 nm have the highest *in vitro* cell uptake while the uptake is lower for small nanoparticles (2~10 nm).[59] The formation of protein corona on the nanoparticles also plays an essential role in cell uptake. Previous research has proposed that higher uptake of 2 nm sized nanoparticles could be achieved at higher serum conditions.[60] In the case of our PEG-AuNPs, the protein interaction is minimized due to the coating of PEG molecules, thus lowering the cell uptake. To improve tumor uptake, targeting agents such as PSMA inhibitors could be used to modify the PEG-AuNPs while maintaining the small hydrodynamic diameter.[61]

Despite the modest uptake, the ^{125}I-PEG-AuNPs were found to kill the tumor cells efficiently as observed from the *in vitro* experiments. Due to the high number of AEs emitted by ^{125}I, even a tiny amount of activity accumulated in the nucleus might provide sufficient radiation dose to induce damage to the DNA molecules (Figure S3.5), especially when using an AE emitter with high yield of AEs such as ^{125}I (23.0 AEs per decay). Moreover, the interaction between ^{125}I and the gold surface also favors tumor cell killing. Gold nanoparticles have been widely applied as radiosensitizers in external beam radiation therapy (EBRT). As a high Z element, gold atoms can interact with photons or electrons and emit a high number of secondary photons and electrons which leads to higher tumor killing efficiency.[62] More specifically, it has been experimentally determined that depositing ^{125}I on a 2D gold film increased the yield of electrons by 600%.[63] Considering the high number of PEG-AuNPs internalized per cell, the radiation dose to the cells could be significantly amplified even in the presence of such a tiny amount of ^{125}I per cell.

Conclusions

In this work, we explored a new type of radiopharmaceutical using AE emitters and ultra-small nanoparticles. The high tumor killing efficiency of the ^{125}I-PEG-AuNPs was systematically studied using various *in vitro* models. The high tumor killing efficiency was attributed to accumulation of the nanoparticles in the cell nucleus as well as the high yield of AEs originating from ^{125}I. The results obtained from this work provide a new path for the application of AE emitters and hopefully offer new possibilities for cancer treatment.

References

[1] A. Dash, F. F Russ Knapp, M. Ra Pillai, *Current radiopharmaceuticals* **2013**, *6*, 152-180.
[2] J. P. Pouget, I. Navarro-Teulon, M. Bardies, N. Chouin, G. Cartron, et al., *Nat Rev Clin Oncol* **2011**, *8*, 720-734.
[3] C. a. Parker, S. Nilsson, D. Heinrich, S. I. Helle, J. O'sullivan, et al., *New England Journal of Medicine* **2013**, *369*, 213-223.
[4] T. Derlin, S. Schmuck, *The Lancet Oncology* **2018**, *19*, e372.
[5] M. S. Hofman, J. Violet, R. J. Hicks, J. Ferdinandus, S. P. Thang, et al., *The Lancet Oncology* **2018**, *19*, 825-833.
[6] J. Strosberg, G. El-Haddad, E. Wolin, A. Hendifar, J. Yao, et al., *New England Journal of Medicine* **2017**, *376*, 125-135.
[7] K. Clemens, B. Frank, L. G. Frederik, W. Mirjam, A. V. Frederik, et al., *Journal of Nuclear Medicine* **2016**, *57*, 1941.
[8] F. Buchegger, F. Perillo-Adamer, Y. M. Dupertuis, A. Bischof Delaloye, *European Journal of Nuclear Medicine and Molecular Imaging* **2006**, *33*, 1352-1363.
[9] R. W. Howell, K. S. Narra Vr Fau - Sastry, D. V. Sastry Ks Fau - Rao, D. V. Rao, *Radiat Res* **1993**, *134*, 71-78.
[10] A. I. Kassis, F. Fayad, B. M. Kinsey, S. R. S. Kandula, S. J. Adelstein, *Radiation Research* **1989**, *118*, 283-294.
[11] B. Cornelissen, M. D. Hu, K. McLarty, D. Costantini, R. M. Reilly, *Nuclear Medicine and Biology* **2007**, *34*, 37-46.
[12] A. Fasih, H. Fonge, Z. Cai, J. V. Leyton, I. Tikhomirov, et al., *Breast Cancer Research and Treatment* **2012**, *135*, 189-200.
[13] B. Cornelissen, A. Waller, C. Target, V. Kersemans, S. Smart, et al., *EJNMMI Research* **2012**, *2*, 9.
[14] A. Zereshkian, J. V. Leyton, Z. Cai, D. Bergstrom, M. Weinfeld, et al., *Nuclear Medicine and Biology* **2014**, *41*, 377-383.
[15] Y. J. Gu, J. Cheng, C. C. Lin, Y. W. Lam, S. H. Cheng, et al., *Toxicol Appl Pharmacol* **2009**, *237*, 196-204.
[16] M. Kodiha, Y. M. Wang, E. Hutter, D. Maysinger, U. Stochaj, *Theranostics* **2015**, *5*, 357-370.
[17] N. Panté, M. Kann, *Molecular Biology of the Cell* **2002**, *13*, 425-434.
[18] A. G. Tkachenko, H. Xie, D. Coleman, W. Glomm, J. Ryan, et al., *Journal of the American Chemical Society* **2003**, *125*, 4700-4701.
[19] J. M. de la Fuente, C. C. Berry, M. O. Riehle, A. S. G. Curtis, *Langmuir* **2006**, *22*, 3286-3293.
[20] L. Song, N. Falzone, K. A. Vallis, *International Journal of Radiation Biology* **2016**, *92*, 716-723.
[21] Z. Cai, N. Chattopadhyay, K. Yang, Y. L. Kwon, S. Yook, et al., *Nuclear Medicine and Biology* **2016**, *43*, 818-826.
[22] L. Song, S. Able, E. Johnson, K. A. Vallis, *Nanotheranostics* **2017**, *1*, 232.
[23] K. M. Tsoi, S. A. MacParland, X.-Z. Ma, V. N. Spetzler, J. Echeverri, et al., *Nature Materials* **2016**, *15*, 1212-1221.
[24] R. W. Howell, *Med Phys* **1992**, *19*, 1371-1383.
[25] M. W. Huang, S. M. Liu, L. Zheng, Y. Shi, J. Zhang, et al., *J Radiat Res* **2012**, *53*, 973-977.

[26] X. Hu, H. Qiu, L. Zhang, W. Zhang, Y. Ma, et al., *Cancer Biol Ther* **2012**, *13*, 840-847.
[27] S. B. Schwarz, N. Thon, K. Nikolajek, M. Niyazi, J. C. Tonn, et al., *Radiat Oncol* **2012**, *7*, 30.
[28] J. Chin, R. B. Rumble, M. Kollmeier, E. Heath, J. Efstathiou, et al., *J Clin Oncol* **2017**, *35*, 1737-1743.
[29] Z. Ji, Y. Jiang, S. Tian, F. Guo, R. Peng, et al., *Int J Radiat Oncol Biol Phys* **2019**, *103*, 638-645.
[30] Y. Chen, Y. Jiang, Z. Ji, P. Jiang, F. Xu, et al., *Brachytherapy* **2020**, *19*, 81-89.
[31] G. Mariani, A. Cei, P. Collecchi, J. Baranowska-Kortylewicz, A. D. Van den Abbeele, et al., *J Nucl Med* **1993**, *34*, 1175-1183.
[32] G. Mariani, P. Collecchi, L. Giuliani, J. Baranowska-Kortylewicz, L. Di Luca, et al., *Ann N Y Acad Sci* **1993**, *698*, 204-211.
[33] G. Mariani, P. Collecchi, S. Baldassarri, L. Di Luca, S. Buralli, et al., *J Nucl Med* **1996**, *37*, 16S-19S.
[34] A. I. Kassis, F. Fayad, B. M. Kinsey, K. S. Sastry, R. A. Taube, et al., *Radiat Res* **1987**, *111*, 305-318.
[35] S. K. Sahu, P. Y. Wen, C. F. Foulon, J. S. Nagel, P. M. Black, et al., *J Nucl Med* **1997**, *38*, 386-390.
[36] R. B. Michel, M. E. Castillo, P. M. Andrews, M. J. Mattes, *Clinical Cancer Research* **2004**, *10*, 5957-5966.
[37] M. Gardette, C. Viallard, S. Paillas, J. L. Guerquin-Kern, J. Papon, et al., *Invest New Drugs* **2014**, *32*, 587-597.
[38] Y. H. Kim, J. Jeon, S. H. Hong, W. K. Rhim, Y. S. Lee, et al., *Small* **2011**, *7*, 2052-2060.
[39] S. B. Lee, S. W. Lee, S. Y. Jeong, G. Yoon, S. J. Cho, et al., *ACS Appl Mater Interfaces* **2017**, *9*, 8480-8489.
[40] N. Su, Y. Dang, G. Liang, G. Liu, *Nanoscale Research Letters* **2015**, *10*, 160.
[41] J. Liu, M. Yu, X. Ning, C. Zhou, S. Yang, et al., *Angew Chem Int Ed Engl* **2013**, *52*, 12572-12576.
[42] J. Shi, P. W. Kantoff, R. Wooster, O. C. Farokhzad, *Nat Rev Cancer* **2017**, *17*, 20-37.
[43] M. J. Mitchell, M. M. Billingsley, R. M. Haley, M. E. Wechsler, N. A. Peppas, et al., *Nat Rev Drug Discov* **2021**, *20*, 101-124.
[44] H. S. Choi, W. Liu, P. Misra, E. Tanaka, J. P. Zimmer, et al., *Nat Biotechnol* **2007**, *25*, 1165-1170.
[45] B. Du, M. Yu, J. Zheng, *Nature Reviews Materials* **2018**, *3*, 358-374.
[46] K. Huang, H. Ma, J. Liu, S. Huo, A. Kumar, et al., *ACS Nano* **2012**, *6*, 4483-4493.
[47] S. Huo, S. Jin, X. Ma, X. Xue, K. Yang, et al., *ACS Nano* **2014**, *8*, 5852-5862.
[48] K. P. Kepp, *Inorg Chem* **2016**, *55*, 9461-9470.
[49] I. P. C. Murray, M. J. Spiro, J. B. Stanbury, *Journal of Chronic Diseases* **1961**, *14*, 473-483.
[50] P. Wang, W. J. Sun, Q. Wang, J. W. Ma, X. H. Su, et al., *Acs Appl Nano Mater* **2019**, *2*, 1374-1381.
[51] X. Jiang, B. Du, M. Yu, X. Jia, J. Zheng, *Journal of innovative optical health sciences* **2016**, *9*, 1642003-1642001 - 1642003-1642008.
[52] M. G. Roberts, V. J. Facca, R. Keunen, Q. Yu, R. M. Reilly, et al., *Biomacromolecules* **2022**, *23*, 3296-3307.
[53] A. E. Nel, L. Madler, D. Velegol, T. Xia, E. M. Hoek, et al., *Nat Mater* **2009**, *8*, 543-557.

[54] T. T. Goodman, P. L. Olive, S. H. Pun, *International journal of nanomedicine* **2007**, *2*, 265-274.
[55] D. L. Priwitaningrum, J.-B. G. Blondé, A. Sridhar, J. van Baarlen, W. E. Hennink, et al., *J Control Release* **2016**, *244*, 257-268.
[56] R. A. Nadar, N. Asokan, L. Degli Esposti, A. Curci, A. Barbanente, et al., *Nanoscale* **2020**, *12*, 13582-13594.
[57] J. Friedrich, C. Seidel, R. Ebner, L. A. Kunz-Schughart, *Nature Protocols* **2009**, *4*, 309-324.
[58] S. Behzadi, V. Serpooshan, W. Tao, M. A. Hamaly, M. Y. Alkawareek, et al., *Chemical Society Reviews* **2017**, *46*, 4218-4244.
[59] W. Jiang, B. Y. S. Kim, J. T. Rutka, W. C. W. Chan, *Nature Nanotechnology* **2008**, *3*, 145-150.
[60] F. Muraca, L. Boselli, V. Castagnola, K. A. Dawson, *ACS Appl Bio Mater* **2020**, *3*, 3800-3808.
[61] D. Luo, X. Wang, S. Zeng, G. Ramamurthy, C. Burda, et al., *Small* **2019**, *15*, e1900968.
[62] J. Xie, L. Gong, S. Zhu, Y. Yong, Z. Gu, et al., *Adv Mater* **2019**, *31*, e1802244.
[63] A. Pronschinske, P. Pedevilla, C. J. Murphy, E. A. Lewis, F. R. Lucci, et al., *Nat Mater* **2015**, *14*, 904-907.

Supplemental information

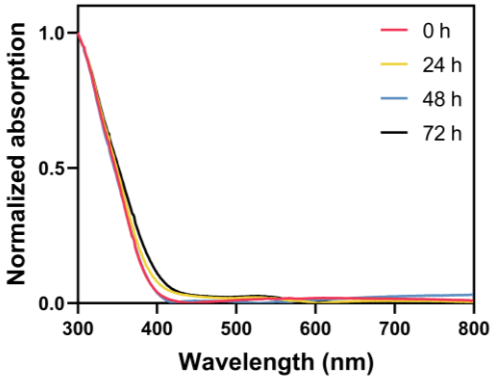

Figure S3.1. Normalized UV-vis spectrum of PEG-AuNPs in PBS over 72 h at 37 ℃.

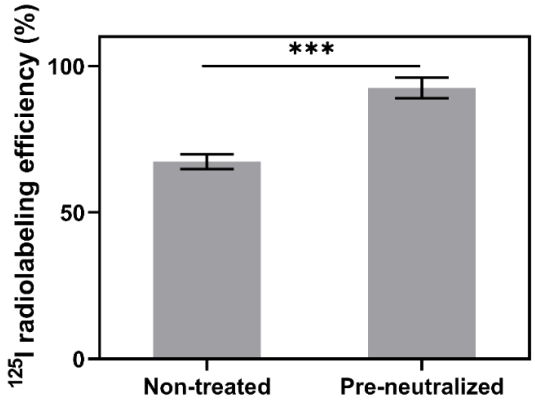

Figure S3.2. Radiolabeling efficiency of ^{125}I-PEG-AuNPs using [^{125}I]NaI solution at pH of 12~14 or neutralized to pH 7. The ^{125}I to NP ratio was set to 0.1 for all samples, n=3.

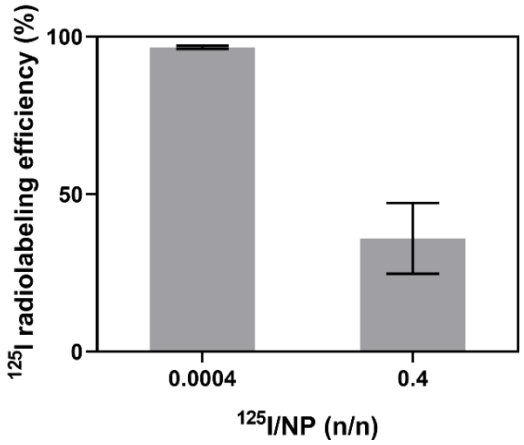

Figure S3.3. Radiolabeling efficiency of ^{125}I-PEG-AuNPs with various ^{125}I to NP ratios. [^{125}I]NaI solution was neutralized before the radiolabeling of all samples, n=3.

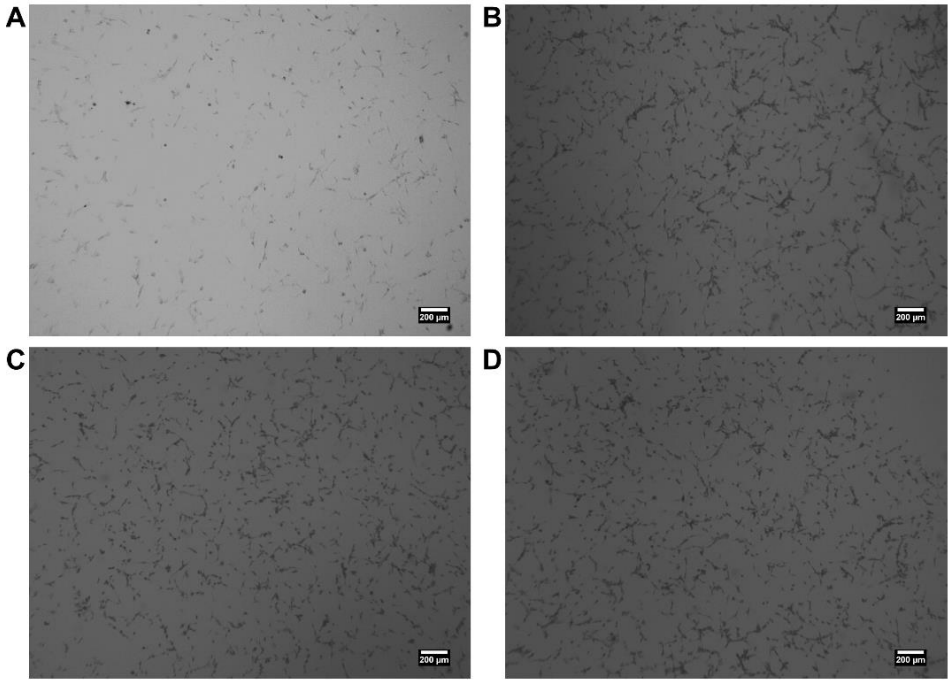

Figure S3.4. Silver staining of U87 monolayer cells treated by a) 0 nM; b) 1 nM; c) 50 nM and d) 100 nM bare PEG-AuNPs for 24 h. The scale bar is 200 µm. The increase contrast of the cells indicates the uptake of nanoparticles.

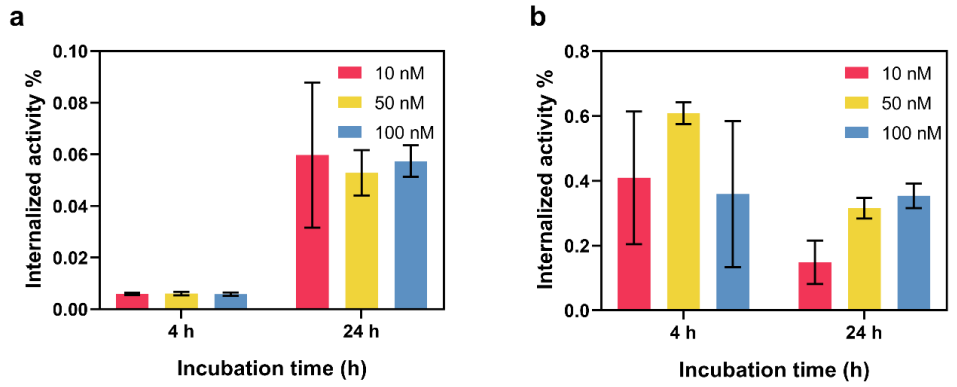

Figure S3.5. a) Uptake of ^{125}I-PEG-AuNPs in U87 cell monolayers after 4 and 24 h incubation at 37 °C, data is shown in percentage of initial ^{125}I activity, n=3; b) uptake of ^{125}I-PEG-AuNPs in U87 cell spheroids after 4 and 24 h incubation at 37 °C, data is shown in percentage of initial ^{125}I activity, n=3.

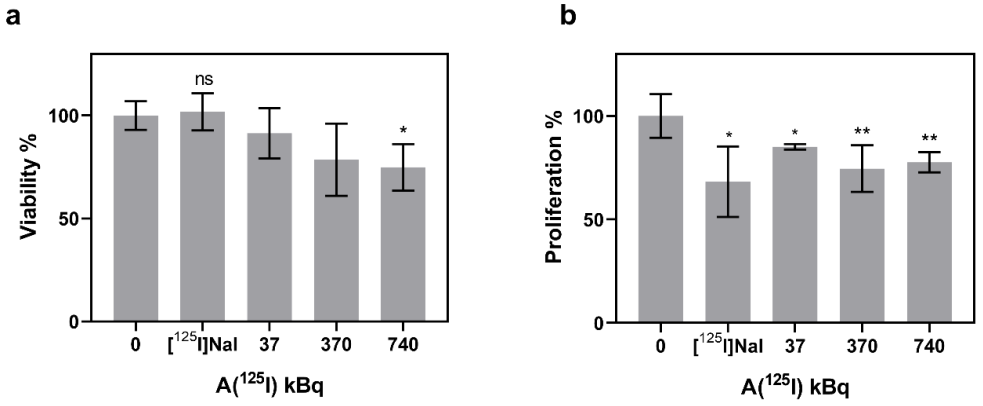

Figure S3.6. *In vitro* tumor killing efficiency of the ^{125}I-PEG-AuNPs with different ^{125}I activity or 740 kBq [^{125}I]NaI determined by a) viability assay 48 h after removal of activity, n=4; b) DNA proliferation assay 48 h after removal of activity, n=4.

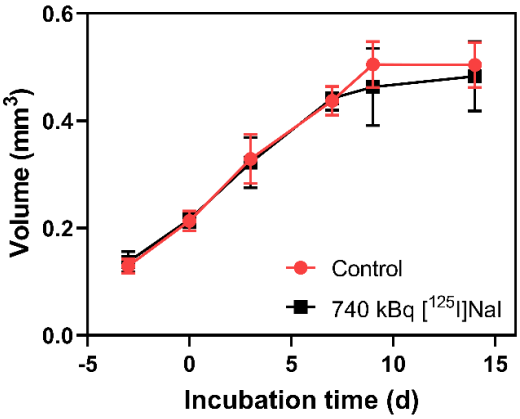

Figure S3.7. 3D spheroid growth inhibition assay of 740 kBq [^{125}I]NaI treated U87 spheroids. Non-treated spheroids were used as control, n=4.

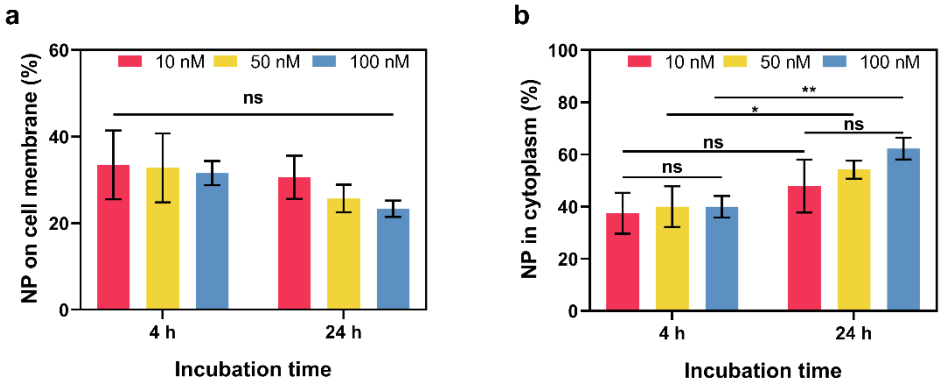

Figure S3.8. Sub-cellular distribution of ^{125}I-PEG-AuNPs on the a) cell membrane and b) in the cell cytoplasm of U87 cell monolayers after 4 and 24 h incubation, data is shown as percentage of all internalized nanoparticles, n=3.

4

Indium-111 radiolabeled ultra-small gold and silver telluride nanoparticles for radionuclide therapy

Abstract

Radionuclide therapy employing Auger electron emitters holds great potential for personalized cancer treatment. As the energy of the Auger electrons is mainly deposited surrounding their site of decay, tumor cells can be eliminated very efficiently while sparing healthy tissues. However, the short range of the Auger electrons requires the delivery of Auger emitters to the cell nucleus for sufficient DNA damage. In this work, we prepared indium-111 (^{111}In) radiolabeled ultra-small gold and silver telluride nanoparticles for Auger electron therapy. With a core diameter of 2 nm and a hydrodynamic diameter of less than 3 nm, both nanoparticles were found to accumulate in the cell nucleus after being internalized. 2D and 3D *in vitro* assays showed that these ^{111}In radiolabeled ultra-small nanoparticles are highly toxic to U87 cells. In conclusion, the delivery of ^{111}In to the cell nucleus can be significantly improved by using ultra-small nanoparticles as carriers, thereby achieving high tumor killing efficacy.

Key words: Indium-111, Auger therapy, gold nanoparticle, silver telluride nanoparticle, radionuclide therapy

Introduction

Radionuclide therapy is a cancer treatment modality that typically uses radionuclides coupled to targeting vectors to attack metastasized tumors.[1] Apart from the commonly used α and β^- particles, Auger electrons (AEs) could also be used for therapeutic applications.[2-3] AEs with energy from 10 eV to 10 keV are often emitted as a result of electron capture or β^+ decay. The emitted AEs can cause direct and indirect DNA damage, the latter being inducted through the generation of reactive oxygen species (ROS).[4-5] However, the range of the AEs is typically short, in the order of only a few nanometers. Thus, the AE emitters must be delivered close enough to vital cell organelles such as the cell nucleus to produce lethal damage.

Indium-111 (^{111}In) decays to stable cadmium-111 (^{111}Cd) by electron capture with a half-life ($t_{1/2}$) of 2.8 d. ^{111}In has been widely applied for single photon emission computed tomography (SPECT) imaging because of the emission of γ particles with suitable energies (245.35 keV and 171.28 keV).[6] In addition, ^{111}In emits 7.4 AEs per decay, making it also a potential candidate for Auger therapy.[7] In this sense, various antibodies or peptides have been radiolabeled with ^{111}In and applied in the treatment of prostate cancer, breast cancer and acute myelogenous leukemia, resulting in efficient tumor control in multiple *in vitro* and *in vivo* studies.[8-15] Although positive results have been obtained from these pre-clinical studies, no successful clinical trial of ^{111}In based therapeutic radiopharmaceuticals has been reported so far.[16]

The fast development of nanomaterials during the past years has boosted their applications in the medical field.[17] The physical properties of nanoparticles, including core composition, size, shape, surface charge and functionalization can be precisely controlled which facilitates their applications in drug delivery, imaging and tumor sensitization as boosters to other treatment modalities.[18]

Despite the great potential for medical applications, intravenously (i.v.) administrated nanoparticles with a hydrodynamic diameter larger than 5.5 nm tend to accumulate in the liver and spleen because of the mononuclear phagocyte system (MPS) capture.[19] As the hepatic excretion of nanoparticles from liver and spleen is slow, taking usually days to months, the long-term toxicity from the cargo of the nanoparticles or the nanoparticles themselves could be problematic.[20] To avoid high MPS uptake, the excretion pathways of

the nanoparticles can be altered to achieve renal clearance via the urinary system. The renal clearable nanoparticles (typically with a hydrodynamic diameter less than 5.5 nm) can escape from the MPS capture and be efficiently excreted from the body within hours to a few days.[21] Thus, the concerns regarding the long-term toxicity caused by MPS capture can be relieved by using such small nanoparticles.

Over the past 20 years, inorganic nanoparticles with sub-2 nm diameters have been extensively reported for medical applications.[22-24] Taking advantage of the favorable pharmacokinetics including fast excretion through renal clearance and rapid tumor uptake, these nanoparticles have been primarily developed for diagnostic applications.[25-28] Ultra-small glutathione-coated gold nanoparticles (GSH-AuNPs) and glutathione-coated silver telluride nanoparticles (GSH-Ag_2TeNPs) have been proposed as contrast agents for computed tomography (CT) due to the strong CT contrast of these elements.[28-29] Moreover, the GSH-AuNPs have also been pre-clinically utilized for fluorescent and nuclear imaging (PET and SPECT) facilitated by the emission of GSH-AuNPs in the infrared range and the possibility of being radiolabeled with diagnostic radionuclides.[30-31]

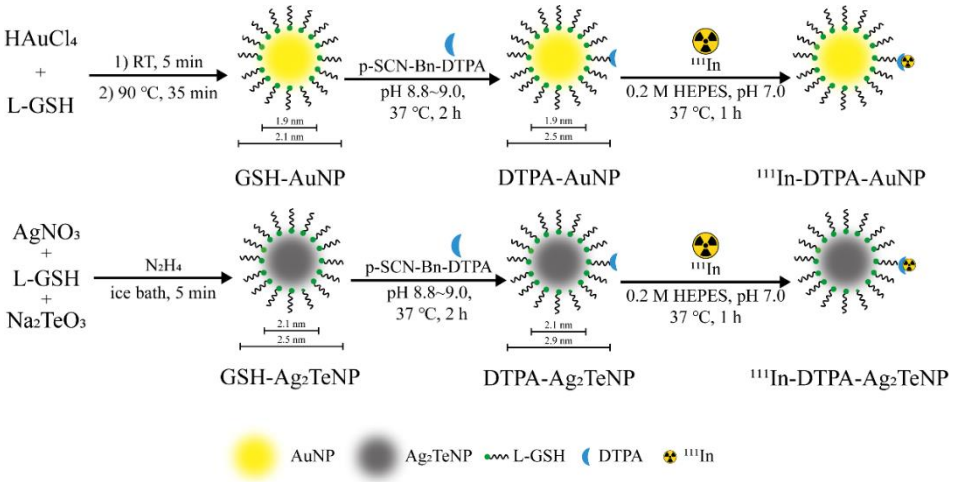

Figure 4.1. Schematic illustration of the synthesis, DTPA functionalization and ^{111}In radiolabeling of the GSH-AuNPs and GSH-Ag_2TeNPs.

In addition, a few ultra-small nanoparticles have been previously reported to passively accumulate at the cell nucleus after internalization, making them very attractive as carriers for AE emitters.[32-34] In this work, ultra-small GSH-AuNPs and GSH-Ag_2TeNPs were

synthesized and radiolabeled with ^{111}In (Figure 4.1). The total cell uptake as well as the fraction of nanoparticles accumulated in the cell nucleus were determined. Finally, the tumor killing efficiency of these two types of nanoparticles was evaluated by performing different *in vitro* assays.

Methods and materials

1. Materials

Gold(III) chloride trihydrate (≥ 99.9%), sodium tellurite (99%) and hydrazine hydrate (50%~60%) were purchased from Merck Sigma (Zwijndrecht, the Netherlands). Silver nitrate (≥ 99.9%), L-glutathione (≥ 98%), 5/6-carboxyfluorescein succinimidyl ester (FITC-NHS, > 90%) and sodium carbonate (≥ 98%) were ordered from Thermo Fisher Scientific (Landsmeer, the Netherlands). S-2-(4-Isothiocyanatobenzyl)-diethylenetriamine pentaacetic acid (p-SCN-Bn-DTPA, > 90%) and indium-111 ($^{111}InCl_3$ in 0.01 M HCl) were kindly provided by Erasmus Medical Center (Rotterdam, the Netherlands). All chemicals were used as received without further purification. Milli-Q water was obtained from an in-house Milli-Q system (Millipore) and used throughout this study.

2. Synthesis of ultra-small GSH-AuNPs

The GSH-AuNPs were synthesized as previously reported.[30] Typically, 94.5 mg (0.24 mmol) gold(III) chloride trihydrate ($HAuCl_4•3H_2O$) and 73.8 mg (0.24 mmol) L-glutathione (L-GSH) were weighed in a 20 ml glass bottle and dissolved in 10 mL water at room temperature. 30 µl 1 M $HAuCl_4•3H_2O$ was then added to the mixture and heated at 90 °C for 35 min. The obtained GSH-AuNPs were cooled down to room temperature and concentrated to 1.5 ml after being centrifuged at 4200 rpm for 15 min in Amicon centrifuge filters (MWCO=10 kDa). The GSH-AuNPs were then purified by passing through a disposable PD-10 column (GE Healthcare) using PBS buffer (pH 7.4) as the mobile phase. The fractions from 1.5 ml to 3 ml (V_{tot}=1.5 ml) were collected and stored at 4 °C.

3. Synthesis of ultra-small GSH-Ag_2TeNPs

The synthesis of GSH-Ag_2TeNPs was adapted from a previously reported protocol with minor adjustments.[28] In a typical synthesis, 1.5 ml 30 mM silver nitrite ($AgNO_3$), 1.5 ml 15

mM sodium tellurite (Na_2TeO_3) and 1.5 ml 90 mM reduced L-glutathione (L-GSH) were mixed in an ice bath. 0.5 ml hydrazine hydrate (50%-60% N_2H_4) was then quickly injected into the mixture. The mixture was vigorously mixed for 5 min. The as-prepared GSH-Ag_2TeNPs were washed twice with water and twice with PBS buffer (pH 7.4) using Amicon centrifuge filters (MWCO=10 kDa) at 4200 rpm for 20 min at 4 ℃. The final volume of the GSH-Ag_2TeNPs was adjusted to 2 ml by PBS and stored at 4 ℃ until further usage.

4. Characterizations

The morphology and size of the nanoparticles were studied with a JEM-1400 Plus transmission electron microscope (TEM, JEOL) at the acceleration voltage of 120 kV. The UV-vis absorption spectrum of both nanoparticles was measured using a UV-vis-NIR spectrophotometer (UV-6300PC, VWR). The luminescence spectra of the GSH-AuNPs were recorded using a Cary Eclipse fluorescence spectrophotometer (Agilent). The hydrodynamic diameter and zeta-potential of the nanoparticles were determined using a zeta-sizer (nano-ZS, Malvern). The Au or Ag content in the purified GSH-AuNPs and GSH-Ag_2TeNPs was determined using an ICP-MS (NexION® 2000, PerkinElmer) after being dissolved in aqua regia or concentrated nitric acid respectively. The results of ICP-MS measurements were used to calculate the concentrations of the nanoparticles. (The detailed calculation can be found in the Supplemental Information.)

5. Conjugation of FITC on GSH-Ag_2TeNPs

FITC was linked to GSH-Ag_2TeNPs via the NHS-amine reaction. In a typical reaction, 15 μl 7 mg/ml FITC-NHS in anhydrous DMSO was added to 1 ml of purified GSH-Ag_2TeNPs in PBS and reacted overnight at room temperature. The produced FITC-Ag_2TeNPs were washed thrice by PBS using Amicon centrifuge filters (MWCO=10 kDa) at 4 ℃ and redispersed in 1 ml PBS. The samples were stored at 4 ℃ and protected from light. To prove the successful linkage of FITC on the nanoparticles, the luminescent spectra of the FITC-Ag_2TeNPs and GSH-Ag_2TeNPs were recorded using a Cary Eclipse fluorescence spectrophotometer (Agilent, λ_{ex}=495 nm, λ_{em}=519 nm).

6. DTPA conjugation on GSH-AuNPs and GSH-Ag_2TeNPs

150 µl purified GSH-AuNPs were diluted to a total volume of 1 ml by PBS. The pH of the solution was adjusted to 8.8~9.0 by 0.1 M Na_2CO_3 (typically 38 µl). 15 µl of 13 mg/ml p-SCN-Bn-DTPA (10× molar excess to GSH-AuNPs) in anhydrous DMSO was then added. The reaction was continued at 37 °C for 2 h under constant shaking (800 rpm). Unconjugated DTPA was removed by washing the sample thrice in Amicon centrifuge filters (MWCO=10 kDa). The final volume of the DTPA-AuNPs dispersion was adjusted to 1.5 ml by 0.2 M HEPES pH 7.0 and stored at 4 ℃.

The conjugation of DTPA on GSH-Ag_2TeNPs was performed in the same way as described above. The obtained DTPA-Ag_2TeNPs were dispersed in 0.2 M HEPES pH 7.0, passed through a 20 nm syringe filter (GE Healthcare) and stored at 4 ℃ until further use.

7. Colloidal stability assay

The GSH-AuNPs, GSH-Ag_2TeNPs, DTPA-AuNPs and DTPA- Ag_2TeNPs were dispersed in PBS or 10% fetal bovine serum (FBS) in PBS and incubated at 37 °C for 72 h. The UV-vis spectrum of each sample was recorded every 24 h.

8. ^{111}In radiolabeling of DTPA-GSH-AuNPs and DTPA-GSH-Ag_2TeNPs

74 µl DTPA-AuNPs (20.2 µM) was added to 326 µl 0.2 M HEPES buffer (pH=7.0). Then 37 MBq of $^{111}InCl_3$ in 100 µl 0.2 M HEPES buffer (pH=7.0) was added to the DTPA-AuNPs and shaken at 37 °C for 1 h. After the reaction, the mixture was loaded on a PD-10 column and eluted by PBS. The elution was portioned per 500 µl and the ^{111}In activity in each fraction was determined using an automatic gamma counter (Wallac Wizard^2 2480, Perkin Elmer) to calculate the radiolabeling efficiency.

The ^{111}In radiolabeling of DTPA-Ag_2TeNPs was performed similarly. Typically, 166 µl DTPA-Ag_2TeNPs (13.7 µM) were mixed with 37 MBq of $^{111}InCl_3$. The total volume of this mixture was filled up to 500 µl with 0.2 M HEPES buffer (pH=7.0) and then reacted at 37 °C for 1 h. The obtained ^{111}In-DTPA-Ag_2TeNPs were then passed through a PD-10 column using PBS as eluent. The radiolabeling efficiency was also calculated in the same way as that of DTPA-AuNPs.

9. Radiochemical stability assay

The fractions containing ^{111}In-DTPA-AuNPs or ^{111}In-DTPA-Ag_2TeNPs were combined and added 10 µl 200 mM DTPA (pH=7.0) to achieve a final DTPA concentration of 1 mM. The mixture was then incubated at 37 °C for 24 h before being passed through a PD-10 column to separate the ^{111}In-DTPA-AuNPs or ^{111}In-DTPA-Ag_2TeNPs from free ^{111}In-DTPA. The radiochemical stability was then calculated by comparing the activity retained on the nanoparticles with the initial activity radiolabeled on the nanoparticles. (n=3)

10. Cell Culture

U87 human glioblastoma cells (ATCC) were cultured in complete Dulbecco's modified Eagle's medium (DMEM) supplemented with 10% FBS and 1% penicillin/streptomycin. The cells were incubated in a humidified environment at 37 ℃ with 5% CO_2.

11. Biocompatibility studies of GSH-AuNPs, GSH-Ag_2TeNPs, DTPA-AuNPs and DTPA-Ag_2TeNPs

U87 cells were seeded on 96-well plates with a cell density of 5000 cells/well. After being pre-incubated at 37 °C for 24 h, the cells were incubated with non-radioactive GSH-AuNPs, GSH-Ag_2TeNPs, DTPA-AuNPs and DTPA-Ag_2TeNPs with concentrations ranging from 1 nM to 1000 nM for another 24 h. The viability of the treated cells was determined by CCK-8 assay after washing the cells thrice with PBS. The viability of non-treated cells was also measured as a control. (n=3)

12. *In vitro* cell uptake of ^{111}In-DTPA-AuNPs and ^{111}In-DTPA-Ag_2TeNPs

2D uptake: U87 cells were seeded on 12-well plates and pre-incubated for 24 h (8×10^4 cells/well). On the next day, 1 ml fresh culture medium containing 10, 50, 100 nM ^{111}In-DTPA-AuNPs or ^{111}In-DTPA-Ag_2TeNPs (18 kBq) was added to the cells and incubated for 4 h or 24 h at 37 ℃. The cells were then washed three times with PBS and detached by trypsin. The separation of the sub-cellular fractions was achieved using the Subcellular Protein Fractionation Kit (Thermo Scientific) following the instructions from the manufacturer. The activity of ^{111}In of each cell fraction was measured by an automated gamma counter (Wallac Wizard^2 2480, Perkin Elmer) and summed up to calculate the total uptake. The cell uptake and subcellular distribution of ^{111}In-DTPA (18 kBq) were also measured for comparison. (n=3)

3D uptake: The spheroids were formed by seeding U87 cells in U-shaped 96-well plates (2000 cells/well). 7-days old U87 spheroids were then incubated with 10, 50, 100 nM ^{111}In-DTPA-AuNPs or ^{111}In-DTPA-Ag_2TeNPs (18 kBq) for 4 h or 24 h at 37 ℃. The spheroids were washed thrice by PBS before the measurements of activity in the washing solutions and the spheroids using an automated gamma counter (Wallac Wizard^2 2480, Perkin Elmer). The uptake of ^{111}In-DTPA (18 kBq) in U87 spheroids was also measured for comparison. (n=4)

13. Confocal microscope

Approximately 2×10^4 U87 cells/well were seeded on a μ-Slide 8 well high-chambered coverslip (ibidi GmbH, Germany) and pre-incubated for 24 h. On the next day, the cells were treated with 300 μl 100 nM FITC-Ag_2TeNPs in culture medium and incubated for another 24 h. The cells were then washed thrice by PBS before being fixed with 4% paraformaldehyde for 10 min and stained with diamidino-2-phenylindole (DAPI, Invitrogen) for 10 min. The confocal images were acquired using a Zeiss LSM 980 confocal microscope and analyzed by Zeiss Zen 3.8 software.

14. *In vitro* cytotoxicity of ^{111}In radiolabeled GSH-AuNPs and GSH-Ag_2TeNPs

2D Viability assay: U87 cells were seeded on 96-well plates and pre-incubated for 24 h (5000 cells/well). On the next day, the cells were treated by ^{111}In-DTPA-AuNPs or ^{111}In-DTPA-Ag_2TeNPs with 74~1480 kBq ^{111}In for 24 h. The cells were then washed thrice with PBS and incubated for another 24 hours before the determination of the viability using CCK-8 (Dojindo). The viability of non-treated cells was also measured and used as a control. (n=4)

2D colony formation assay: U87 cells were seeded on 12-well plates (8×10^4 cells/well) and pre-incubated at 37 ℃ for 24 hours. ^{111}In-DTPA-AuNPs or ^{111}In-DTPA-Ag_2TeNPs with 1, 2 and 3 MBq ^{111}In or 3 MBq ^{111}In-DTPA were then added to the cells and incubated at 37 ℃ for 24 h. After the treatment, the cells were washed thrice by PBS, reseeded on 6-well plates with a cell density of 500 cells/well and left undisturbed for 14 days to allow colony formation. The culture medium was refreshed every 3 days. On the last day of incubation, the colonies were fixed by 4% (w/v) paraformaldehyde, stained by 1% crystal violet and counted manually. (n=3)

3D cell growth inhibition assay: 7-days old U87 spheroids (seeding density=2000 cells/well) were treated with ^{111}In-DTPA-AuNPs or ^{111}In-DTPA-Ag_2TeNPs with 0.37 and 1 MBq ^{111}In

or 1 MBq of ^{111}In-DTPA and incubated at 37 °C for 24 h. After the treatment, the spheroids were washed three times with PBS and supplied with fresh culture medium. The spheroids were then cultured for another 14 days. The culture medium was refreshed every 3 days. The size of the spheroids was measured at multiple time points and analyzed using ImageJ. The size of untreated spheroids was also measured and used as a control. (n=4)

15. Statistical Analysis

Data are expressed as mean ± standard deviation based on at least three independent replicates. Student's t-test was used for the comparison between the two samples. For the comparison among multiple samples, one-way or two-way ANOVA test was performed. P values: ns $p>0.05$, $^{*}p\leq0.05$, $^{**}p\leq0.01$, $^{***}p\leq0.001$, $^{****}p\leq0.0001$.

Results and discussion

Besides being extensively applied in SPECT imaging, ^{111}In also shows great potential for cancer treatment considering its emission of 7.4 AEs per decay. However, the development of Auger therapy is challenging mainly because of the short range of the AEs. In previous studies, ^{111}In has been radiolabeled on 14~30 nm gold nanoparticles modified with tumor targeting peptides which simultaneously enabled transportation of ^{111}In to the cell nucleus and amplified the radiation dose via the radiosensitizing effects.[35-37] However, high liver uptake of these ^{111}In radiolabeled nanoparticles has been observed in the *in vivo* studies due to the MPS capture.

To avoid high MPS uptake, ultra-small GSH-AuNPs and GSH-Ag_2TeNPs were chosen as the carriers for ^{111}In in this work. Both types of nanoparticles have been extensively studied in cancer imaging as CT contrast agents and have shown remarkable pharmacokinetic properties. Specifically, these particles can escape from the MPS capture and be quickly eliminated from the body via renal clearance.[28, 30] In this work, the therapeutic application of these ultra-small nanoparticles was explored. Due to their small sizes, these nanoparticles might passively migrate inside the cell nucleus after being internalized. In this case, ^{111}In could be delivered to the cell nucleus when being radiolabeled on these nanoparticles, hereby producing severe DNA damage.

The GSH-AuNPs and the GSH-Ag_2TeNPs were both synthesized using reactions in aqueous phase without the use of organic solvents. In the case of GSH-AuNPs, the gold salts were reduced and capped by L-GSH under heating. The GSH-Ag_2TeNPs were produced by reducing silver salts by hydrazine in an ice bath with the presence of L-GSH as capping ligands. The shape and size of the nanoparticles were characterized by TEM and shown in Figure 4.2 a and d. Both nanoparticles were quasi-spherically shaped and had similar core diameters of 1.9 ± 0.4 nm and 2.1 ± 0.3 nm for GSH-AuNPs and GSH-Ag_2TeNPs respectively. Due to the GSH coating on the nanoparticle surface, the hydrodynamic diameters of both nanoparticles were slightly larger than their core sizes but were still less than 3 nm (Figure 4.2 b and e). Due to the high sensitivity of the UV-vis spectrum to size change, the UV-vis spectrum of GSH-AuNPs and the GSH-Ag_2TeNPs was recorded and shown in Figure 4.2 c and f. No obvious peaks were observed from the spectrum, further confirming the small size of these nanoparticles.[25, 28, 30] The zeta-potential measurements showed that both nanoparticles were negatively charged (Figure S4.1 a). In addition, the zeta-potential values of both nanoparticles were found to be lower than -30 mV, suggesting high colloidal stability.[38]

The GSH-AuNPs have been reported to have fluorescent emission in the infrared range. As shown in Figure S4.2, the GSH-AuNPs prepared in this work also exhibited an emission peak at 810 nm when using an excitation wavelength of 340 nm, matching well with the literature results.[29]

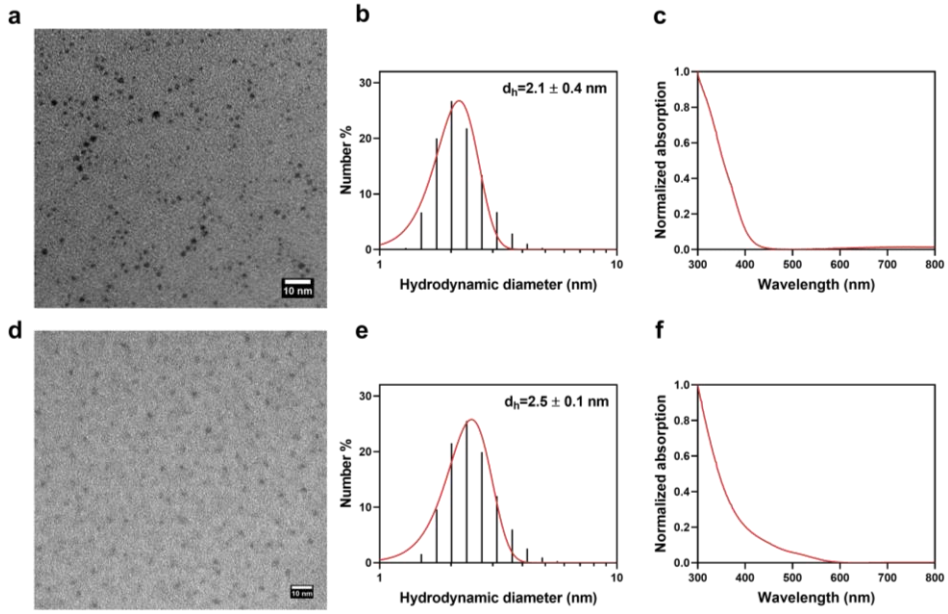

Figure 4.2. Characterization of GSH-AuNPs and GSH-Ag_2TeNPs: a-c) TEM image, number based hydrodynamic diameter and normalized UV-vis spectrum of GSH-AuNPs, scale bar=10 nm; d-f) TEM image, number based hydrodynamic diameter and normalized UV-vis spectrum of GSH-Ag_2TeNPs, scale bar=10 nm. The nanoparticles were dispersed in PBS buffer for the DLS and UV-vis measurements.

The colloidal stability of the nanoparticles in physiological solutions was investigated by dispersing the nanoparticles in PBS or 10% FBS and incubated at 37 °C for 72 h. The UV-vis spectrum of each sample was recorded every 24 hours as an indication of size change or the formation of aggregates. As shown in Figure 4.3, no significant change was observed from the UV-vis spectrum of both nanoparticles after being incubated in either PBS buffer or 10% FBS for 72 h, suggesting high colloidal stability. The high resistance against protein adsorption could be attributed to the zwitterionic coating provided by GSH which hindered protein binding.

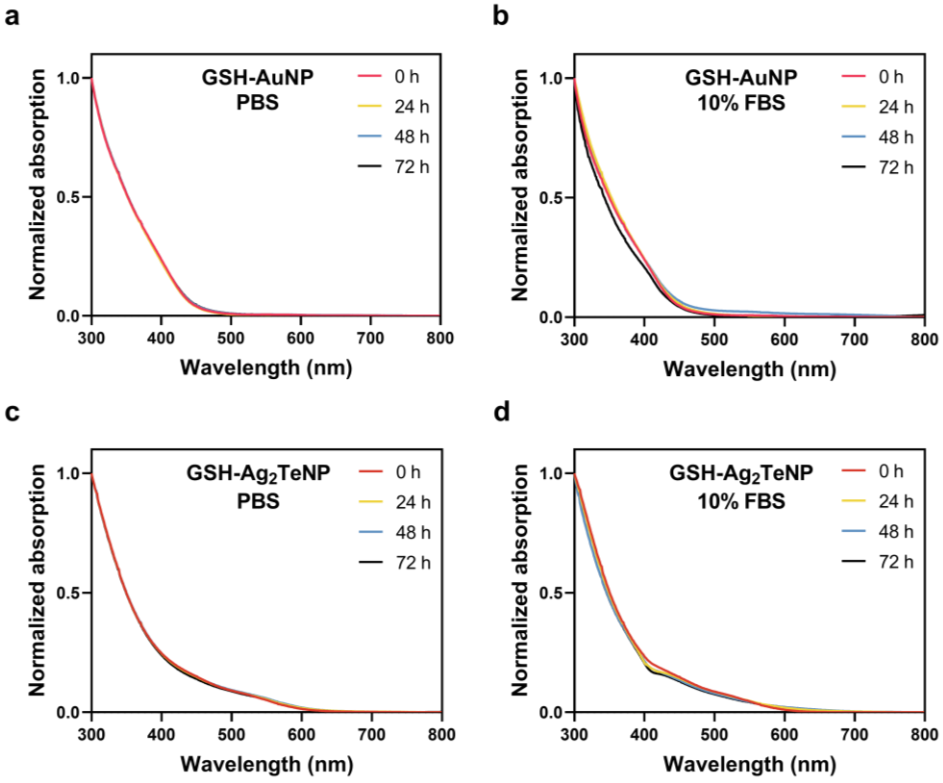

Figure 4.3. Colloidal stability of GSH-AuNPs and GSH-Ag_2TeNPs. The nanoparticles were dispersed in either PBS or 10% FBS in PBS and incubated at 37 °C for 72 h. The normalized UV-vis spectrum of GSH-AuNPs in a) PBS, b) 10% FBS and GSH-Ag_2TeNPs in c) PBS, d) 10% FBS was recorded every 24 h.

Subsequently, the nanoparticles were functionalized with DTPA via the reaction of the amine groups available on the nanoparticle surface with excess dosage of p-SCN-Bn-DTPA. The hydrodynamic diameters of both nanoparticles were found to be slightly increased by 0.4 nm as a result of DTPA linkage (Figure S4.3 a&c). No obvious difference in the UV-vis spectrum was detected before and after DTPA conjugation (Figure S4.3 b&d). A small increase in the zeta-potential values of both nanoparticles was observed after the conjugation of DTPA (Figure S4.1 b).

In the next step, the radiolabeling of the DTPA-AuNPs and DTPA-Ag_2TeNPs with ^{111}In was performed. Typically, 100× molar excess of the DTPA modified nanoparticles to $^{111}In^{3+}$ ions were required to achieve a high radiolabeling efficiency. After the reaction, size exclusion columns (PD-10 in this work) were used to purify the products. Typical elution

profiles of ^{111}In-DTPA-AuNPs and ^{111}In-DTPA-Ag_2TeNPs on PD-10 columns using PBS as eluent can be found in Figure S4.4, which clearly demonstrates that free ^{111}In ions were separated from the nanoparticles. For the ^{111}In-DTPA-AuNPs, fractions 4-7 were collected while fractions 4-10 were collected for the ^{111}In-DTPA-Ag_2TeNPs. The radiolabeling efficiency was determined as 89.4 ± 1.8% and 72.8 ± 1.8% for ^{111}In-DTPA-AuNPs and ^{111}In-DTPA-Ag_2TeNPs respectively (Figure 4.4 a).

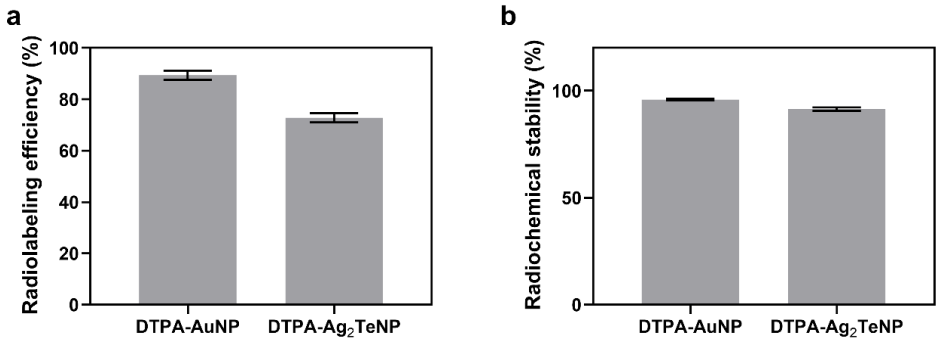

Figure 4.4. a) Radiolabeling efficiency of ^{111}In-DTPA-AuNPs and ^{111}In-DTPA-Ag_2TeNPs, n=5; b) radiochemical stability of ^{111}In-DTPA-AuNPs and ^{111}In-DTPA-Ag_2TeNPs after being incubated in PBS containing 1 mM DTPA for 24 h at 37 ℃, n=3.

The radiochemical stability was evaluated by incubating the purified ^{111}In-DTPA-AuNPs and ^{111}In-DTPA-Ag_2TeNPs in PBS containing 1 mM DTPA for 24 hours at 37 ℃. The loosely bounded ^{111}In was captured by DTPA and then separated from the nanoparticles by passing the product through a PD-10 column. As shown in Figure 4.4 b, high radiochemical stability (>95%) under DTPA challenge was achieved for both nanoparticles.

Before performing any biological studies, the biocompatibility of bare and DTPA-modified GSH-AuNPs and GSH-Ag_2TeNPs was first evaluated. The viability of U87 cells was measured after being incubated with either type of nanoparticles for 24 h. As shown in Figure S4.5, all the nanoparticles were found to be non-toxic to U87 cells at all tested concentrations, suggesting that all of these nanoparticles were suitable for biological applications.

The uptake and sub-cellular distribution of ^{111}In-DTPA-AuNPs and ^{111}In-DTPA-Ag_2TeNPs in 2D U87 cells were determined after incubating the cells with 10, 50 or 100 nM of each type of nanoparticles for 4 or 24 hours (Figure 4.5). Regarding the percentage of

internalized ^{111}In activity, the uptake of ^{111}In-DTPA-AuNPs was found to increase by 5~6 times when extending the incubation time from 4 h to 24 hours (Figure 4.5a). Higher cell uptake was also achieved by increasing the nanoparticle concentrations from 10 nM to 100 nM. The highest uptake (0.8 %) was achieved after treating the cells with 100 nM ^{111}In-DTPA-AuNPs for 24 h and was significantly higher than that of ^{111}In-DTPA. The number of internalized ^{111}In-DTPA-AuNPs per cell was also calculated based on the percentage of internalized ^{111}In activity and was found to be in the order of 10^6 nanoparticles/cell (Figure 4.5 b).

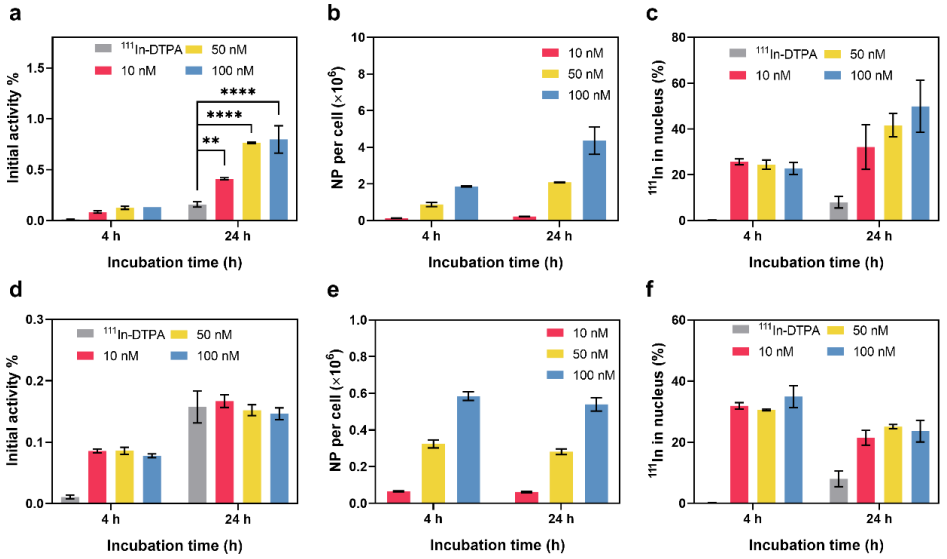

Figure 4.5. *In vitro* uptake of ^{111}In-DTPA-AuNPs (a-c) and ^{111}In-DTPA-Ag_2TeNPs (d-f) in 2D U87 cells with various nanoparticle concentrations and an incubation time of 4 or 24 h. a) and d) uptake of ^{111}In-DTPA-AuNPs and ^{111}In-DTPA-Ag_2TeNPs in U87 cell monolayers. The uptake of ^{111}In-DTPA using the same ^{111}In activity was also measured for comparison. The results are presented as percentage of the initially added activity, n=3; b) and e) number of internalized ^{111}In-DTPA-AuNPs and ^{111}In-DTPA-Ag_2TeNPs per cell, n=3; c) and f) percentage of ^{111}In-DTPA-AuNPs and ^{111}In-DTPA-Ag_2TeNPs accumulated in cell nucleus determined by sub-cellular fractionation, n=3.

In the case of ^{111}In-DTPA-Ag_2TeNPs, the 4 h uptake was found to be comparable with that of ^{111}In-DTPA-AuNPs, around 0.1% of the initially added ^{111}In activity (Figure 4.5 d). However, the 24 h uptake of ^{111}In-DTPA-Ag_2TeNPs was not as high as that of the ^{111}In-DTPA-AuNPs but only comparable to that of ^{111}In-DTPA. The largest difference was found from the 100 nM groups where the uptake of ^{111}In-DTPA-Ag_2TeNPs was about 5.5 times lower than that of ^{111}In-DTPA-AuNPs (0.15% versus 0.80%). Due to the lower cell uptake, the number

of internalized ^{111}In-DTPA-Ag_2TeNPs per cell was also less (Figure 4.5 e). Moreover, increasing the concentration of ^{111}In-DTPA-Ag_2TeNPs did not lead to obvious improvement in cell uptake.

Due to the short range of the AEs, ^{111}In must be delivered to the cell nucleus for maximum DNA damage. Thus, the fraction of internalized activity in the cell nucleus is an important factor for estimating the damage to tumor cells. As shown in Figure 4.5 c and f, 49.8% and 23.6% of the internalized ^{111}In-DTPA-AuNPs and ^{111}In-DTPA-Ag_2TeNPs were found to accumulate in the cell nucleus respectively (100 nM concentration and 24 hours incubation). The uptake of ^{111}In-DTPA-AuNPs and ^{111}In-DTPA-Ag_2TeNPs in cell nucleus was surprisingly high and even comparable to some of the ^{111}In radiolabeled cell nucleus-targeting peptides.[8, 10, 15] The high nucleus uptake suggests that both nanoparticles are very likely to induce DNA damage to the tumor cells provided that sufficient activity of ^{111}In is taken up by the cells.

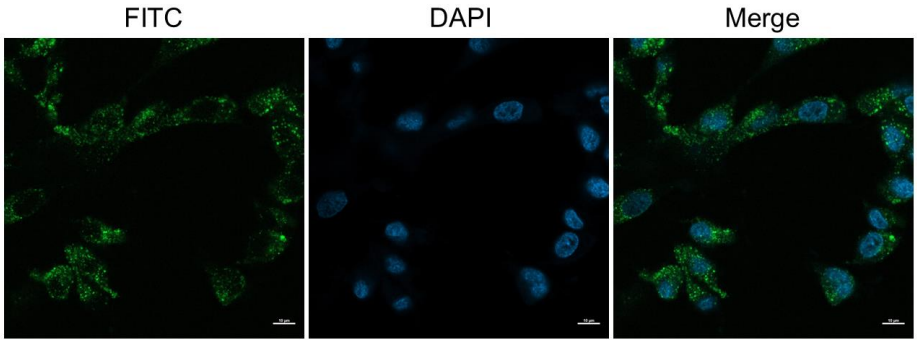

Figure 4.6. Confocal images of U87 cells after 24 h incubation with FITC-Ag_2TeNPs. The concentration of the NPs was 100 nM. The cell nucleus was stained by DAPI (blue, middle) while the FITC-Ag_2TeNPs showed a green fluorescence (left). The merged image (right) indicates the co-localization of FITC-Ag_2TeNPs and the cell nucleus. Scale bar=10 µm.

To further confirm the localization of the nanoparticles in the cell nucleus, we modified the GSH-Ag_2TeNPs with FITC and checked their distribution in U87 cells using confocal microscopy. The linkage of FITC was achieved by the NHS-amine reaction taking advantage of the high number of free amine groups available from the GSH coating. The successful FITC modification was confirmed by measuring the emission spectrum and the UV-vis spectrum of FITC-Ag_2TeNPs (Figure S4.6). The confocal images shown in Figure 4.6 revealed that the FITC signal can be observed in the cell nucleus. In addition to the nucleus,

even stronger FITC signal was observed in the cytoplasm and the cell membrane, matching well with the results of the sub-cellular fractionation assays (Figure S4.7).

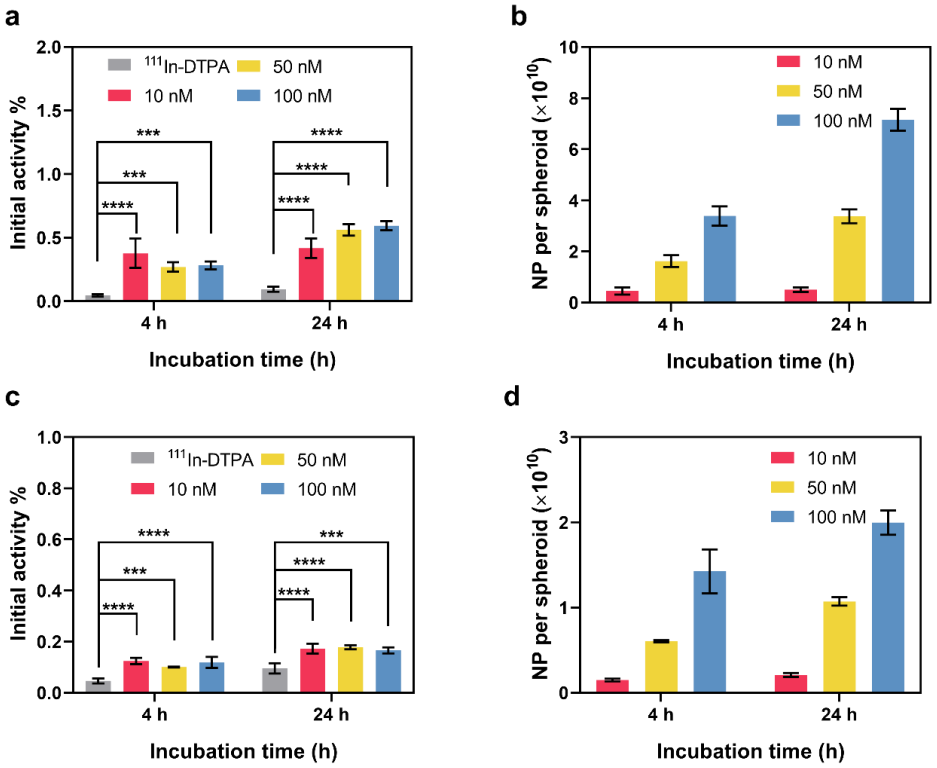

Figure 4.7. *In vitro* uptake of ^{111}In-DTPA-AuNPs (a-b) and ^{111}In-DTPA-Ag_2TeNPs (c-d) in 3D U87 spheroids for various nanoparticle concentrations and at incubation time of 4 or 24 h. The results are presented as percentage of the initially added activity (a and c) as well as nanoparticles per spheroid (b and d), n=4.

The 3D spheroid model resembles actual tumors better than the 2D monolayer model.[39] Therefore, we also evaluated the uptake of the ^{111}In-DTPA-AuNPs and ^{111}In-DTPA-Ag_2TeNPs in U87 cell spheroids. Comparing with the control group, ^{111}In uptake was significantly higher among the groups treated with either type of nanoparticles at both 4 h and 24 h (Figure 4.7 a&c). The concentration of the nanoparticles seemed to have a very small effect on the uptake in spheroids when given in percentage of internalized activity. But when converting the results to nanoparticles per spheroid, this difference became more pronounced, i.e. higher nanoparticle concentrations resulted in much more nanoparticles per spheroid (Figure 4.7 b&d). The highest uptake of ^{111}In-DTPA-AuNPs was found to be 0.6% of the initially added ^{111}In (corresponding to 7×10^{10} nanoparticles per spheroid) when a

concentration of 100 nM and 24 h incubation time were applied, similar to what has been observed in the 2D models (Figure 4.7 a). For the ^{111}In-DTPA-Ag_2TeNPs, the highest uptake was found to be 0.17%, approximately 3 times lower than that of ^{111}In-DTPA-AuNPs (Figure 4.7 c).

Next, we evaluated the tumor killing efficiency of the ^{111}In-DTPA-AuNPs and ^{111}In-DTPA-Ag_2TeNPs by performing a viability assay. As shown in Figure 4.8 a, the reduction of cell viability was observed among all groups treated with ^{111}In-DTPA-AuNPs with as low as 74 kBq ^{111}In. The lowest cell viability was found to be 85% corresponding to the group treated with ^{111}In-DTPA-AuNPs containing 1.48 MBq ^{111}In. On the contrary, no significant reduction of cell viability was found among all groups treated with ^{111}In-DTPA-Ag_2TeNPs.

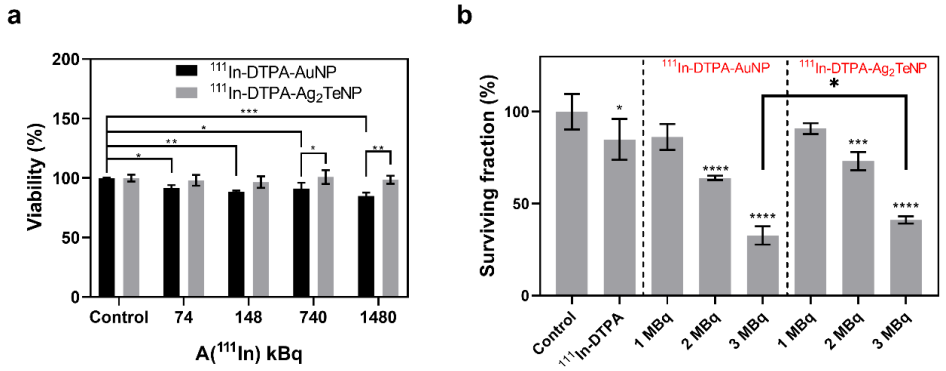

Figure 4.8. *In vitro* tumor killing efficiency of ^{111}In-DTPA-AuNPs and ^{111}In-DTPA-Ag_2TeNPs as determined by a) viability assay performed 24 h after the removal of activity, n=3; b) colony formation assay after 24 h of incubation with ^{111}In-DTPA-AuNPs and ^{111}In-DTPA-Ag_2TeNPs. The tumor killing efficiency of ^{111}In-DTPA (3 MBq) was also measured for comparison, n=3. The specific activity of ^{111}In-DTPA-AuNPs and ^{111}In-DTPA-Ag_2TeNPs were 14.4 kBq/nM and 11.9 kBq/nM respectively.

To better investigate the production of reproductive damage, we also performed a colony formation assay using both types of nanoparticles with ^{111}In activity ranging from 1 MBq to 3 MBq (Figure 4.8 b). After the treatment of ^{111}In-DTPA-AuNPs or ^{111}In-DTPA-Ag_2TeNPs, the surviving fractions of the cells decreased significantly compared to that of non-treated cells. In particular, the cell surviving fraction was reduced to 32.7% and 41.2% after treatment with 3 MBq of ^{111}In-DTPA-AuNPs and ^{111}In-DTPA-Ag_2TeNPs respectively. Meanwhile, treatment with the same activity of ^{111}In-DTPA only decreased the cell surviving fraction by 15%, indicating the important role of the small nanoparticles in cell killing. However, there was only 10% difference on the reduction of cell survival when comparing the cell death

caused by ^{111}In-DTPA-AuNPs and ^{111}In-DTPA-Ag_2TeNPs, despite the much higher cell uptake of the ^{111}In-DTPA-AuNPs in 2D cells.

Subsequently, we investigated the tumor killing efficiency of the ^{111}In-DTPA-AuNPs and ^{111}In-DTPA-Ag_2TeNPs in 3D cell spheroids. The size change of the spheroids was tracked for 14 days after being treated with the ^{111}In radiolabeled nanoparticles or ^{111}In-DTPA. As shown in Figure 4.9, significant growth inhibition of the spheroids treated by 1 MBq ^{111}In-DTPA-AuNPs and ^{111}In-DTPA-Ag_2TeNPs was observed on day 14, while no obvious difference in size between the treated spheroids and the controls was found at earlier time points. Similar to the results obtained from the 2D assays, the treatment of ^{111}In-DTPA had no influence on the spheroid growth. To compare the growth inhibition effect of the ^{111}In-DTPA-AuNPs and ^{111}In-DTPA-Ag_2TeNPs, the size of the spheroids on day 14 was normalized to controls and shown in Figure S4.8. It is interesting to note that the spheroid growth inhibition effect was not significantly different between ^{111}In-DTPA-AuNPs and ^{111}In-DTPA-Ag_2TeNPs despite the rather different uptake.

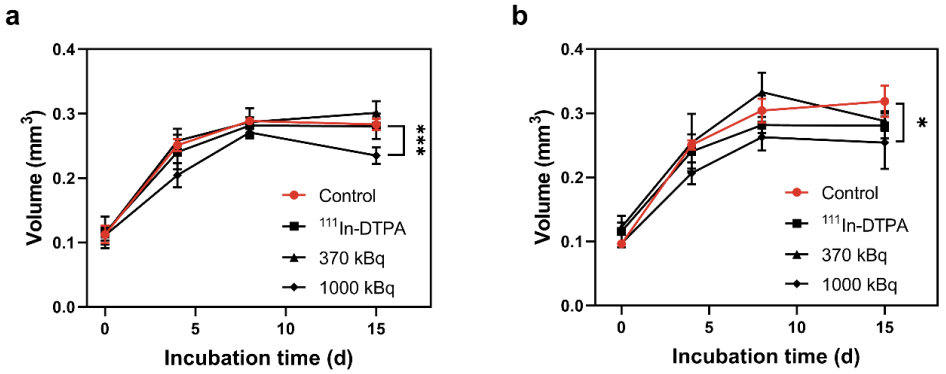

Figure 4.9. Volume change of U87 cell spheroids after the treatment of a) ^{111}In-DTPA-AuNPs and b) ^{111}In-DTPA-Ag_2TeNPs with 370 kBq or 1 MBq of ^{111}In, n=4. The volume change of 1 MBq ^{111}In-DTPA treated spheroids was also recorded for comparison. The specific activity of ^{111}In-DTPA-AuNPs and ^{111}In-DTPA-Ag_2TeNPs were 14.4 kBq/nM and 11.9 kBq/nM respectively.

In this work, two types of ^{111}In radiolabeled ultra-small nanoparticles were prepared and evaluated using *in vitro* models. Despite the similar size and surface charges of these two types of nanoparticles, their cell uptake was quite different. The cell internalization of nanoparticles is influenced by various factors including size, shape, surface charge and hydrophobicity.[40-43] Similar to the results from this work, some other nanoparticles with the same size but different cell uptake have been previously reported in the literature and

explained by the difference in other physical properties such as the hydrophobicity.[44-46] Further research is needed to better understand the cell uptake of these small nanoparticles.

Despite the modest cell uptake of ^{111}In-DTPA-AuNPs and ^{111}In-DTPA-Ag_2TeNPs (less than 1% of initially added ^{111}In activity), high cell killing efficiency has been achieved in 2D assays. This positive outcome might be attributed to the high nucleus accumulation of these 2-nm sized nanoparticles, leading to DNA damage caused by the AEs emitted by ^{111}In. Although cell nucleus has been considered as the prior target in Auger therapy, high cytotoxicity has also been achieved by targeting the AE emitters to the cell membrane.[4, 47-50] The AEs can form locally lipid rafts on the cell membrane, hereby leading to the formation of ROS or the initiation of DNA damage response (DDR) and eventually cell death. Thus, nanoparticles that had remained on the cell membrane could also have contributed to the high cell killing efficiency. Moreover, the self-radiosensitization effect from the interaction between γ particles or AEs and the nanoparticles might also account for the efficient tumor killing. Gold nanoparticles have been previously reported to act as radiosensitizers which can enhance the DNA damage caused by X-rays or electrons.[51-52] Although there has been no reports on the radiosensitizing effect of Ag_2TeNPs, the enhancement of external beam radiation therapy (EBRT) by silver nanoparticles, as well as composites with iron oxide, carbon and poly(lactic-co-glycolic acid) (PLGA) nanoparticles, have been reported in the literature.[53-56]

In term of the uptake in 3D tumor models, these non-targeted nanoparticles were likely to enter the spheroids through passive diffusion. Unlike in monolayered cells, nanoparticles can be retained in the interstitial space of the spheroids as previously reported, leading to very limited internalization of nanoparticles inside the cells of the spheroids.[57] Considering the fact that the uptake in U87 cell monolayers was low, it was likely that only a small fraction of the nanoparticles taken by the spheroids eventually reached the cell nucleus, which explains the weak growth inhibition effect observed in the spheroids. In future studies, more efforts need to be put on understanding the distribution of GSH-AuNPs and GSH-Ag_2TeNPs in cell spheroids, including their penetration depth and migration from the interstitial space into the cells.

To further improve the cytotoxicity to cancer cells, tumor-targeting moieties can be conjugated to the nanoparticles to achieve higher retention and therefore possibly higher cell uptake. In addition, the combination of Auger therapy with other treatment modalities such as DNA repair inhibitors might provide better treatment outcomes as well.

Conclusion

Two new types of potential radiopharmaceuticals for Auger therapy were developed in this work. High cell nucleus uptake has been achieved taking advantage of the small size of the nanoparticles, thus leading to high tumor killing efficiency *in vitro* even at modest cell uptake. With the modification of tumor-targeting moieties, the ^{111}In-DTPA-AuNPs and ^{111}In-DTPA-Ag_2TeNPs can be promising candidates for cancer theranostics.

References

[1] A. Dash, F. F. Knapp, R. A. M. Pillai, *Current Radiopharmaceuticals* **2013**, *6*, 152-180.
[2] A. Ku, V. J. Facca, Z. Cai, R. M. Reilly, *EJNMMI Radiopharm Chem* **2019**, *4*, 27.
[3] G. Pirovano, T. C. Wilson, T. Reiner, *Nucl Med Biol* **2021**, *96-97*, 50-53.
[4] S. Paillas, R. Ladjohounlou, C. Lozza, A. Pichard, V. Boudousq, et al., *Antioxidants & Redox Signaling* **2016**, *25*, 467-484.
[5] R. W. Howell, V. Narra, K. S. R. Sastry, D. V. J. R. r. Rao, *Radiat Res* **1993**, 134, 71-78.
[6] G. Mariani, L. Bruselli, T. Kuwert, E. E. Kim, A. Flotats, et al., *European Journal of Nuclear Medicine and Molecular Imaging* **2010**, *37*, 1959-1985.
[7] K. F. Eckerman, A. Endo, MIRD Radionuclide Data and Decay Schemes, *The Society of Nuclear Medicin*e, Reston (VA), **2007**.
[8] B. Cornelissen, M. Hu, K. McLarty, D. Costantini, R. M. Reilly, *Nuclear Medicine and Biology* **2007**, *34*, 37-46.
[9] B. Cornelissen, S. Darbar, V. Kersemans, D. Allen, N. Falzone, et al., *Nuclear Medicine and Biology* **2012**, *39*, 1142-1151.
[10] B. Cornelissen, A. Waller, C. Target, V. Kersemans, S. Smart, et al., *EJNMMI Research* **2012**, *2*, 9.
[11] C. Panosa, H. Fonge, M. Ferrer-Batalle, J. A. Menendez, A. Massaguer, et al., *Nucl Med Biol* **2015**, *42*, 931-938.
[12] A. Zereshkian, J. V. Leyton, Z. Cai, D. Bergstrom, M. Weinfeld, et al., *Nucl Med Biol* **2014**, *41*, 377-383.
[13] J. V. Leyton, M. Hu, C. Gao, P. V. Turner, J. E. Dick, et al., *J Nucl Med* **2011**, *52*, 1465-1473.
[14] C. Chan, H. Fonge, K. Lam, R. M. Reilly, *Nucl Med Biol* **2020**, *80-81*, 37-44.
[15] V. J. Facca, Z. Cai, N. E. K. Gopal, R. M. Reilly, *Mol Pharm* **2022**, *19*, 3652-3663.
[16] K. Vallis, R. Reilly, D. Scollard, P. Merante, A. Brade, et al., **2014**, *4*, 181-192.
[17] B. Pelaz, C. Alexiou, R. A. Alvarez-Puebla, F. Alves, A. M. Andrews, et al., *ACS Nano* **2017**, *11*, 2313-2381.
[18] M. J. Mitchell, M. M. Billingsley, R. M. Haley, M. E. Wechsler, N. A. Peppas, et al., *Nat Rev Drug Discov* **2021**, *20*, 101-124.
[19] M. Yu, J. Zheng, *ACS Nano* **2015**, *9*, 6655-6674.
[20] K. M. Tsoi, S. A. MacParland, X. Z. Ma, V. N. Spetzler, J. Echeverri, et al., *Nat Mater* **2016**, *15*, 1212-1221.
[21] B. Du, M. Yu, J. Zheng, *Nature Reviews Materials* **2018**, *3*, 358-374.
[22] S. Li, J. Wei, Q. Yao, X. Song, J. Xie, et al., *Chem Soc Rev* **2023**, *52*, 1672-1696.
[23] X. Jiang, B. Du, Y. Huang, J. Zheng, *Nano Today* **2018**, *21*, 106-125.
[24] X. Wang, X. Zhong, J. Li, Z. Liu, L. Cheng, *Chem Soc Rev* **2021**, *50*, 8669-8742.
[25] J. Liu, M. Yu, X. Ning, C. Zhou, S. Yang, et al., *Angew Chem Int Ed Engl* **2013**, *52*, 12572-12576.
[26] J. Liu, M. Yu, C. Zhou, S. Yang, X. Ning, et al., *J Am Chem Soc* **2013**, *135*, 4978-4981.
[27] J. C. Hsu, E. D. Cruz, K. C. Lau, M. Bouche, J. Kim, et al., *Chem Mater* **2019**, *31*, 7845-7854.
[28] L. M. Nieves, Y. C. Dong, D. N. Rosario-Berrios, K. Mossburg, J. C. Hsu, et al., *ACS Appl Mater Interfaces* **2022**, *14*, 34354-34364.
[29] C. Zhou, M. Long, Y. Qin, X. Sun, J. Zheng, *Angew Chem Int Ed Engl* **2011**, *50*, 3168-3172.

[30] F. Chen, S. Goel, R. Hernandez, S. A. Graves, S. Shi, et al., *Small* **2016**, *12*, 2775-2782.
[31] C. Zhou, G. Hao, P. Thomas, J. Liu, M. Yu, et al., *Angew Chem Int Ed Engl* **2012**, *51*, 10118-10122.
[32] M. Kodiha, Y. M. Wang, E. Hutter, D. Maysinger, U. Stochaj, *Theranostics* **2015**, *5*, 357-370.
[33] K. Huang, H. Ma, J. Liu, S. Huo, A. Kumar, et al., *ACS Nano* **2012**, *6*, 4483-4493.
[34] S. Huo, S. Jin, X. Ma, X. Xue, K. Yang, et al., *ACS Nano* **2014**, *8*, 5852-5862.
[35] Z. Cai, N. Chattopadhyay, K. Yang, Y. L. Kwon, S. Yook, et al., *Nucl Med Biol* **2016**, *43*, 818-826.
[36] L. Song, N. Falzone, K. A. Vallis, *International Journal of Radiation Biology* **2016**, *92*, 716-723.
[37] L. Song, S. Able, E. Johnson, K. A. Vallis, *Nanotheranostics* **2017**, *1*, 232-243.
[38] V. R. Patel, Y. J. J. o. a. p. t. Agrawal, *J Adv Pharm Technol Res* **2011**, *2*, 81.
[39] M. E. Katt, A. L. Placone, A. D. Wong, Z. S. Xu, P. C. Searson, *Front Bioeng Biotechnol* **2016**, *4*, 12.
[40] S. Behzadi, V. Serpooshan, W. Tao, M. A. Hamaly, M. Y. Alkawareek, et al., *Chemical Society Reviews* **2017**, *46*, 4218-4244.
[41] S. L. Zhang, H. J. Gao, G. Bao, *Acs Nano* **2015**, *9*, 8655-8671.
[42] F. Zhao, Y. Zhao, Y. Liu, X. Chang, C. Chen, et al., *Small* **2011**, *7*, 1322-1337.
[43] G. Sahay, D. Y. Alakhova, A. V. Kabanov, *J Control Release* **2010**, *145*, 182-195.
[44] W. Jiang, B. Y. S. Kim, J. T. Rutka, W. C. W. Chan, *Nature Nanotechnology* **2008**, *3*, 145-150.
[45] A. Verma, O. Uzun, Y. H. Hu, Y. Hu, H. S. Han, et al., *Nature Materials* **2008**, *7*, 588-595.
[46] X. Bai, S. Wang, X. Yan, H. Zhou, J. Zhan, et al., *ACS Nano* **2020**, *14*, 289-302.
[47] J. P. Pouget, L. Santoro, L. Raymond, N. Chouin, M. Bardiès, et al., *Radiation Research* **2008**, *170*, 192-200.
[48] L. Santoro, S. Boutaleb, V. Garambois, C. Bascoul-Mollevi, V. Boudousq, et al., *Journal of Nuclear Medicine* **2009**, *50*, 2033-2041.
[49] S. Paillas, V. Boudousq, B. Piron, N. Kersual, M. Bardiès, et al., *Nuclear Medicine and Biology* **2013**, *40*, 471-480.
[50] B. Piron, S. Paillas, V. Boudousq, A. Pèlegrin, C. Bascoul-Mollevi, et al., *Nuclear Medicine and Biology* **2014**, *41*, e75-e83.
[51] X. Jiang, B. Du, M. Yu, X. Jia, J. Zheng, *Journal of Innovative Optical Health Sciences* **2016**, *09*, 1642003.
[52] A. Pronschinske, P. Pedevilla, C. J. Murphy, E. A. Lewis, F. R. Lucci, et al., *Nature Materials* **2015**, *14*, 904-907.
[53] R. Xu, J. Ma, X. Sun, Z. Chen, X. Jiang, et al., *Cell Research* **2009**, *19*, 1031-1034.
[54] D. Zhao, X. Sun, J. Tong, J. Ma, X. Bu, et al., *Acta Biochimica et Biophysica Sinica* **2012**, *44*, 678-684.
[55] A. Kleinauskas, S. Rocha, S. Sahu, Y.-P. Sun, P. Juzenas, *Nanotechnology* **2013**, *24*, 325103.
[56] M. Tamborini, E. Locatelli, M. Rasile, I. Monaco, S. Rodighiero, et al., *ACS Nano* **2016**, *10*, 2509-2520.
[57] M. G. Roberts, V. J. Facca, R. Keunen, Q. Yu, R. M. Reilly, et al., *Biomacromolecules* **2022**, *23*, 3296-3307.
[58] A. Khorami-Moghadam, A. R. Jalilian, K. Yavari, B. Alirezapour, M. Mazidi, et al., *Radiochimca Acta* **2013**, *101*, 577-584.

Supplemental information

1. Calculation of the number of nanoparticles

The as-prepared GSH-AuNPs and GSH-Ag_2TeNPs were dissolved using aqua regia and 69% nitric acid respectively. The concentration of Au or Ag was then measured using ICP-MS (NexION® 2000, PerkinElmer). The volume of a single nanoparticle (**V**) was calculated by using the diameter (**d**) of the nanoparticles as determined by TEM.

$$V = \frac{\pi}{6} \times d^3$$

Knowing the density (**ρ**) of gold (19.3 g/cm^3) and silver telluride (8.3 g/cm^3), the mass of a single particle (**M**) was calculated to be 6.93×10^{-20} g/NP and 3.49×10^{-20} g/NP respectively.

$$M = V \times \rho$$

With the concentration of Au and Ag measured by ICP-MS (**c,** g/L), the number of the nanoparticles in **v** liters of dispersion was calculated by:

$$[NP]_{number} = \frac{c \times v}{M \times v}\ NPs/L$$

Then the nanoparticle concentration was converted to mole per liter after being divided by the Avogadro constant (N_{AV}):

$$[NP]_{molar} = \frac{[NP]_{number}}{N_{AV}}\ M$$

2. Radiolabeling of DTPA with ^{111}In

In a typical experiment, 5 MBq ^{111}In was added to 70 µl 0.2 M HEPES pH 7.0 buffer. 30 µl of 1 mM DTPA dissolved in 0.2 M HEPES pH 7.0 buffer was then added to the ^{111}In and reacted for 1 h at 37 °C. The radiolabeling efficiency was evaluated using iTLC and was always ~100% (n>5). The mobile phase was 10 wt% ammonium acetate: MeOH=1:1 (v/v).[58] ^{111}In-DTPA was developed along with the mobile phase while free $^{111}In^{3+}$ remained at the origin.

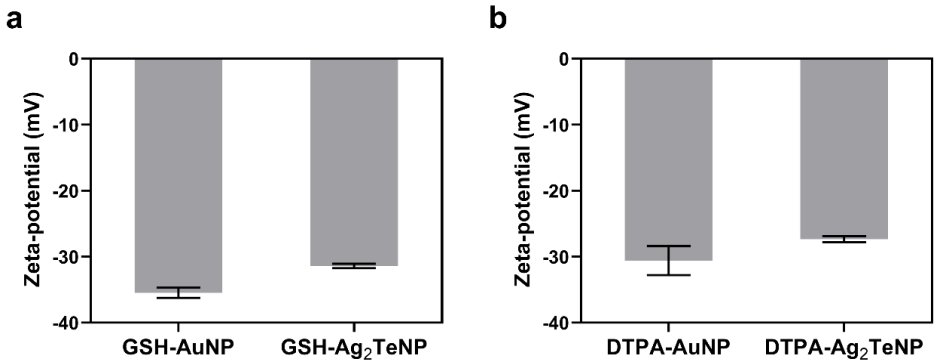

Figure S4.1. Zeta potential of different nanoparticles in PBS. a) GSH-AuNPs and GSH-Ag_2TeNPs, n=3; b) DTPA modified GSH-AuNPs and GSH-Ag_2TeNPs, n=3.

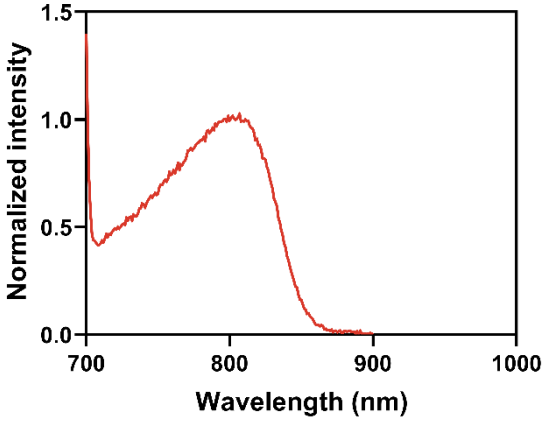

Figure S4.2. The fluorescence emission spectrum of GSH-AuNPs in PBS. A peak at 810 nm was measured when using an excitation wavelength of 340 nm.

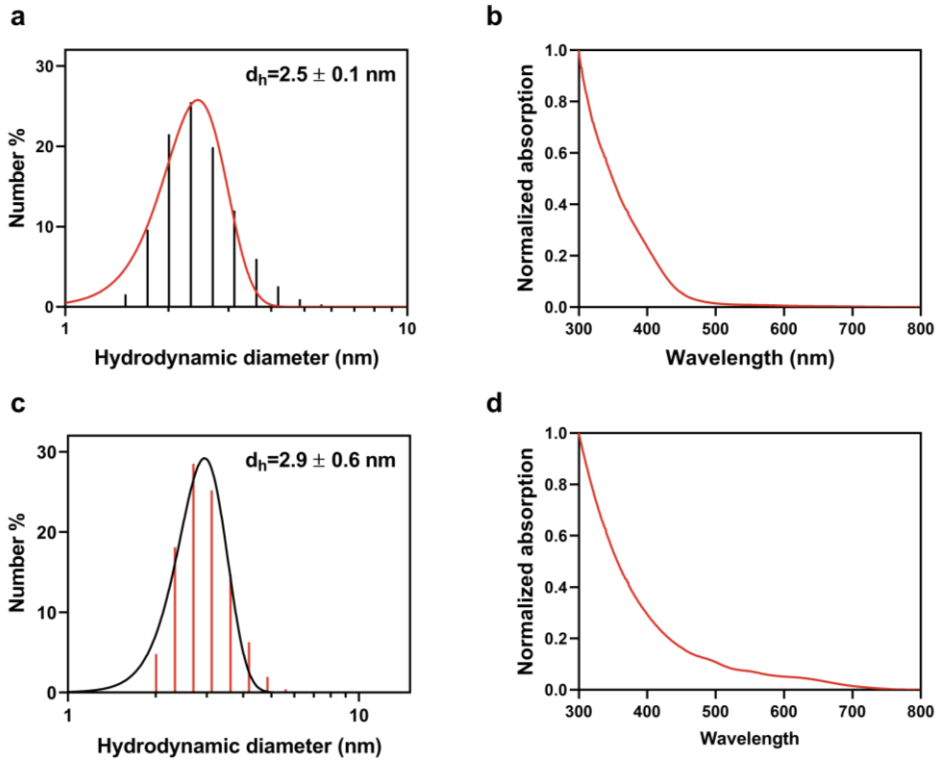

Figure S4.3. Number based hydrodynamic diameter of a) DTPA-AuNPs and c) DTPA-Ag_2TeNPs. Normalized UV-vis spectrum of b) DTPA-AuNPs and d) DTPA-Ag_2TeNPs. The nanoparticles were dispersed in PBS for the DLS and UV-vis measurements.

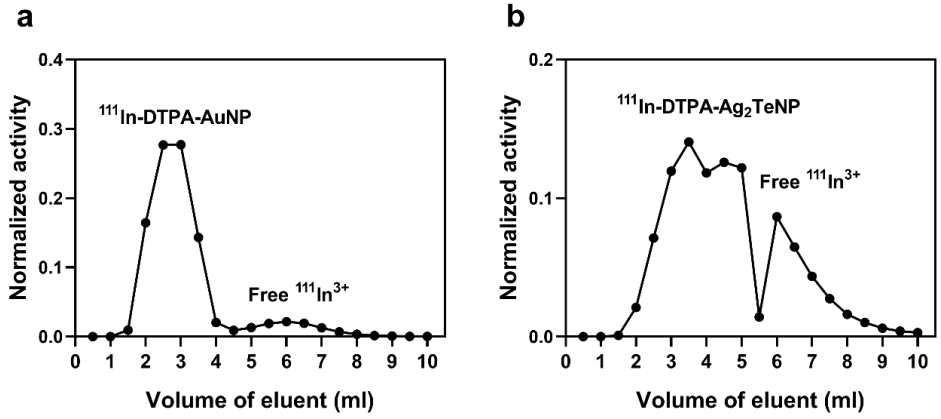

Figure S4.4. Typical elution profiles of a) ^{111}In-DTPA-AuNPs and b) ^{111}In-DTPA-Ag_2TeNPs in PD-10 columns using PBS as eluent. Fractions were collected every 500 µl. The counts of each fraction were measured with an automated gamma counter for 5 min to collect high enough counts.

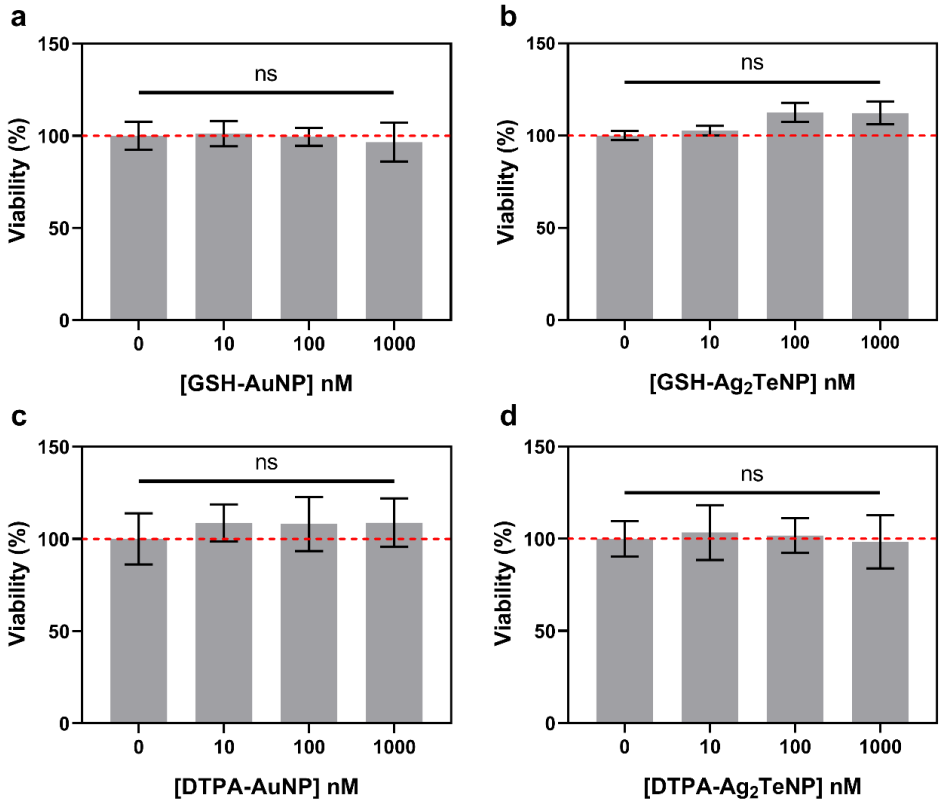

Figure S4.5. Viability assay of U87 cells after being incubated with non-radioactive a) GSH-AuNPs; b) GSH-Ag_2TeNPs; c) DTPA-AuNPs and d) DTPA-Ag_2TeNPs at nanoparticle concentrations of 0, 10, 100 and 1000 nM at 37 °C for 24 h, n=3.

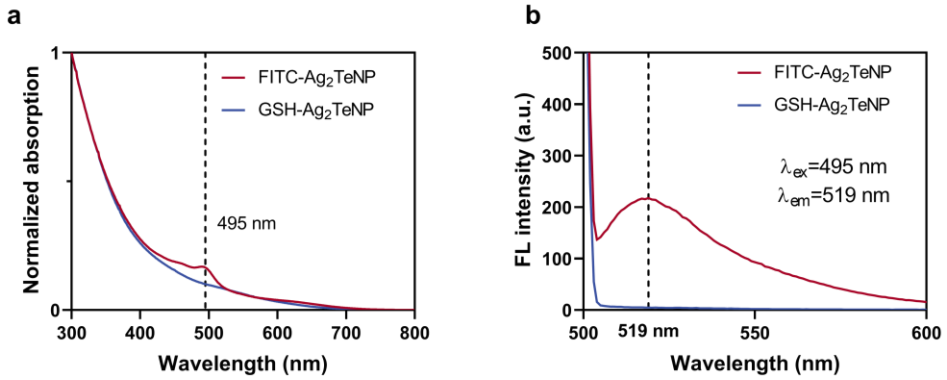

Figure S4.6. a) Absorption spectrum of FITC-Ag_2TeNPs and GSH-Ag_2TeNPs in PBS. A new peak at 495 nm was detected for the FITC-Ag_2TeNPs corresponding to the FITC absorption at 495 nm. b) Fluorescent emission spectrum of FITC-Ag_2TeNPs and GSH-Ag_2TeNPs in PBS using an excitation wavelength at 495 nm. The fluorescent signal was detected at 519 nm from the FITC-Ag_2TeNPs while the GSH-Ag_2TeNPs were non-fluorescent, suggesting the successful FITC linkage.

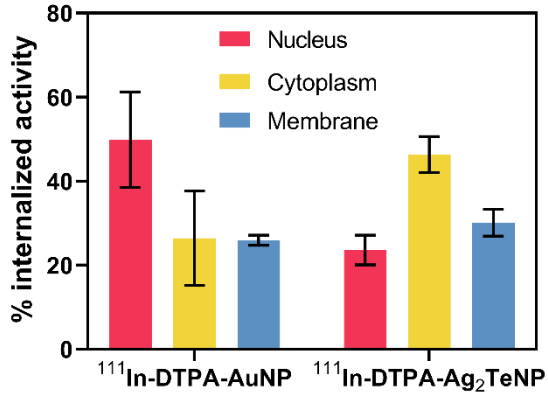

Figure S4.7. Subcellular distribution of internalized ^{111}In-DTPA-AuNPs and ^{111}In-Ag_2TeNPs in 2D U87 cells after 24 h incubation. The nanoparticle concentration was 100 nM for both types of nanoparticles, n=3.

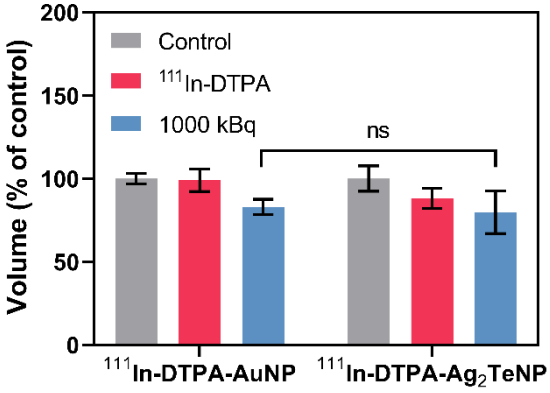

Figure S4.8. Normalized spheroid size on day 14 after the treatment with ^{111}In-DTPA-AuNPs, ^{111}In-DTPA-Ag_2TeNPs and ^{111}In-DTPA with 1 MBq ^{111}In, n=4.

5

Inorganic nanoparticles as carriers for the lead-212/bismuth-212 *in vivo* generator: a solution to the loss of bismuth-212 caused by internal conversion

Abstract

The lead-212/bismuth-212 (^{212}Pb/^{212}Bi) *in vivo* generator for alpha radionuclide therapy has gained a lot of interest in the past years. The alpha emitters in this decay chain (^{212}Bi and ^{212}Po) are all formed from β^- decay, relieving the safety concern regarding the recoil effect caused by alpha decay. However, approximately 36% ^{212}Bi (the daughter of ^{212}Pb) can still be released from conventional carriers due to internal conversion effects during the decay of ^{212}Pb. In this work, we investigated the potential of inorganic nanoparticles as carriers of ^{212}Pb/^{212}Bi *in vivo* generator to achieve high retention of ^{212}Bi. The radiolabeling of ^{212}Pb on CTAB/CTAC-Au@AuNPs, PEG-AuNPs, GSH-Ag_2TeNPs and PVP-PbSNDs was performed and evaluated in terms of radiolabeling efficiency and radiochemical stability of both ^{212}Pb and ^{212}Bi. In all cases, more than 85% of the overall radiochemical stability was achieved when being challenged with 1 mM EDTA solution for 24 hours. The improved ^{212}Bi retention was attributed to the high number of free electrons in the nanoparticles which can rapidly fill the electron vacancies created by internal conversion. These results illustrate that such inorganic nanoparticles might function as carriers of ^{212}Pb/^{212}Bi *in vivo* generator, which combined with other favorable properties such as fast renal clearance and the possibility to attach various targeting vectors on the surface, provide exciting opportunities for the design of new radiopharmaceuticals.

Key words: lead-212, bismuth-212, *in vivo* generator, internal conversion, inorganic nanoparticles

Introduction

Over the last 10 years, the interest on treating metastasized cancer with alpha (α) particle emitting radionuclides have been growing rapidly.[1-3] α particles can directly interact with the DNA molecules due to their high linear energy transfer (LET), leading to lethal damages such as double strand breaks (DSB).[4] Moreover, the DNA damage from α particles is not influenced by the oxygen level or cell cycle of the tumor cells.[5] Considering the high cytotoxicity to tumor cells as well as the short range (several cell diameters), α particles are very suitable for treating metastatic tumors while sparing the surrounding healthy tissues.[6] Despite the fact that there are approximately 100 α-emitting radionuclides, only a small number of those radionuclides have appropriate half-life time and good accessibility for clinical applications, such examples are radium-223 (^{223}Ra), actinium-225 (^{225}Ac), astatine-211 (^{211}At), bismuth-213 (^{213}Bi) and bismuth-212 (^{212}Bi).[7] In 2013, ^{223}Ra dichloride (Xofigo®, Bayer) was approved by the FDA for the treatment of bone metastasis and became the first commercially available α radiopharmaceutical.[8]

Bismuth-212 (^{212}Bi) has been applied in alpha radionuclide therapy in previous studies.[5, 9-11] However, the direct use of ^{212}Bi is limited by its short half-life time ($t_{1/2}$=60.5 min) which makes the preparation and shipment of ^{212}Bi radiopharmaceuticals difficult, and in addition limits the activity of ^{212}Bi that eventually reaches the tumor sites after being administrated to the patient.[12] Lead-212 (^{212}Pb) decays to ^{212}Bi with a half-life time of 10.6 h and can be used as an *in vivo* generator of ^{212}Bi to compensate for its fast decay (Figure 5.1).[13-14] Many preclinical studies on ^{212}Pb based radiopharmaceuticals have been reported in the literature for the treatment of breast cancer,[15-21] melanoma,[22-24] pancreatic cancer,[25-26] neuroendocrine cancer,[27-28] ovarian cancer[29] and brain metastases.[30] Moreover, the combination of ^{203}Pb ($t_{1/2}$=51.9 h, E_γ=279.2 keV, 80.94%) and ^{212}Pb has been explored for tumor theragnostic applications.[23, 31] In the term of clinical studies, results of the first phase I clinical trial of ^{212}Pb radiopharmaceutical was reported in 2014.[32-33] In this study, ^{212}Pb was attached to trastuzumab modified with 2-[4,7,10-tris(2-amino-2-oxoethyl)-1,4,7,10-tetrazacyclododec-1-yl]acetamide (TCMC) to target ovarian tumors. Minimal toxicity to healthy tissues has been observed from this study. Another phase I clinical trial has been initiated in 2018 using ^{212}Pb-octreotate (AlphaMedix™) which targets metastatic SSTR

expressing neuroendocrine tumors.[34] No dose-limiting toxicity has been found from this study either.

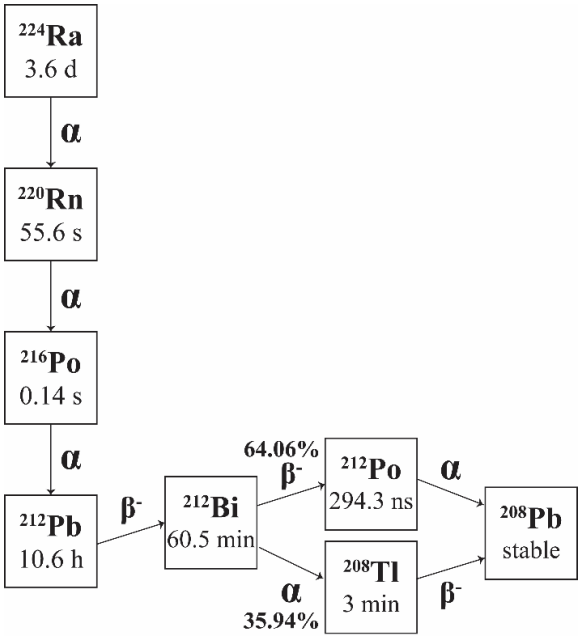

Figure 5.1. Decay scheme of ^{224}Ra. The decay data of all radionuclides is obtained from the Evaluated Nuclear Structure Data File (ENSDF, National Nuclear Data Center, USA).

In spite of the positive outcomes from these studies, it is not entirely clear if the release of ^{212}Bi from the targeting agents would cause any late toxicity. When ^{212}Pb decays to ^{212}Bi, the excitation energy can be released by the emission of γ photons but also via the ejection of an inner shell (K or L) electron (i.e. internal conversion), which leads to the creation of an electron vacancy. The electrons from outer shells will then transit to fill in this vacancy, resulting in the emission of characteristic X-rays or Auger electrons or both which results in the creation of more electron vacancies. A cascade of Auger electrons eventually leads to the loss of a high number of electrons from the ^{212}Bi atoms, making the $^{212}Bi^{n+}$ ions highly positive charged (n>3). The highly charged ^{212}Bi ions tend to attract electrons from the carrier molecules to reduce their oxidation number back to +3. The carriers can then also become positively charged due to the donation of electrons to the $^{212}Bi^{n+}$ ions. The repulsive force between the $^{212}Bi^{3+}$ ions and the positively charged carriers hereby lead to the release of $^{212}Bi^{3+}$ ions. According to the decay scheme of ^{212}Pb, the total internal conversion coefficient of the magnetic dipole (M1) transition from 238.6 keV level to the ground state is supposed

to be 0.84, implying that 45.6% of this transition is by internal convertion.[35] After multiplying with the branching ratio of this transition (82.5%), the overall probability of internal conversion during the decay of ^{212}Pb is calculated to be 37.6%. This result has been verified experimentally using ^{212}Pb/^{212}Bi-DOTA complex where 37% of ^{212}Bi was released from the DOTA complex.[36]

Considering the complex environment *in vivo*, the free $^{212}Bi^{3+}$ ions are not likely to be complexed again by the chelator molecules but will distribute in the body (mostly kidney), leading to undesired radiation burden.[37] In order to address this problem, a few studies have been carried out using nanomaterials as the carrier of ^{212}Pb. For instance, ^{212}Pb has been loaded inside fullerene (C60) nanoparticles. However, no improvement on the retention of the internally converted ^{212}Bi has been achieved.[38] In another work, ^{212}Pb was encapsulated in liposomes with a diameter of 120 nm and more than 90% retention of ^{212}Bi has been achieved.[39]

Our group has previously shown that the incorporation of radionuclides inside nanoparticles composed of high Z materials can diminish the loss of internally converted daughter radionuclides.[40] In this work, various inorganic nanoparticles were radiolabeled with ^{212}Pb including cetyltrimethylammonium bromide or cetrimonium chloride coated gold core-shell structured nanoparticles (CTAB/CTAC-Au@AuNP), polyethylene glycol coated gold nanoparticles (PEG-AuNP), glutathione coated silver telluride nanoparticles (GSH-Ag_2TeNP) and polyvinylpyrrolidone coated lead sulfide nanodots (PVP-PbSND). We report here the radiolabeling efficiency as well as the radiochemical stability of all these nanoparticles.

Methods and materials

1. Materials

The ^{224}Ra/^{212}Pb generator was purchased from Oak Ridge National Laboratory (ORNL, Oak Ridge, TN, USA). Silver nitrate, L-glutathione and polyvinylpyrrolidone (10 kDa) were ordered from Thermo Fisher Scientific (Landsmeer, the Netherlands). All other chemicals used in this study were obtained from Merck Sigma (Zwijndrecht, the Netherlands). All

chemicals were used as received without further purification. Milli-Q water was produced using an in-house Milli-Q system (Millipore) and used throughout this study.

2. Elution of $^{224}Ra/^{212}Pb$ generator

^{212}Pb was obtained by slowly eluting the $^{224}Ra/^{212}Pb$ generator with 500 µl 2 M HCl, followed by 250 µl water. The collected ^{212}Pb solution was evaporated on a hot plate until soft dryness. The residual was then redissolved in 500 µl 0.5 M sodium acetate (NaOAc) buffer (pH 6.0). The elution efficiency of ^{212}Pb was 87%~99% (n>5).

3. Synthesis of ^{212}Pb radiolabeled core-shell structured AuNPs

The synthesis of ^{212}Pb-CTAB/CTAC-Au@AuNPs was adapted from a published protocol with minor adjustment.[40-41] 0.1 ml 25 mM tetrachloroauric(III) acid ($HAuCl_4$), 50 kBq ^{212}Pb in 20 µl 0.5 M NaOAc buffer (pH 6.0), 4 ml 250 mM CTAB and 5.88 ml water was added to a glass vial and mixed for 10 min. 0.6 ml freshly prepared, ice-cold 10 mM sodium borohydride ($NaBH_4$) solution was added to the mixture under vigorous stirring. The color of the solution changed from yellow to dark brown rapidly. The obtained ^{212}Pb-AuNP seeds were left undisturbed at 27 °C for 1 hour before further reactions. To grow an extra layer of gold on top of the ^{212}Pb-AuNP seeds, 2 ml 200 mM CTAC, 1.5 ml 100 mM ascorbic acid (AA) and 1 ml ^{212}Pb-AuNP seed were added to a glass vial and mixed for 5 min at 27 °C. 2 ml 0.5 mM $HAuCl_4$ was then added in one-shot by a pipet. The reaction was continued at 27 °C for another 15 min. To remove free ^{212}Pb and other daughter radionuclides, 50 µl 10 mM ethylenediaminetetraacetic acid (EDTA) was added to the ^{212}Pb-CTAB/CTAC-Au@AuNPs and incubated for another 15 min. The ^{212}Pb-Au@AuNPs were then washed thrice using centrifuge filters (10 kDa MWCO, Amicon) at 4000 rpm for 20 min and redispersed in 1 mM EDTA.

4. Synthesis of ^{212}Pb radiolabeled PEG-AuNPs

The synthesis of ^{212}Pb-PEG-AuNPs was adapted from a published protocol with adjustments.[42] In a typical reaction, 188 µl 10 mM $HAuCl_4$ and 50 kBq ^{212}Pb in NaOAc buffer were added to 1.927 ml water. After being mixed at room temperature for 5 min, 400 µl 10 mM PEG350-SH was added dropwise and mixed for another 5 min. Then, 400 µl ice-cold 20 mM $NaBH_4$ was quickly added under vigorous stirring. The mixture was further stirred for 2 min and aged for 1 hour before the addition of 50 µl 10 mM EDTA to capture

free ^{212}Pb and other daughter radionuclides. The obtained ^{212}Pb-PEG-AuNPs were then washed thrice using a centrifuge filter (10 kDa MWCO) at 4000 rpm for 10 min and redispersed in 1 mM EDTA.

5. Synthesis of ^{212}Pb radiolabeled GSH-Ag_2TeNPs

The synthesis of ^{212}Pb-GSH-Ag_2TeNPs was adapted from a published protocol with minor adjustment.[43] In a typical reaction, 1.5 ml 30 mM silver nitrate ($AgNO_3$), 1.5 ml 15 mM sodium tellurite (Na_2TeO_3), 1.5 ml 90 mM L-glutathione (L-GSH) as well as 37 kBq ^{212}Pb in 20 µl NaOAc buffer were mixed in an ice bath. 0.5 ml hydrazine hydrate (50%-60%, N_2H_4) was quickly injected into the mixture and vigorously stirred for 5 min, followed by the addition of 50 µl 10 mM EDTA and further incubated for 10 min. The produced ^{212}Pb-GSH-Ag_2TeNPs were then washed thrice using centrifuge filters (10 kDa MWCO) at 4250 rpm for 20 min at 4 °C and redispersed in 1 mM EDTA.

6. Synthesis of ^{212}Pb radiolabeled PVP-PbSNDs

The synthesis of [^{212}Pb]-PVP-PbSNDs was adapted from a published protocol with adjustments.[44] Typically, 37 kBq ^{212}Pb (in 20 µl NaOAc buffer), 1 g polyvinylpyrrolidone (MW=10 kDa, PVP10k) and 10 ml 1 mM lead chloride ($PbCl_2$) were mixed in a glass vial at room temperature for 10 min. 10 µl 1 M sodium sulfide (Na_2S) was then added to this solution and mixed for 5 min at room temperature followed by heating in an oil bath at 90 °C for 15 min. The obtained [^{212}Pb]-PVP-PbSNDs were then cooled down to room temperature followed by the incubation with 50 µl 10 mM EDTA for 15 min, washed thrice using centrifuge filters (10 kDa MWCO) at 4200 rpm for 20 min and finally redispersed in 1 mM EDTA.

7. Determination of radiolabeling efficiency

The radiolabeling efficiency (RE) of the ^{212}Pb-CTAB/CTAC-Au@AuNPs was determined by measuring the counts of the nanoparticles and the counts of the washing fractions using an automated gamma counter (Wallac Wizard^2 2480, Perkin Elmer, n=3). The radiolabeling efficiency was calculated using the following equation: Counts(NPs)/[Counts(NPs)+ ∑Counts(wash)] × 100%. ^{212}Pb was measured by using the gamma emission at 238.6 keV while ^{212}Bi was measured by using the gamma emission at 723.3 keV. The radiolabeling efficiency of other ^{212}Pb radiolabeled nanoparticles was determined by iTLC before washing

the nanoparticles using centrifuge filters. (EtOH: 10 wt% NH_4OAc=1:1, n=3) The nanoparticles were retained at the origin of the iTLC strips while the $^{212}Pb/^{212}Bi$-EDTA complex moved along with the mobile phase.

8. Determination of radiochemical stability

The radiochemical stability (RCS) of the CTAB/CTAC-^{212}Pb-Au@AuNPs was determined by washing the nanoparticles using centrifuge filters (10 kDa) at 24 hours after purification. The RCS was calculated by comparing the counts remaining in the nanoparticle fraction and the counts in the washing solutions. (n=3) The 4 h or 24 h RCS of the other ^{212}Pb radiolabeled nanoparticles was measured by iTLC using the same mobile phase as described in the previous section. (n=3)

Results and discussion

CTAB/CTAC-Au@AuNPs as carriers for ^{212}Pb

In previous research (Chapter 2), we showed that the loss of daughter radionuclides due to internal conversion can be prevented if the mother radionuclides are incorporated in core-shell structured gold nanoparticles. We therefore first radiolabeled the same gold nanoparticles with ^{212}Pb. As shown in Figure 5.2, the radiolabeling efficiency of ^{212}Pb was found to be 93.9 ± 0.2%. Much higher radiolabeling efficiency was achieved when compared to ^{166}Dy (59.8 ± 0.2%) which might be explained by the fact that only trace amounts of $^{212}Pb^{2+}$ ions (4.6×10^{-6} nmol) were actually added while much more Dy^{3+} ions (166 nmol) were used in the case of ^{166}Dy. After challenging the purified ^{212}Pb-CTAB/CTAC-Au@AuNPs with 1 mM EDTA for 24 hours (two half-lives of ^{212}Pb), the retention of ^{212}Pb and ^{212}Bi was determined as shown in Figure 5.2. Similar to the results of $^{166}Dy/^{166}Ho$, high RCS was achieved for both the mother ^{212}Pb (98.5 ± 0.1%) and the daughter ^{212}Bi (87.5 ± 1.3%).

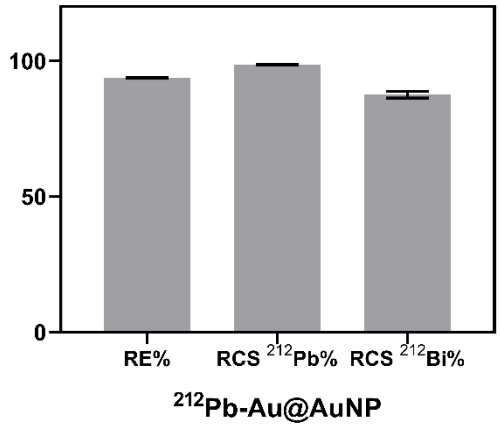

Figure 5.2. Radiolabeling efficiency (RE) of ^{212}Pb-CTAB/CTAC-Au@AuNPs and the corresponding radiochemical stability (RCS) of ^{212}Pb and ^{212}Bi after being challenged with 1 mM EDTA for 24 h, n=3.

PEG-AuNPs as carriers for ^{212}Pb

We also tested the radiolabeling efficiency of ^{212}Pb in gold nanoparticles coated by PEG molecules. Prior to the radiolabeling with ^{212}Pb, non-radioactive PEG-AuNPs were first prepared and characterized using transmission electron microscopy (TEM) and dynamic light scattering (DLS). As shown in Figure S5.1, the diameter of the PEG-AuNPs was found to be 3.0 ± 0.9 nm and the hydrodynamic diameter was measured to be 4.5 ± 0.9 nm. Considering the trace amount of doped $^{212}Pb^{2+}$ ions, the size distribution of the ^{212}Pb-PEG-AuNPs should be identical to that of the non-radioactive PEG-AuNPs. The ^{212}Pb radiolabeling on PEG-AuNPs was also achieved by the co-reduction of gold salts and $^{212}Pb^{2+}$ ions by $NaBH_4$ but resulted in a lower radiolabeling efficiency, i. e. 42.4 ± 3.4%. The RCS of the ^{212}Pb-PEG-AuNP was found to be 87.2 ± 10.4% after being challenged with 1 mM EDTA for 24 h, comparable to that of the ^{212}Pb-CTAB/CTAC-Au@AuNPs.

GSH-Ag_2TeNPs as carriers for ^{212}Pb

Next, we explored the possibility of loading ^{212}Pb on other types of nanoparticles. The first attempt was made with glutathione coated silver telluride nanoparticles (GSH-Ag_2TeNPs) which have been reported to be a very promising computed tomography (CT) contrast agent due to the strong X-ray attenuation and tiny size (~ 2 nm).[43] Considering the similar ionic radius between Ag^+ and Pb^{2+} ions, Pb^{2+} ions might be able to co-precipitate with the Ag^+ ions to form Pb doped GSH-Ag_2TeNPs. Moreover, lead telluride (PbTe) is also barely soluble in

water as Ag_2Te.[45] The co-precipitation of Pb and Ag was first tested with a non-radioactive Pb source. From Figure S5.2, it can be seen that the ^{nat}Pb-GSH-Ag_2TeNPs had a diameter of 2.1 ± 0.3 nm and a hydrodynamic diameter of 2.7 ± 0.6 nm when using an initial Pb to Ag ratio of 1 to 1000 (n/n) during synthesis. To predict the radiolabeling efficiency of ^{212}Pb, the conversion rate of $^{nat}Pb^{2+}$ and Ag^+ ions during the formation of nanoparticles was determined. With the ICP-OES measurements, a comparable conversion rate of about 70% was achieved for both Pb and Ag (Figure S5.3), probably due to the quenching of reaction at relatively early time point (5 min after addition of hydrazine). Higher conversion rate is likely to be achievable by extending the reaction time, but that also leads to increase in the size of the nanoparticles.[43] To maintain the renal clearable properties of the GSH-Ag_2TeNPs, we decided to proceed with the ^{212}Pb radiolabeling using a reaction time of 5 minutes, although the radiolabeling efficiency might not be optimal. According to this approach, the radiolabeling efficiency was determined to be 74.8 ± 3.6%, consistent with the results from the pilot study. After being challenged by 1 mM EDTA for 4 h or 24 h, the RCS of the ^{212}Pb-GSH-Ag_2TeNPs was quantified using iTLC. A nearly 100% RCS was achieved at 4 h. The 24 h RCS was also found to be high, i.e. 95.5 ± 6.2%.

PVP-PbSNDs as carriers for ^{212}Pb

Ultra-small copper-64 (^{64}Cu) radiolabeled copper(II) sulfide nanodots (CuSNDs) have shown great potential for positron emission tomography (PET) and photothermal therapy.[44] Due to the small hydrodynamic diameter (5 nm), the [^{64}Cu]CuSNDs were found to be renal clearable, thereby minimizing the radiation burden to the body. Considering the similar oxophilicity of Cu and Pb, we replaced Cu by Pb and prepared polyvinylpyrrolidone coated lead(II) sulfide nanodots (PVP-PbSNDs).[46] As shown in Figure S5.4, the PVP-PbSNDs have a small diameter of 2.8 ± 0.6 nm as well as a hydrodynamic diameter of 4.4 ± 0.8 nm in water. The radiolabeling of PVP-PbSNDs was achieved by mixing $^{212}Pb(OAC)_2$ with $PbCl_2$ as the reactant. A nearly 100% radiolabeling efficiency was achieved as well as high RCS after 4 h and 24 h incubation in 1 mM EDTA (94.2 ± 1.7% and 92.7 ± 5.1% respectively). Attempt to increase the specific activity of the [^{212}Pb]-PVP-PbSNDs was carried out by scaling down the reaction by 50% but using the same activity of ^{212}Pb. Surprisingly, the radiolabeling efficiency in the scaled down reaction decreased to 73.8 ± 7.7% while the 4 h RCS remained higher than 90%.

Table 5.1. An overview of the radiolabeling efficiency and radiochemical stability of the ^{212}Pb radiolabeled nanoparticles produced in this work.

	Radiolabeling efficiency (%)	**4 h radiochemical stability (%)**	**24 h radiochemical stability (%)**
CTAB/CTAC-Au@AuNPs	93.9 ± 0.2	-	98.5 ± 0.1 (^{212}Pb)[a] 87.5 ± 1.3 (^{212}Bi)
PEG-AuNPs	42.4 ± 3.4	-	87.2 ± 10.4[b]
GSH-Ag_2TeNPs	74.8 ± 3.6	103.4 ± 5.0	95.5 ± 6.2
PVP-PbSNDs (scaled donw)	73.8 ± 7.7	89.9 ± 7.1	-
PVP-PbSNDs	99.1 ± 1.0	94.2 ± 1.7	92.7 ± 5.1

[a] The radiochemical stability of ^{212}Pb and ^{212}Bi on CTAB/CTAC-Au@AuNPs were determined separately by measuring the gamma emission at 238.6 keV and 723.3 keV for ^{212}Pb and ^{212}Bi respectively.
[b] The radiochemical stability of ^{212}Pb radiolabeled PEG-AuNPs, GSH-Ag_2TeNPs and PVP-PbSNDs was determined as the sum of ^{212}Pb and ^{212}Bi using iTLC.

Discussion

One of the main problems hindering the clinical translation of nanomaterials is the high mononuclear phagocyte system (MPS) uptake which might cause long term toxicity, especially when considering those radiolabeled nanoparticles.[47-48] One possible solution is to tune the physical properties of the nanoparticles to enable renal clearance. Renal clearable nanoparticles can be rapidly excreted from the body within hours, thus reducing the concern of toxicity to healthy tissues.[49-50] In this work, we explored the radiolabeling of ^{212}Pb on various nanoparticles via co-reduction or co-precipitation methods. Specifically, the PEG-AuNPs, GSH-Ag_2TeNPs and PVP-PbSNDs are likely to be renal clearable due to their small

hydrodynamic diameters (<5.5 nm).[51] The ^{212}Pb radiolabeling efficiency of the tested nanoparticles varied from less than 50% to nearly 100%, mainly depending on the host and surface coating materials of the nanoparticles (Table 5.1).

In terms of the retention of ^{212}Pb and ^{212}Bi, high RCS was achieved for all tested nanoparticles even after being challenged by EDTA for 24 hours (Table 5.1). As the dissociated $^{212}Pb^{2+}$ and $^{212}Bi^{3+}$ ions are not likely to be re-absorbed by the nanoparticles, all free $^{212}Pb^{2+}$ and ^{212}Bi should be well separated from the nanoparticles either via centrifugation or iTLC. Considering the high RCS of the ^{212}Pb radiolabeled nanoparticles prepared in this work, it seems that the loss of internally converted ^{212}Bi was prevented by doping ^{212}Pb during the formation of the nanoparticles. As discussed in Chapter 2, the incorporation of the mother nuclides inside gold nanoparticles provides a great number of free electrons to quickly fill the electron vacancies created by the internal conversion effects. Thus, the daughter nuclides could be well retained in the gold nanoparticles. This hypothesis was further verified in this work by the high RCS of ^{212}Bi in the CTAB/CTAC-Au@AuNPs and PEG-AuNPs. Besides gold nanoparticles, two types of metal chalcogenide nanoparticles were also investigated as the carrier of ^{212}Pb/^{212}Bi *in vivo* generator. The $^{212}Pb^{2+}$ ions were co-precipitated along with the host materials (Ag or ^{nat}Pb) during the synthesis. The high RCS (>90%) achieved from the ^{212}Pb-GSH-Ag_2TeNPs and [^{212}Pb]-PVP-PbSNDs indicated the strong retention of ^{212}Pb and the internally converted ^{212}Bi. We hypothesized that the free electrons from the surrounding Ag or ^{nat}Pb atoms might also rapidly migrate to the $^{212}Bi^{n+}$ (n>3) ions, compensating the loss of Auger electrons thus avoiding the ejection of ^{212}Bi from the nanoparticles.

Despite the promising radiolabeling efficiency and high RCS, the specific activity of the obtained ^{212}Pb radiolabeled nanoparticles was too low for further biological studies. The next step of this research should focus on radiolabeling using higher activity of ^{212}Pb (in MBq) to check if the high radiolabeling efficiency and RCS can be maintained. The RCS of each nanoparticle should also be evaluated when dispersed in physiological solutions (e.g. PBS buffer and blood serum). Furthermore, the ^{212}Pb radiolabeled nanoparticles should be functionalized with tumor targeting moieties to enhance tumor uptake and good tumor killing efficiency.

Conclusion

In conclusion, four different types of inorganic nanoparticles were radiolabeled with ^{212}Pb using chelator-free approaches with high RCS for both ^{212}Pb and ^{212}Bi. The retention of internally converted ^{212}Bi is likely due to the high number of free electrons in these nanoparticles. However, the current radiolabeling methods still need to be improved to increase the specific activity of the products. Further biological studies will demonstrate the potential of these ^{212}Pb radiolabeled nanoparticles in cancer treatment.

References

[1] K. E. Baidoo, K. Yong, M. W. Brechbiel, *Clinical Cancer Research* **2013**, *19*, 530-537.
[2] G. Sgouros, L. Bodei, M. R. McDevitt, J. R. Nedrow, *Nat Rev Drug Discov* **2020**, *19*, 589-608.
[3] H. Jadvar, P. M. Colletti, *European Journal of Nuclear Medicine and Molecular Imaging* **2021**, *49*, 47-53.
[4] J. P. Pouget, S. J. Mather, *Eur J Nucl Med* **2001**, *28*, 541-561.
[5] M. R. Zalutsky, O. R. Pozzi, *Q J Nucl Med Mol Imaging* **2004**, *48*, 289-296.
[6] G. Sgouros, J. C. Roeske, M. R. McDevitt, S. Palm, B. J. Allen, et al., *J Nucl Med* **2010**, *51*, 311-328.
[7] T. I. Kostelnik, C. Orvig, *Chem Rev* **2019**, *119*, 902-956.
[8] C. Parker, S. Nilsson, D. Heinrich, S. I. Helle, J. M. O'Sullivan, et al., *N Engl J Med* **2013**, *369*, 213-223.
[9] M. G. Ferrier, V. Radchenko, D. S. Wilbur, *Radiochim Acta* **2019**, *107*, 1065-1085.
[10] C. L. Ruegg, W. T. Anderson-Berg, M. W. Brechbiel, S. Mirzadeh, O. A. Gansow, et al., *Cancer Res* **1990**, *50*, 4221-4226.
[11] R. P. Junghans, D. Dobbs, M. W. Brechbiel, S. Mirzadeh, A. A. Raubitschek, et al., *Cancer Res* **1993**, *53*, 5683-5689.
[12] N. K. Tafreshi, M. L. Doligalski, C. J. Tichacek, D. N. Pandya, M. M. Budzevich, et al., *Molecules* **2019**, *24*.
[13] D. E. Milenic, K. Garmestani, E. D. Brady, P. S. Albert, A. Abdulla, et al., *Clinical Cancer Research* **2007**, *13*, 1926-1935.
[14] K. E. Baidoo, D. E. Milenic, M. W. Brechbiel, *Nucl Med Biol* **2013**, *40*, 592-599.
[15] D. E. Milenic, K. Garmestani, E. D. Brady, P. S. Albert, D. Ma, et al., *Cancer Biotherapy and Radiopharmaceuticals* **2005**, *20*, 557-568.
[16] V. Boudousq, L. Bobyk, M. Busson, V. Garambois, M. Jarlier, et al., *PLoS One* **2013**, *8*, e69613.
[17] K. J. Yong, D. E. Milenic, K. E. Baidoo, Y. S. Kim, M. W. Brechbiel, *Cancer Med* **2013**, *2*, 646-653.
[18] D. E. Milenic, K. E. Baidoo, Y.-S. Kim, M. W. Brechbiel, *mAbs* **2015**, *7*, 255-264.
[19] B. B. Kasten, M. T. Azure, T. R. Schoeb, D. R. Fisher, K. R. Zinn, *Nucl Med Biol* **2016**, *43*, 391-396.
[20] B. B. Kasten, P. G. Oliver, H. Kim, J. Fan, S. Ferrone, et al., *Int J Mol Sci* **2018**, *19*.
[21] I. Liatsou, J. Yu, R. Bastiaannet, Z. Li, R. F. Hobbs, et al., *International Journal of Radiation Biology* **2022**, *98*, 1452-1461.
[22] Y. Miao, M. Hylarides, D. R. Fisher, T. Shelton, H. Moore, et al., *Clinical Cancer Research* **2005**, *11*, 5616-5621.
[23] Y. Miao, S. D. Figueroa, D. R. Fisher, H. A. Moore, R. F. Testa, et al., *J Nucl Med* **2008**, *49*, 823-829.
[24] M. Li, D. Liu, D. Lee, Y. Cheng, N. J. Baumhover, et al., *Cancers (Basel)* **2021**, *13*.
[25] B. B. Kasten, A. Gangrade, H. Kim, J. Fan, S. Ferrone, et al., *Nucl Med Biol* **2018**, *58*, 67-73.
[26] D. Bauer, L. M. Carter, M. I. Atmane, R. De Gregorio, A. Michel, et al., *J Nucl Med* **2023**.
[27] T. A. R. Stallons, A. Saidi, I. Tworowska, E. S. Delpassand, J. J. Torgue, *Molecular Cancer Therapeutics* **2019**, *18*, 1012-1021.

[28] D. Chapeau, S. Koustoulidou, M. Handula, S. Beekman, C. de Ridder, et al., *Pharmaceuticals (Basel)* **2023**, *16*.
[29] B. B. Kasten, R. C. Arend, A. A. Katre, H. Kim, J. Fan, et al., *Nucl Med Biol* **2017**, *47*, 23-30.
[30] A. Corroyer-Dulmont, S. Valable, N. Falzone, A. M. Frelin-Labalme, O. Tietz, et al., *Neuro Oncol* **2020**, *22*, 357-368.
[31] M. Li, N. J. Baumhover, D. Liu, B. S. Cagle, F. Boschetti, et al., *Pharmaceutics* **2023**, *15*.
[32] R. F. Meredith, J. Torgue, M. T. Azure, S. Shen, S. Saddekni, et al., *Cancer Biother Radiopharm* **2014**, *29*, 12-17.
[33] R. Meredith, J. Torgue, S. Shen, D. R. Fisher, E. Banaga, et al., *J Nucl Med* **2014**, *55*, 1636-1642.
[34] S. D. Ebrahim, T. Izabela, E. Rouzbeh, T. Julien, H. Jason, et al., *Journal of Nuclear Medicine* **2022**, *63*, 1326.
[35] F. Rösel, H. M. Fries, K. Alder, H. C. Pauli, *Atomic Data and Nuclear Data Tables* **1978**, *21*, 91-289.
[36] S. Mirzadeh, K. Kumar, O. A. Gansow, **1993**, *60*, 1-10.
[37] D. Beninson, H. Dunster, W. Jacobi, H. Jammet, J. Liniecki, et al., *Annals of the ICRP* **1980**, 67.
[38] M. D. Diener, J. M. Alford, S. J. Kennel, S. Mirzadeh, *Journal of the American Chemical Society* **2007**, *129*, 5131-5138.
[39] G. Henriksen, B. W. Schoultz, P. Hoff, R. H. Larsen, **2003**, *91*, 109-114.
[40] R. Wang, B. Ponsard, H. Wolterbeek, A. Denkova, *EJNMMI Radiopharmacy and Chemistry* **2022**, *7*, 16.
[41] Y. Zheng, X. Zhong, Z. Li, Y. Xia, *Particle & Particle Systems Characterization* **2013**, *31*, 266-273.
[42] Y. Zhao, D. Sultan, L. Detering, H. Luehmann, Y. Liu, *Nanoscale* **2014**, *6*, 13501-13509.
[43] L. M. Nieves, Y. C. Dong, D. N. Rosario-Berrios, K. Mossburg, J. C. Hsu, et al., *ACS Appl Mater Interfaces* **2022**, *14*, 34354-34364.
[44] M. Zhou, J. Li, S. Liang, A. K. Sood, D. Liang, et al., *ACS Nano* **2015**, *9*, 7085-7096.
[45] J. He, M. G. Kanatzidis, V. P. Dravid, *Materials Today* **2013**, *16*, 166-176.
[46] K. P. Kepp, *Inorg Chem* **2016**, *55*, 9461-9470.
[47] Q. Dai, S. Wilhelm, D. Ding, A. M. Syed, S. Sindhwani, et al., *ACS Nano* **2018**, *12*, 8423-8435.
[48] K. M. Tsoi, S. A. MacParland, X. Z. Ma, V. N. Spetzler, J. Echeverri, et al., *Nat Mater* **2016**, *15*, 1212-1221.
[49] M. Yu, J. Zheng, *ACS Nano* **2015**, *9*, 6655-6674.
[50] B. J. Du, M. X. Yu, J. Zheng, *Nat Rev Mater* **2018**, *3*, 358-374.
[51] H. S. Choi, W. Liu, P. Misra, E. Tanaka, J. P. Zimmer, et al., *Nat Biotechnol* **2007**, *25*, 1165-1170.

Supplemental information

1. Synthesis of PEG-AuNPs

In a typical reaction, 188 µl 10 mM $HAuCl_4$ and 1.927 ml water were mixed at room temperature for 5 min, followed by the dropwise addition of 400 µl 10 mM PEG350-SH. The obtained solution was mixed for another 5 min at room temperature. Then, 400 µl ice-cold 20 mM $NaBH_4$ was quickly added under vigorous stirring. The mixture was stirred for 2 min and aged for 1 hour to allow the decomposition of excess $NaBH_4$. The obtained PEG-AuNPs were washed thrice using centrifuge filters (10 kDa MWCO) at 4000 rpm for 10 min and redispersed in water.

2. Synthesis of ^{nat}Pb-GSH-Ag_2TeNPs

In a typical reaction, 1.5 ml 30 mM silver nitrate ($AgNO_3$), 1.5 ml 15 mM sodium tellurite (Na_2TeO_3), 1.5 ml 90 mM L-glutathione (L-GSH) and 4.5 µl 10 mM $Pb(OAC)_2$ were mixed in an ice bath. 0.5 ml hydrazine hydrate (50%-60%, N_2H_4) was quickly injected into the mixture and vigorously stirred for 5 min. 50 µl 10 mM EDTA was added to the as-prepared ^{nat}Pb-GSH-Ag_2TeNPs for 15 min. The ^{nat}Pb-GSH-Ag_2TeNPs were washed thrice using centrifuge filters (10 kDa MWCO) at 4250 rpm for 20 min at 4 ℃ and redispersed in water.

3. Synthesis of PVP-PbSNDs

Typically, 1 g polyvinylpyrrolidone (MW=10 kDa, PVP10k) was first dissolved in 10 ml 1 mM lead chloride ($PbCl_2$) in a glass vial at room temperature. 10 µl 1 M sodium sulfide (Na_2S) was then added to this solution, mixed for 5 min at room temperature and heated in an oil bath at 90 ℃ for another 15 min. The obtained PVP-PbSNDs were cooled down to room temperature and washed thrice using centrifuge filters (10 kDa MWCO) at 4200 rpm for 20 min and finally redispersed in water.

4. Characterizations

The shape and size of the non-radioactive nanoparticles were imaged by a 120 kV JEM-1400 Plus transmission electron microscope (TEM, JEOL). A zeta-sizer (nano-ZS, Malvern) was used to determine the hydrodynamic diameter of the nanoparticles. The conversion rate of Pb and Ag from the ^{nat}Pb-GSH-Ag_2TeNPs were determined using ICP-OES (Optima 8000, Perkin Elmer) measurements after destructing the nanoparticles with concentrated nitric acid.

The measured concentrations of Pb and Ag were compared with the initially added Pb and Ag to calculate the conversion rates.

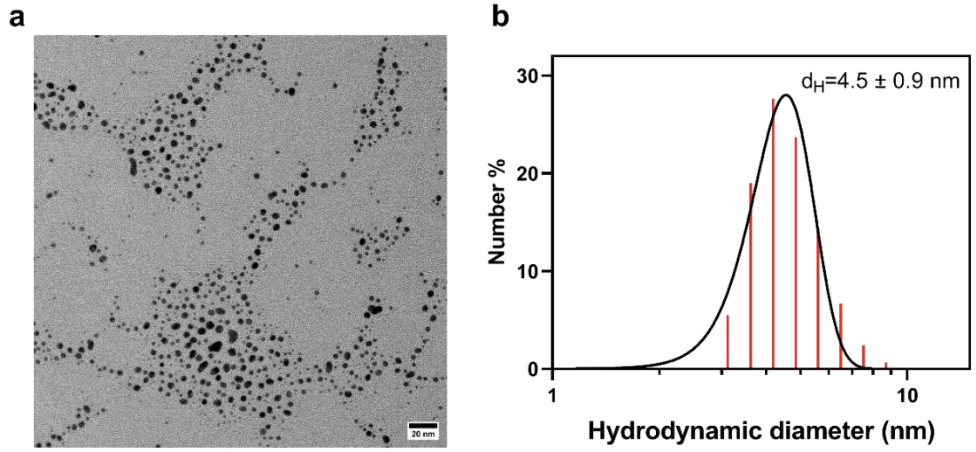

Figure S5.1. Characterization of non-radioactive Pb doped PEG-AuNPs. a) TEM images, scale bar=20 nm; b) number based hydrodynamic diameter measured by DLS (solvent: water). According to the TEM images, the Pb doped PEG-AuNPs had semi-spherical shape and a diameter of 3.0 ± 0.9 nm (n>300). In water, the number weighted hydrodynamic diameter was determined to be 4.5 ± 0.9 nm.

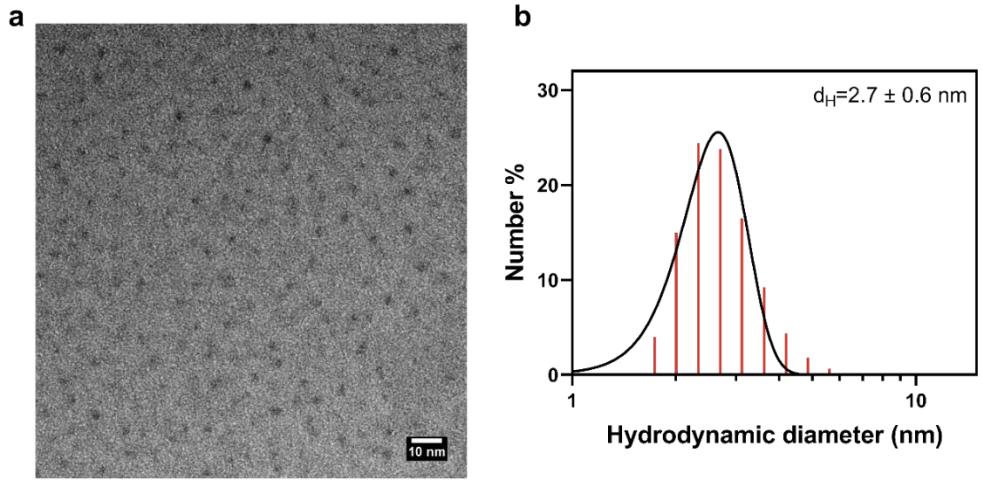

Figure S5.2. Characterization of non-radioactive Pb doped GSH-Ag_2TeNPs. a) TEM images, scale bar=10 nm; b) number based hydrodynamic diameter measured by DLS (solvent: PBS buffer, pH 7.4). According to the TEM images, the Pb doped GSH-Ag_2TeNPs had a semi-spherical shape and a diameter of 2.1 ± 0.3 nm (n>300). In PBS buffer, the number weighted hydrodynamic diameter was measured to be 2.7 ± 0.6 nm.

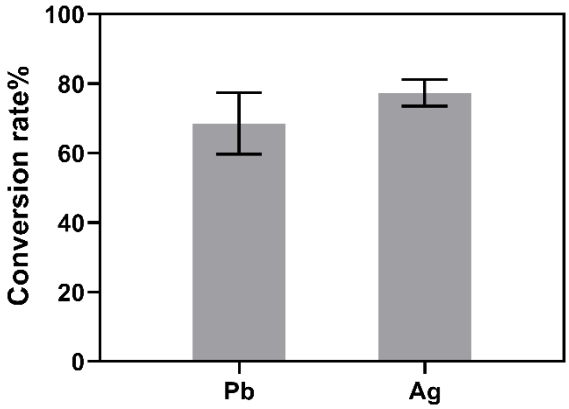

Figure S5.3. The conversion rate of Pb and Ag during the formation of non-radioactive Pb-GSH-Ag_2TeNPs when using an initial feeding ratio of Pb:Ag=1:1000 (n/n), n=3.

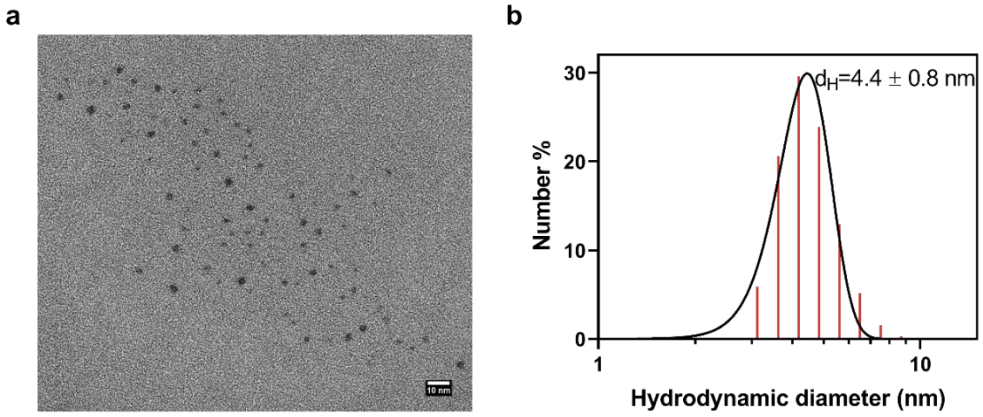

Figure S5.4. Characterization of non-radioactive PVP-PbSNDs. a) TEM images, scale bar=10 nm; b) number based hydrodynamic diameter measured by DLS (solvent: water). According to the TEM images, the PVP-PbSNDs had a semi-spherical shape and a diameter of 2.8 ± 0.6 nm (n>300). In water, the number hydrodynamic diameter was measured to be 4.4 ± 0.8 nm in water.

General conclusions and future perspectives

6

The research described in this thesis focused on the development of nanoparticle-based radiopharmaceuticals for cancer treatment. The radiolabeling of a few selected nanoparticles with different types of therapeutic radionuclides, including α emitters (^{212}Pb/^{212}Bi), β$^-$ emitters (^{166}Dy/^{166}Ho) and Auger electron emitters (^{111}In and ^{125}I) was successfully developed. The chemo-physical properties, radiochemical properties as well as the *in vitro* anti-tumor efficacy of these radiolabeled nanoparticles were systematically investigated in this thesis.

Core-shell structured gold nanoparticles were radiolabeled with ^{166}Dy (Chapter 2) and ^{212}Pb (Chapter 5) via co-reduction of the radiometallic ions with gold salts, which is referred to as radionuclide doping. The radiolabeling efficiency was found to be 59.8 ± 0.2% and 93.9 ± 0.2% for ^{166}Dy and ^{212}Pb respectively. The higher radiolabeling efficiency of ^{212}Pb was likely to originate from its high specific activity, meaning that only trace amount of $^{212}Pb^{2+}$ ions were actually added for reaction. More than 95% of ^{166}Dy and ^{166}Ho was retained on the nanoparticles even after 72 h DTPA challenge. In case of the ^{212}Pb radiolabeled gold nanoparticles, the retention of ^{212}Pb and ^{212}Bi after 24 h EDTA challenge was determined to be 98.5 ± 0.1% and 87.5 ± 1.3% respectively. Therefore, we came to a conclusion that the loss of daughter radionuclides due to internal conversion can be avoided by incorporating the mother nuclides in core-shell structured gold nanoparticles. The high number of free electrons of gold might account for the high retention of these internally converted daughter nuclides. Furthermore, three other types of metallic or metal-chalcogenide nanoparticles were radiolabeled with ^{212}Pb in Chapter 5, once again achieving minimum loss of ^{212}Pb and ^{212}Bi during 24 h EDTA challenge. However, the work reported in these chapters is still in an early stage and has certain limits. First, the exact mechanism of how the internally converted radionuclides are retained in these nanoparticles is not fully understood. In addition, the retention of the internally converted radionuclides still has to be verified in physiological solvents (e.g. PBS and serum) using higher activity of ^{166}Dy and ^{212}Pb.

In Chapter 3 and 4, ultra-small nanoparticles with sub-2 nm core size and sub-5.5 nm hydrodynamic diameter were radiolabeled with the Auger electron (AE) emitters ^{125}I and ^{111}In. Under the most optimal conditions, 14.4%, 49.8% and 23.6% of the internalized ^{125}I-PEG-AuNPs, ^{111}In-DTPA-AuNPs and ^{111}In-DTPA-Ag_2TeNPs respectively, were found in the cell nucleus of U87 cells. Due to the efficient delivery of AE emitters to the cell nucleus

as well as the self-radiosensitizing effect of the nanoparticles, high tumor cell killing efficiency were achieved in 2D U87 cells. However, all the tested nanoparticles had modest cell uptake, limiting their tumor killing efficacy in the 3D U87 spheroids. In future work, the nanoparticles have to be functionalized with tumor targeting moieties for higher uptake in the tumor cells while maintaining their small hydrodynamic diameter. In this sense, small molecular targeting agents such as PSMA and FAP inhibitors are preferred.[1-2] In addition, the results from the nucleus fractionation assay have to be verified with western blot assays and static or dynamic fluorescence imaging. As the tumor cell killing efficiency was only determined on the cell level in this work, more biological assays such as DNA double strand break staining and western blot are recommended for future work to better quantify the induction of DNA damage and to understand the mechanism of cell death caused by these AE emitting nanoparticles. Radiation dose calculations of the AE emitters can be performed using various models such as MCNP6 and MIRDCell as previously reported in the literature.[3-4] However, the radiosensitization effect of the nanoparticles might be challenging to be included in current models, requiring more information on the interaction between the primary electrons and the nanoparticles.

In conclusion, the application of nanoparticles especially those with small sizes in radionuclide therapy was found to be very beneficial for the improved radiochemical stability against nuclear events such as internal conversion as well as the delivery of AE emitters to the cell nucleus for maximum DNA damage. Extra benefits such as the fast body clearance via the urinary system and the possibility of being tracked by CT, PET, SPECT or fluorescence imaging are also attractive but need to be proved in animal models. Besides the AE emitters radiolabeled nanoparticles reported in this thesis, more combinations should be evaluated in the future. For example, the AE emitting Pt radionuclides (^{191}Pt, ^{193m}Pt and ^{195m}Pt) can be built inside the sub-2 nm GSH-PtNPs while ^{197}Hg or ^{99m}Tc can be loaded on the surface of PEG-AuNPs. This type of research will provide more possibility for Auger therapy, thus leading to more chances for clinical translation.

Reference:

[1] A. E. Machulkin, Y. A. Ivanenkov, A. V. Aladinskaya, M. S. Veselov, V. A. Aladinskiy, et al., *J Drug Target* **2016**, *24*, 679-693.
[2] P. Windisch, D. R. Zwahlen, F. L. Giesel, E. Scholz, P. Lugenbiel, et al., *Ejnmmi Res* **2021**, *11*.
[3] P. Lai, Z. L. Cai, J. P. Pignol, E. Lechtman, S. Mashouf, et al., *Phys Med Biol* **2017**, *62*, 8581-8599.
[4] Z. L. Cai, N. Al-saden, C. J. Georgiou, R. M. Reilly, *International Journal of Radiation Biology* **2023**, *99*, 53-63.

Summary

Radionuclide therapy is an important cancer treatment modality that makes use of the local irradiation from radionuclides at the tumor sites. Radiopharmaceuticals are normally composed of three components: radionuclide, carrier and tumor targeting agent. In terms of the radionuclide carriers, macrocyclic and acyclic chelators are commonly used to complex the radiometallic ions. Besides conventional chelators, inorganic nanoparticles have also been proposed as radionuclide carriers in previous research but have been mainly focused on the diagnostic applications. In this thesis, various types of inorganic nanoparticles were radiolabeled with therapeutic radionuclides including α, β^- and Auger electron (AE) emitters. The behavior of some radionuclides on the host materials during internal conversion was studied. Moreover, the cell uptake and tumor killing efficiency of the AE emitters radiolabeled nanoparticles were assessed *in vitro* to evaluate their potential for cancer treatment.

Holmium-166 (^{166}Ho, $t_{1/2}$=26.8 h, E_{max}=1.85 MeV) is an important β^- emitter in radionuclide therapy and has been widely applied in the radioembolization treatment of liver metastases. By using its mother nuclide dysprosium-166 (^{166}Dy, $t_{1/2}$=81.5 h) as the *in vivo* generator of ^{166}Ho, higher radiation dose can be achieved with the same activity as ^{166}Ho. However, the internal conversion effects during the decay of ^{166}Dy to ^{166}Ho can lead to the release of 72% of ^{166}Ho to the environment when being bound to chelators (e.g. DOTA). In Chapter 2, we radiolabeled ^{166}Dy on core-shell structured gold nanoparticles as well as platinum-gold bimetallic nanoparticles. The radiolabeling efficiency of ^{166}Dy was found to be 60% and 70% in ^{166}DyAu@AuNPs and ^{166}DyPtAuNPs respectively. The retention of ^{166}Ho on both nanoparticles was found to be more than 95% even after being challenged with DTPA for 72 hours, suggesting that the loss of internally converted ^{166}Ho was avoided. These results might be attributed to the high number of free electrons in these high Z atoms which can quickly fill in the electron vacancies created by the internal conversion effect. Moreover, the extra gold shell improved the colloidal stability of the ^{166}DyAuNPs but had little influence on the ^{166}Ho retention.

The long-term toxicity due to high MPS uptake is one of the main challenges of the biological application of nanoparticles especially when using radiolabeled nanoparticles. By tuning the hydrodynamic diameters to less than 5.5 nm, nanoparticles can escape from the MPS capture and be quickly excreted via the urinary system, i.e. renal clearance. In Chapter 3, PEG-AuNPs with an ultra-small core size of 1.9 ± 0.3 nm and a hydrodynamic diameter of 4.3 ± 0.8 nm were prepared and found to be colloidally stable in various physiological solutions. Besides the potential renal clearable property, these small nanoparticles might also passively accumulate in the cell nucleus after being internalized. Thus, these small PEG-AuNPs were radiolabeled with an Auger electron emitter, ^{125}I by chemical absorption on the gold surface. ^{125}I has a long half-life of 59.4 days and emits 23.0 AEs per decay. These AEs have an intermediate linear energy transfer (LET) of 4~26 keV but a short range of only a few nanometers. Thus, ^{125}I has to be delivered close enough to the DNA molecules, i. e. in the cell nucleus, to cause sufficient damage to the tumor cells. According to the results from the subcellular fractionation assay, 15% to 20% of the internalized ^{125}I-PEG-AuNPs were located in the nucleus of U87 cells. Moreover, significant anti-tumor effect of the ^{125}I-PEG-AuNPs was observed from various *in vitro* assays in U87 cells despite the modest total uptake of the ^{125}I-PEG-AuNPs. The high number of AEs per decay of ^{125}I as well as the self-radiosensitization effect of the PEG-AuNPs might account for the observed high cytotoxicity to U87 cells.

Motivated by the positive results from the previous chapter, more combinations of AE emitters and small nanoparticles were designed and prepared in Chapter 4, namely ^{111}In-DTPA-AuNPs and ^{111}In-DTPA-Ag_2TeNPs. ^{111}In has been extensively applied in single photon emission computed tomography (SPECT) imaging but has also been reported for cancer treatment due to the emission of 7.4 AEs per decay. In this chapter, ultra-small GSH-AuNPs and GSH-Ag_2TeNPs with 2-nm core sizes, as well as sub-5.5 nm hydrodynamic diameters, were synthesized and modified with DTPA molecules for the complexation with ^{111}In. From the results of 2D cell uptake experiments, it was found that 49.8% and 23.6% of the internalized ^{111}In-DTPA-AuNPs and ^{111}In-DTPA-Ag_2TeNPs respectively, were accumulated in the cell nucleus of U87 cells. Further *in vitro* cytotoxicity assays confirmed the high tumor killing efficiency of these ^{111}In radiolabeled nanoparticles in U87 cells.

Due to the higher LET of AEs and α particles when compared to β^- particles, they have primarily direct interaction with DNA molecules and can thus produce more lethal damage to tumor cells. The ^{212}Pb/^{212}Bi *in vivo* generator is one of the most promising candidates in alpha radionuclide therapy. However, approximately 36% of ^{212}Bi the daughter of ^{212}Pb might dissociate from the chelator carriers due to internal conversion effects. In Chapter 5, we designed four types of ^{212}Pb radiolabeled nanoparticles and achieved radiolabeling efficiency varying from 40% to nearly 100%. The overall radiochemical stability of ^{212}Pb and ^{212}Bi was found to be 87.5% to 95% at 24 h, suggesting the stable incorporation of ^{212}Pb in the nanoparticles as well as the prevention of possible ^{212}Bi loss. Moreover, the small sizes of these ^{212}Pb radiolabeled nanoparticles were verified by pilot studies with non-radioactive Pb, suggesting the possible renal clearable properties of these ^{212}Pb radiolabeled nanoparticles.

In summary, this thesis explores the application of nanoparticles as the carriers of radionuclides in radionuclide therapy. The results reported in this thesis proved that the possible dissociation of radionuclides caused by nuclear events such as internal conversion can be well prevented when being loaded on nanoparticles composed of high Z elements. The combination of AE emitters and ultra-small nanoparticles has been proven to be a very promising candidate in Auger therapy. Future studies should focus on the improvement of cell uptake of these nanoparticles, by, for instance, the addition of tumor-targeting moieties such as PMSA inhibitors and FAP inhibitors. Based on the results obtained from this thesis, nanoparticles especially those with small sizes might be appropriate radionuclide carriers in radionuclide therapy as replacement of the commonly used chelators, providing new opportunities for cancer treatment.

Samenvatting

Radionuclidetherapie is een belangrijke behandelingsmethode voor kanker die gebruikmaakt radionucliden voor de lokale bestraling van tumoren. Radiofarmaca zijn doorgaans samengesteld uit drie componenten: een radionuclide, een drager, en een tracer die selectief aan tumoren bindt. Voor de dragers worden vaak macrocyclische en acyclische chelatoren gebruikt die een complex vormen met de radioactieve metaalionen. Naast deze conventionele chelatoren is er in het verleden ook onderzoek gedaan naar het gebruik van inorganische nanodeeltjes als radionuclidedragers, maar dit was voornamelijk gericht op diagnostische toepassingen. In dit proefschrift zijn verschillende soorten anorganische nanodeeltjes geradiolabeld met therapeutische radionucliden, waaronder α-, β^-- en Auger-elektronen (AE) stralers. Het gedrag van een aantal radionucliden geladen op de nanodeeltjes is bestudeerd tijdens interne conversie. Daarnaast werden de celopname en de efficiëntie waarmee tumoren werden vernietigd door de nanodeeltjes, welke geradiogelabeld waren met AE-stralers, *in vitro* beoordeeld op hun potentieel voor kankerbehandeling.

Holmium-166 (^{166}Ho, $t_{1/2}$=26.8 uur, E_{max}=1.85 MeV) is een belangrijke β^- emitter binnen de radionuclidetherapie, en wordt veelvuldig toegepast in de behandeling van levermetastasen door middel van radioembolisatie. Door gebruik te maken van de moedernuclide dysprosium-166 (^{166}Dy, $t_{1/2}$=81.5 uur) als *in vivo* generator voor de productie van ^{166}Ho kan een hogere stralingsdosis worden bereikt met dezelfde beginactiviteit als ^{166}Ho. De interne conversie effecten die plaatsvinden tijdens het verval van ^{166}Dy naar ^{166}Ho kunnen echter leiden tot het vrijkomen van 72% van het ^{166}Ho wanneer het gebonden is aan chelatoren (zoals DOTA). In Hoofdstuk 2 hebben we ^{166}Dy gelabeld op kern-schil gestructureerde goud nanodeeltjes en platina-goud bimetalen nanodeeltjes. De radiolabeling efficiëntie van ^{166}Dy was 60% en 70% in respectievelijk ^{166}DyAu@AuNPs en ^{166}DyPtAuNPs. De retentie van ^{166}Ho op beide soorten nanodeeltjes was meer dan 95%, zelfs nadat ze waren blootgesteld aan DTPA gedurende 72 uur, wat suggereert dat het verlies van interne-conversie ^{166}Ho werd vermeden. Deze resultaten kunnen worden toegeschreven aan het grote aantal vrije elektronen in deze hoge-Z atomen, die snel het elektronentekort dat wordt gecreëerd door de interne conversie kunnen opvullen. Bovendien verbeterde de extra gouden

schil de colloïdale stabiliteit van de ^{166}DyAuNPs, maar had verder weinig invloed op de retentie van ^{166}Ho.

De toxiciteit op lange termijn als gevolg van een hoge endoplasmatisch reticulum (ER) opname is een van de belangrijkste uitdagingen bij de biologische toepassing van nanodeeltjes, vooral bij het gebruik van geradiolabelde nanodeeltjes. Door te zorgen dat de hydrodynamische diameter minder is dan 5,5 nm kunnen nanodeeltjes ontsnappen aan het ER systeem en snel worden uitgescheiden via de urine, dus via renale klaring. In Hoofdstuk 3 werden PEG-AuNPs met een bijzonder kleine kerngrootte van 1,9 ± 0,3 nm en een hydrodynamische diameter van 4,3 ± 0,8 nm bereid, welke colloïdaal stabiel bleken te zijn in verschillende fysiologische oplossingen. Naast dat ze mogelijk renaal geklaard worden, kunnen deze kleine nanodeeltjes zich ook passief ophopen in de celkern nadat ze zijn geïnternaliseerd. Daarom werden deze kleine PEG-AuNPs gelabeld met een Auger-elektronenemitter, ^{125}I, door chemische absorptie op het goudoppervlak. ^{125}I heeft een lange halfwaardetijd van 59,4 dagen en zendt 23,0 AEs per verval uit. Deze AE hebben een lineïeke energieoverdracht (LET) van 4~26 keV maar een korte reikwijdte van slechts enkele nanometers. Daarom moet het ^{125}I dicht genoeg bij het DNA worden afgeleverd, dus in de celkern, om voldoende schade aan de tumorcellen te veroorzaken. Volgens de resultaten van de subcellulaire fractionatie analyses bevond 15% tot 20% van de geïnternaliseerde ^{125}I-PEG-AuNPs zich in de kern van U87 cellen. Bovendien werd een significante antitumorwerking van de ^{125}I-PEG-AuNPs waargenomen bij verscheidene *in vitro* analyses van de U87 cellen, ondanks de bescheiden totale opname van de ^{125}I-PEG-AuNPs. Het hoge aantal AEs per ^{125}I verval, alsmede het radiosensibiliserende effect van de PEG-AuNPs, kunnen verklaren waarom er een hoge cytotoxiciteit werd waargenomen bij U87 cellen.

Gemotiveerd door de positieve resultaten uit het vorige hoofdstuk werden in Hoofdstuk 4 meer combinaties van AE-emitters en kleine nanodeeltjes gesynthetiseerd, namelijk ^{111}In-DTPA-AuNPs en ^{111}In-DTPA-Ag2TeNPs. ^{111}In wordt veelvuldig toegepast in SPECT (single photon emission computed tomography) imaging, maar is ook onderzocht voor de behandeling van kanker vanwege de emissie van 7,4 AEs per verval. In dit hoofdstuk werden ultrakleine GSH-AuNPs en GSH-Ag_2TeNPs met een kerngrootte van 2 nm en hydrodynamische diameters van minder dan 5,5 nm gesynthetiseerd en gemodificeerd met DTPA-moleculen voor de binding met ^{111}In. Uit de resultaten van 2D celopname experimenten bleek dat respectievelijk 49,8% en 23,6% van de geïnternaliseerde ^{111}In-

DTPA-AuNPs en ^{111}In-DTPA-Ag_2TeNPs zich ophoopten in de celkern van U87-cellen. Verdere *in vitro* cytotoxiciteitstesten bevestigden de hoge efficiëntie waarmee deze ^{111}In-gelabelde nanodeeltjes U87 tumoren doodden.

Vanwege de hoge LET van AE en α-deeltjes in vergelijking met β^--deeltjes hebben ze voornamelijk directe interactie met DNA-moleculen en kunnen ze daardoor meer (dodelijke) schade aan tumorcellen veroorzaken. De ^{212}Pb/^{212}Bi *in vivo* generator is een van de meest veelbelovende kandidaten voor alfa-radionuclidentherapie. Echter, ongeveer 36% van ^{212}Bi, het dochternuclide van ^{212}Pb, kan zich dissociëren van chelatoren als gevolg van interne conversie effecten. In Hoofdstuk 5 hebben we vier soorten ^{212}Pb-gelabelde nanodeeltjes gesynthetiseerd en radiolabeling efficiënties variërend van 40% tot bijna 100% bereikt. De algehele radiochemische stabiliteit van ^{212}Pb en ^{212}Bi lag tussen de 87,5% en 95% na 24 uur, wat wijst op de stabiele opname van ^{212}Pb in de nanodeeltjes en minimaal ^{212}Bi verlies. Bovendien werden de kleine maten van deze ^{212}Pb-gelabelde nanodeeltjes bevestigd door pilotstudies met niet-radioactief Pb, wat wijst op mogelijke renaal-klarende eigenschappen.

Samengevat onderzoekt deze scriptie de toepassing van nanodeeltjes als dragers van radionucliden in radionuclidetherapie. De resultaten die in deze scriptie worden gepresenteerd, tonen aan dat de mogelijke dissociatie van radionucliden als gevolg van nucleaire gebeurtenissen zoals interne conversie kan worden voorkomen wanneer ze worden geladen op nanodeeltjes samengesteld uit elementen met een hoog atoomnummer. Er is bewezen dat de combinatie van AE-emitters en ultrakleine nanodeeltjes zeer veelbelovend is voor Auger-therapie. Toekomstige studies zouden zich moeten richten op het verbeteren van de celopname van deze nanodeeltjes, bijvoorbeeld door de toevoeging van tumorzoekende componenten zoals PMSA-remmers en FAP-remmers. Op basis van de resultaten verkregen uit deze scriptie zouden nanodeeltjes, voornamelijk die met kleine afmetingen, geschikte dragers van radionucliden kunnen zijn in radionuclidetherapie als vervanging voor de veelgebruikte chelatoren, wat nieuwe mogelijkheden biedt voor de behandeling van kanker.

List of publications

Publications

Related to this thesis:

Wang, R., Ponsard, B., Wolterbeek, H., Denkova A. Core–shell structured gold nanoparticles as carrier for ^{166}Dy/^{166}Ho in vivo generator. EJNMMI radiopharm. chem. 2023, 7, 16.

Wang, R., Liu, H., Antal B. Wolterbeek, H., Denkova A. Ultra-small gold nanoparticles radiolabeled with Iodine-125 as potential new radiopharmaceutical. ACS Appl. Bio Mater. 2024, 7, 1240−1249.

Wang, R., Wolterbeek, H., Denkova A. Design of a Novel Lead-212 Radiopharmaceutical based on Ultra-small Silver Telluride Nanoparticles. J Label Compd Radiopharm. Submitted.

Wang, R., Wolterbeek, H., Denkova A. PSMA targeted ultra-small gold nanoparticles for Auger therapy. In preparation.

Other publications:

Liu, H., **Wang, R.**, Gao, H., Chen, L., Li, X., Yu, X., Wu, Y., Bai, Y., Wei, W., Wang, M., Nanoprobes for PET/MR Imaging. Adv. Therap. 2023, 2300232.

Liu, H., Nadar, R. A., Fauzia, R. P., Laan, A. C., Doeswijk, B., **Wang, R.**, van de Meer, A., van Cooten, Q., Carroll, E. C. M., Eelkema, R., Denkova, A. G., Combined Chemoradionuclide Therapy Using Poly(ε-caprolactone-b-ethylene oxide) Micelles as the Delivery Vehicle. Adv. Therap. 2023, 6, 2200224.

Oral presentations

Wang, R., Wolterbeek, H., Denkova A. Application of Ultra-small ^{125}I-PEG-AuNPs in Auger therapy, 33rd NKRV Workshop, Petten in the Netherlands, February 2023.

Wang, R., Wolterbeek, H., Denkova A. Design of a Novel Carrier for ^{166}Dy/^{166}Ho in vivo Generator, RadChem 2022, Marianske Lazne in Czech Republic, May 2022.

Poster presentations

Wang, R., Wolterbeek, H., Denkova A. Core-shell structured gold nanoparticles as carrier for ^{166}Dy/^{166}Ho *in vivo* generator, The Miller Online Workshop on Radiation Chemistry, online, February 2022.

Wang, R., Wolterbeek, H., Denkova A. ^{166}Dy/^{166}Ho radiolabeled nanoparticles as potential candidate for radionuclide therapy, RRFM 2023, Antwerp in Belgium, April 2023.

Acknowledgements

This amazing adventure started six years ago. Without a clear plan for my career after leaving Beijing Normal University, I decided to pursue a MSc degree somewhere in Europe. After being rejected for many times, I was offered a chance to join the MSc program of Chemical Engineering in TU Delft. Because of my previous research experience with PET tracers, I chose the track of nuclear science and engineering and actually became one of the last students of this track. This was also when I met my future PhD promotors, Antonia and Bert. Luckily, I got the chance to complete my master thesis in the ARI group and later on got the offer for this PhD project. Now, it is time to put an end to this story and start a new journey. So, I would like to express my sincere gratitude to everyone who helped me during the past four years at the end of this thesis.

First and most importantly, I would like to thank my promotor, Antonia. Thank you for giving me the opportunity to do this project. You are always available for discussing with me, no matter it is about the latest development of RNT or just the current results of my experiments. I will never be able to complete my thesis without your great input. I also learned how to deal with life-work balance from you. I still remember how shocked you were when I asked you for the permission to work during weekends the first also the last time. Thank you for everything you did for me.

I also want to thank my promotor Bert Wolterbeek for all the discussions on my projects. I used to easily get biased when analyzing the problems. But you can always provide suggestions out of the box and point out a new path to the final goal.

Next, I want to acknowledge all of our collaborators from Radboud University and Erasmus MC. Dr. Frank Nijsen and Dr. Sandra Heskamp, thank you for all the discussions on my project. Dr. Erik de Blois, thank you for the routinely supply of ^{111}In. Dr. Yann Seimbille, thank you for providing iPSMA, SCN-p-Bn-DTPA, LNCaP cells and all the suggestions on my projects. Katalin from the Centre for Energy Research (Hungary), Bernard from the Belgian Nuclear Research Centre, SCK CEN (Belgium) and Christian from the Forschungsreaktor TRIGA Mainz (Germany) are all gratefully acknowledged for sample irradiations.

I want to thank all the colleagues from ARI. Kristina, thank you for all the discussions on nanoparticles and tumor targeting. Robin, thank you so much on sharing your experience on doing research, creating the great work environment in ARI and most importantly, buying the new centrifuge in lab. Baukje, thank you for helping me in lab for the ICP measurements, irradiating samples and dealing with all the mess I made. Thank you for pushing me forward to learn new skills (such as open a rabbit safe and fast) when I was hesitating. Astrid, thank you for all the help in the cell lab, measuring radioactive samples with WALLAC or INNA and of course the irradiation of samples in the reactor. Thank you for your great input on the calibration of the equipment and all the valuable suggestions for my experiments. Folkert, thank you for helping me measure my samples on the soft X-ray detector and dealing with all the IT issues. Eline, thank you for your help on DLS measurements and the favor on supervising my BSc and MSc students. It is awesome to work with you! Mehmet, thank you for your help on INNA measurements and sealing quartz. Adrie, thank you for all the help at the beginning of this project. Anouk, thank you for handling all the paper works over the past four years. I also want to express my sincere thanks to Dr. Rienk Eelkema, Guotai Li and Sietse Kuipers from the ASM group for allowing me to use the zeta-sizer, FT-IR and pH meter. A big thank you to Wiel Evers from BN for his help on TEM and HR-TEM. Without your help, I will never know how my nanoparticles look like. I also want to thank Kirsten from the PPE group for helping me with the confocal microscope. Stephen from the Biocatalysis group is gratefully acknowledged for the help on NMR measurements.

Then I want to thank the previous PhD students from ARI, Huanhuan and Chao for the accompany and all the help during the past four years. You both helped me so much not only on doing experiments but also on daily life. It is always memorable to have lunch and dinner together when you were in Delft. Thank you for everything and I wish you all the best in your future.

Next, I want to express my huge gratitude to Juncheng and Jiechen. I really can’t imagine we have known each other for more than 10 years since the bachelor program in BNU! It is a pity I missed your wedding party because of Covid-19. But we finally met up in the Netherlands and had a lot of wonderful moments together. Specifically, Juncheng, thank you so much for helping me with organic synthesis and NMR measurements. I wish both of you enjoy your time in the Netherland and complete your study successfully!

I want to thank my office mates, Rogier and Robin Nadar. Rogier, we first met on a workshop and talked a lot about Holland PTC and doing PhD or not, and it is so amazing we finally did our PhD together in ARI! Thank you for teaching me Dutch, tasting bears in 'T koepeltje and all the talks over the past years. Robin, we started to work in ARI on the same day in 2019! Thank you for all your help on biological experiments and sharing your experience of PhD life with me.

Then I want to thank my fellow PhD students and post-docs in ARI: Hu, Tiantian, Retna, Alexandra, Svenja, Qi jia, Gauri and Bing. Thank you for all your help on my research and making my time at ARI memorable. I also want to thank my daily supervisor at MSc thesis and internship, Alexandra Arranja. Thank you for all the help in the very beginning of my academic career.

Furthermore, I want to thank my BSc and MSc students. Jelta, Catalina, Linge, Rinus and Olivier thank you for your input on my projects. It has been an honor to work with you.

I want to acknowledge the colleagues from SBD for checking the permits and dealing with all the contaminations I made during the past four years.

I also want to thank the Chinese community in TU Delft. Yifan, Fengqi, Ziying, Zimu, Jessie, Fandy, Hamutu, Qi Shen, Pinping, yueer, Hanggai, Shengnan, Qidi, Chenglong, Chaofan, Justin, Beien, Bei, Ming and Chao Wang.

I am also very grateful for my friends in China, Yunjia (aka the wolf), Wenkai, Huiyu, Ping, Zheng, Mengze, Yuting, Yuanyuan, Yang and Yue. Thank you for all the talks and sharing your happiness with me over the past four years. With you here, I never felt alone in this (relatively) new country. Life is long, long live our friendship!

Most importantly, I want to thank my family for their support during the past years. I have been away from home for seven years but never heard any complain from my parents. It will be impossible for me to complete my study abroad without your understanding and help. 爸爸妈妈，我爱你们! I also want to thank my aunts, uncles and cousins. Thank you for all the help and suggestions over the past years.

The China Scholarship Council (CSC) is gratefully acknowledged for the financial support in the past four years.

Last but not least, I want to thank Li "Oliveira/TIME" Peinan, the amazing Chinese StarCraft 2 player, the world champion of IEM Katowice 2023, the protagonist of the most exciting underdog story who had an expectation of only 0.37% to win the final championship.

I want to thank you for your firm faith and the great desire on winning. You make me realize that no matter how frustrating and disappointing I am, I can still fulfill my dreams as long as I never give up, as long as I keep the love and passion for life at the bottom of my heart. Like you said, a normal person can still be world champion even nobody trusts you. Thank you for cheering me up at the dark moments of my life! GG! WP!

To my family, friends and colleagues,
Thank you for showing up in my life and making it so splendid!
谢谢你们！

Runze Wang
王润泽

Delft, January 2024

Curriculum Vitae

Runze Wang was born on 12th December 1994 in Harbin, Heilongjiang province, P. R. China. He studied at Beijing Normal University from 2013 to 2017 and obtained the bachelor's degree in Chemistry. During September 2017 to August 2019, he studied in TU Delft, the Netherlands and obtained the master degree in Chemical Engineering with the specific track on Nuclear Science and Engineering. From August 2018 to May 2019, he performed his master thesis study in the Applied Radiation and Isotopes (ARI) group at the TU Delft Reactor Institute. His master thesis is entitled "The influence of radiation dose and dose rate on the killing efficiency of tumor cells——A study using ^{90}Y and ^{166}Ho". Then he joined the Quirem Medical B.V. in Deventer, the Netherlands for a three-month internship on a feasibility study of using membrane emulsification technology for the production of polymeric microspheres. In September 2019, he joined the ARI group and started his PhD study under the supervision of Dr. A. G. Denkova and Prof. H.T. Wolterbeek. His PhD research was focused on the application of ultra-small nanoparticles in radionuclide therapy.

This thesis presents an overview of the research outcome that was achieved during his PhD research in TU Delft Reactor Institute.